Master Thesis

Ordered macroporous α-alumina

as support material for the silver catalyzed epoxidation of ethylene

Synthesis, characterization and optimization

Utrecht University, Department of Chemistry

Inorganic Chemistry and Catalysis

Debye Institute for Nanomaterial Science

Author:
Petra Keijzer, BSc

Daily Supervisor:
Jeroen van den Reijen, MSc.

First Examiner:
Prof. Dr. Petra de Jongh

Second Examiner:
Dr. Peter Ngene

Universiteit Utrecht

November 2014 - November 2015

Abstract

In this research, ordered macroporous α-alumina was synthesized, the pore structure of the material was optimized and the material was characterized. PMMA spheres were synthesized using surfactant free emulsion polymerization and assembled into colloidal crystals by centrifugation. These crystals were used as template material to synthesize ordered macroporous α-alumina by filling the voids of the crystal with aluminum hydroxide and calcining the material. Compared to the material obtained by using the synthesis method described in literature, the cage structure of the macropores was improved. This was done by increasing the amount of impregnation steps and by first calcining the impregnated crystals under nitrogen flow, to obtain γ-alumina covered with thin layer of carbon. This layer of carbon stabilized the pore structure and was burned off during a second calcination under air flow. During this second calcination, the γ-alumina was converted into α-alumina at 1150 °C. The obtained material contained pores of 220 nm (SEM, UV-VIS) and had a surface area of approximately 20 m^2/g (N_2-physisorption). Macroporous α-alumina was used as support material in the epoxidation of ethylene. After silver particles of about 20 - 80 nm were attached to the α-alumina by incipient wetness impregnation, the catalyst was tested in an epoxidation setup. By comparing this catalyst to other catalysts composed of lower surface area α-alumina, a clear trend was observed between the surface area of the alumina and the selectivity towards ethylene oxide. This trend is explained by the amount of hydroxyl groups present on the alumina material, which facilitate the complete combustion reaction of ethylene into CO_2 and water.

Contents

1 Introduction **1**

2 Theory **3**

2.1 Reaction mechanism epoxidation of ethylene 3

2.2 Silver as active metal in the epoxidation of ethylene 5

2.3 α-alumina as support material in the epoxidation of ethylene 6

2.4 Ordered meso- or macroporous materials 7

2.4.1 Soft templating 7

2.4.2 Hard templating 8

2.5 Deactivation of the catalyst 9

3 Aims **11**

4 Characterization techniques **13**

5 Part I: Synthesis of template material **15**

5.1 Methods 15

5.1.1 Surfactant free emulsion polymerization 15

5.1.2 Assembly of PMMA spheres into colloidal crystal 16

5.2 Experimental 17

5.2.1 Chemicals 17

5.2.2 Synthesis of PMMA spheres 17

5.2.3 Assembly of PMMA spheres into colloidal crystal 18

5.2.4 Characterization 18

5.3 Results and discussion 18

5.3.1 Synthesis of PMMA spheres 18

5.3.2 Colloidal crystals of PMMA 20

6 Part II: Synthesis of support material **25**

6.1 Methods 25

6.1.1 Synthesis of ordered macroporous α-alumina 25

6.2 Experimental 26

6.2.1 Chemicals 26
6.2.2 Synthesis of ordered macroporous α-alumina 26
6.2.3 Number of impregnation steps applied and larger scale 27
6.2.4 Calcination temperature and atmosphere 28
6.2.5 Pretreatment PMMA colloidal crystals 28
6.2.6 Calcination in combustion boat versus plug flow reactor 28
6.2.7 Strength of the macropores 29
6.2.8 Characterization 29
6.3 Results and discussion 29
6.3.1 Number of impregnation steps applied and larger scale 29
6.3.2 Properties/characteristics of α-alumina 30
6.3.3 Calcination temperature and atmosphere 38
6.3.4 Synthesis of ordered macroporous γ-alumina 42
6.3.5 Influence calcination step under inert atmosphere 44
6.3.6 Pretreatment PMMA colloidal crystals 48
6.3.7 Calcination in combustion boat versus plug flow reactor 49
6.3.8 Strength of cage structure macroporous alumina 52

7 Part III: Synthesis of catalyst and catalytic testing 53
7.1 Methods 53
7.1.1 Incipient wetness impregnation 53
7.2 Experimental 53
7.2.1 Chemicals 53
7.2.2 Impregnation of α-alumina 53
7.2.3 Characterization 54
7.2.4 Catalytic testing in ethylene epoxidation setup 55
7.3 Results and discussion 55
7.3.1 Impregnation of α-alumina 55
7.3.2 Catalytic testing in ethylene epoxidation setup 57

8 Conclusions 59

9 Outlook **61**

9.1 Template material 61

9.1.1 Use of larger PMMA spheres 61

9.1.2 Preparation of PMMA colloidal crystals 61

9.2 Support material 61

9.2.1 Alkoxides precursors or melt impregnation 61

9.2.2 Bulk characterization by using UV-VIS spectroscopy 62

9.2.3 Calcination parameters 62

9.2.4 γ-alumina 63

9.3 Catalyst 63

9.3.1 Impregnation 63

9.3.2 Characterization 63

9.3.3 Stability tests 63

10 Acknowledgments **67**

Appendix A Template material **i**

Appendix B Support material **iv**

Appendix C Catalyst and catalytic test **xi**

1 Introduction

Since ethylene oxide is an important building block for several plastics, polyesters and glycols, extensive research has been conducted on the production of ethylene oxide. In 1931, the synthesis of ethylene oxide by direct oxidation of ethylene over a silver catalyst was discovered by Lefort (Equation 1) [1]. However, ethylene oxide is not the only product formed, since ethylene and ethylene oxide (EO) can also be completely oxidized. The products of these reactions are CO_2 and H_2O (Equations 2 and 3).

$$2CH_2{=}CH_2 + O_2 \longrightarrow 2\ EO \tag{1}$$

$$CH_2{=}CH_2 + 3O_2 \longrightarrow 2CO_2 + 2H_2O \tag{2}$$

$$2\ EO + 5O_2 \longrightarrow 4CO_2 + 4H_2O \tag{3}$$

In catalysis, the size of the active metal is commonly in the range of a few nm, since by decreasing the particle size, more active surface area is obtained by using the same amount of metal. However, it is proposed that in the epoxidation of ethylene, the selectivity of the epoxidation reactions is dependent on the size and structure of the silver particles [2, 3]. A higher selectivity towards ethylene oxide (Equation 1) is achieved on Ag(100) facets compared to Ag(111) facets, since ethylene oxide is mainly formed on these facets, whereas the complete combustion reaction of ethylene (Equation 2) mainly takes place on Ag(111) facets [3]. The surface of larger particles consist of larger Ag(100) facets compared to smaller silver particles, which surface mainly consists of Ag(111) facets [3]. The optimum silver particle size found by Goncharova *et al.*is between 60 and 100 nm [2].

For the epoxidation of ethylene in industry, silver particles are normally placed onto an α-alumina support, to prevent sintering and aggregation of the silver particles [4, 5]. The main advantage of α-alumina as support material is the low density of hydroxyl groups on the surface. These groups facilitate the isomerization of ethylene oxide into acetaldehyde, which reacts further into CO_2 and H_2O (Reaction 3) [6]. The α-alumina support generally used in industry has a surface area of 0.5 - 5 m^2/g, which is quite low compared to most support materials used for other catalytic reactions [4]. Although the low surface area of α-alumina minimizes the amount of hydroxyl groups present, this is a substantial disadvantage for the stability and maximum loading of the catalyst [7].

In general, the surface area of support materials can be increased by the introduction of (ordered) micro- ($<$ 2 nm in diameter), meso- (2 - 50 nm in diameter) and/or macropores ($>$ 50 nm in diameter) by using templates [8]. For example, by using a template, mesoporous silica or carbon materials having surface areas exceeding 1000 m^2/g were synthesized [9, 10]. In this research, macropores are favored, since by using a macroporous support in the preparation of the catalyst, the silver particles ($>$ 50 nm) can be distributed inside this macroporous structure. Furthermore, an ordered cage structure is favored, since this both allows advanced characterization and research on how parameters as pore size and structure influence the preparation and performance of the catalyst. This may lead to new insights in catalyst deactivation mechanisms. Recently, new insights on deactivation mechanisms in other catalytic reactions were

gained, when model catalysts, composed of ordered mesoporous support materials, were used [11–13].

Three-dimensionally ordered macroporous materials were synthesized by Stein *et al.*, by using colloidal crystals of silica, polystyrene or poly(methyl methacrylate) (PMMA) spheres as template material [14, 15]. The macroporous materials were obtained by filling the voids of the template material with precursor solutions, which were converted into metal oxides by calcination. Sokolov *et al.* synthesized ordered macroporous α-alumina materials, by impregnating PMMA colloidal crystals with aluminum hydroxide [16]. By varying the size of the PMMA spheres, the pore size of the alumina was adjusted. Ordered macroporous α-alumina materials with a pore size of 315, 615 and 975 nm with surface areas which range from 24 to 20 m^2/g, respectively, were obtained by calcining impregnated PMMA colloidal crystals under air flow at 1150 °C [16].

Sokolov *et al.* showed that the cage structure of alumina containing large pores ($>$ 600 nm) were better preserved compared to the cage structure of the alumina containing small pores ($<$ 350 nm), since the alumina walls between the cages were thicker at increased pore size [17]. These thicker walls stabilized the cage structure and therefore, the cage structure of the alumina was better resistant against deformation caused by structure transformations. Deformation of cage structure was observed in some parts of the alumina material with pores of 315 nm [17]. Since these α-alumina materials contain ordered macropores and the surface area of these materials range from 20 to 24 m^2/g, this material is promising as support material to synthesize a model catalyst for the epoxidation reaction of ethylene [16].

In this research, we want to synthesize ordered macroporous α-alumina, in which the size of the cages is about 200 - 250 nm. Since there is a high probability for deformation of the cage structure, the synthesis method of Sokolov *et al.* needs to be improved to stabilize and preserve the cage structure.

In Chapter 2, extra theory about the epoxidation reaction, α-alumina as support material, silver as active metal and about the introduction of pores is given. In Chapter 3, the aims of this research and the research questions are listed. In Chapter 4, all characterization techniques used to characterize the obtained products are given. Chapter 5 describes the synthesis of the PMMA template material, which is used to synthesize ordered macroporous α-alumina support materials in Chapter 6. Silver is deposited on one of these support materials in Chapter 7, whereupon this catalyst was tested in the epoxidation of ethylene. These last three chapters are each divided into methods, experimental and results and discussion. The research questions are answered and conclusions are drawn in Chapter 8. Finally, in Chapter 9, potential future work is described in the outlook.

2 Theory

2.1 Reaction mechanism epoxidation of ethylene

The reaction mechanism of the epoxidation of ethylene to ethylene oxide is still not fully understood [5]. Several theories are present about the catalyst surface and the nature of the active oxygen atoms. In 1973, Kilty *et al.* proposed a selective ethylene epoxidation reaction, where molecular oxygen adsorbs onto the silver surface and reacts with an ethylene molecule to form ethylene oxide [18]. This reaction was proposed to occur via the Eley-Rideal mechanism, in which one oxygen atom stays adsorbed onto the silver surface after the double bond of oxygen is broken (Figure 1).

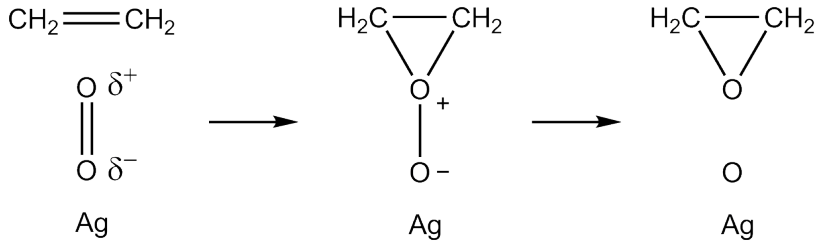

Figure 1: Proposed mechanism for the selective epoxidation reaction of ethylene oxide by Kilty *et al.* [18]

To remove these oxygen atoms from the silver surface, Kilty *et al.* proposed a non-selective combustion reaction in which six of these adsorbed oxygen atoms and one ethylene molecule react to form two molecules of CO_2 and two molecules H_2O, via the Langmuir-Hinselwood mechanism [18]. This reaction is shown in Equation 4.

$$O_{(ads)} + CH_2{=}CH_2 \longrightarrow OC_2H_4 \xrightarrow{5O(ads)} 2CO_2 + 2H_2O \tag{4}$$

In this proposal, six ethylene molecules react with six oxygen molecules to form ethylene oxide, whereupon the remaining oxygen atoms are removed with one ethylene molecule to form CO_2 and H_2O. Therefore, out of seven ethylene molecules, six ethylene oxide molecules are formed, which gives a limiting selectivity of $\frac{6}{7}$, 85.7 % [18].

By using computer simulations, it was found that a weakly bound oxygen atom (electrophilic, δ^+) breaks the C=C double bond of ethylene, whereupon this oxygen is inserted to form ethylene oxide via the selective epoxidation reaction [5]. This does not have to be an associatively bound oxygen molecule. On the other hand, the more strongly bound oxygen atom (nucleophilic, δ^-) activates the C–H bond of ethylene in the non-selective combustion reaction, producing CO_2 and H_2O [5]. At a high oxygen coverage, the selectivity towards ethylene oxide therefore increases, since the oxygen atoms are more weakly bound to the silver [5].

However, higher selectivities than 85.7 % were found shortly after the limiting selectivity of Kilty *et al.* was published, suggesting that ethylene oxide is not obtained via the selective epoxidation reaction only, but also via the non-selective epoxidation reaction. In the 90's, an oxometallacycle (OMC) surface intermediate was proposed for the non-selective epoxidation reaction, whereupon both CO_2 and ethylene oxide are

obtained [5]. The proposed mechanism for this reaction is mainly based on computer simulations and is shown in Figure 2. After activation of the C–H bond of the ethylene molecule by a nucleophilic attack, an OMC surface intermediate is formed. This transforms either in ethylene oxide (EO) or acetaldehyde (AA), in which acetaldehyde reacts with oxygen to form CO_2 and H_2O. Since the activation energies toward acetaldehyde are lower than the activation energies toward ethylene oxide, mostly CO_2 and H_2O is produced via the non-selective epoxidation reaction [5]. To obtain the high selectivities above 85.7%, Özbek *et al.* proposed that both the selective and the non-selective epoxidation reaction produce ethylene oxide [5].

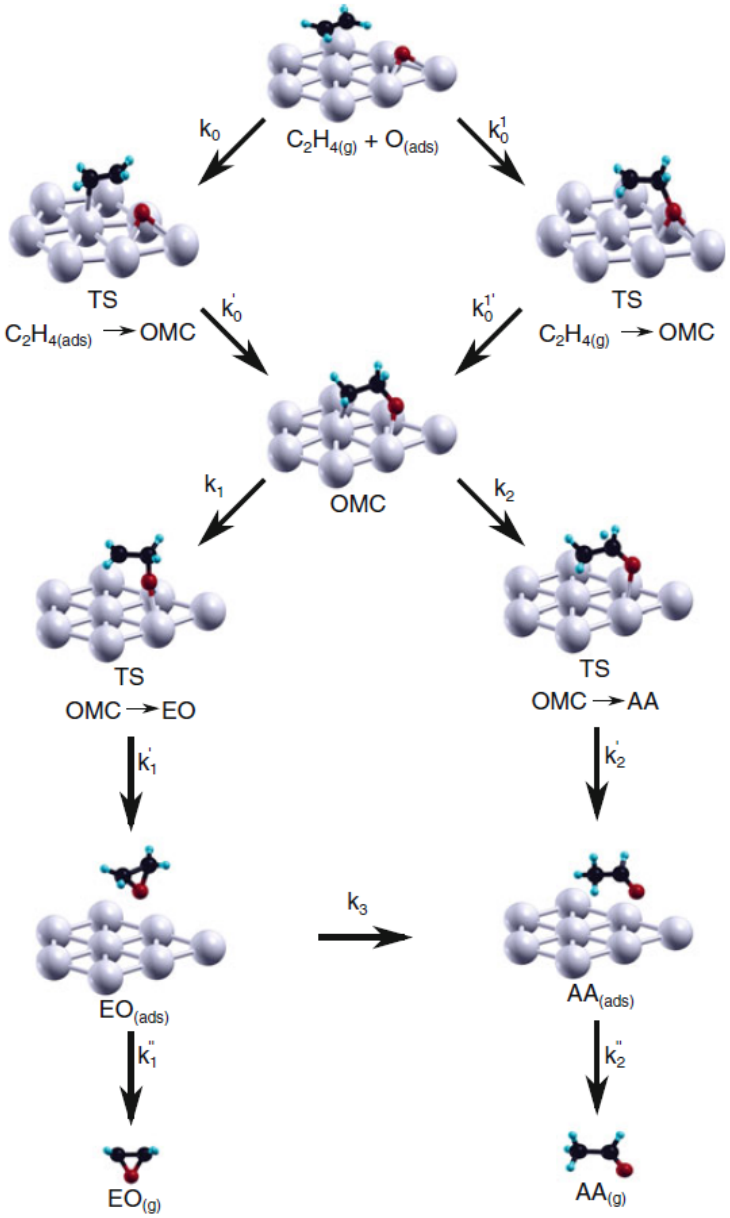

Figure 2: Proposed mechanism for the epoxidation reaction of ethylene oxide through an oxometallacycle (OMC) surface intermediate. The OMC intermediate reacts further into ethylene oxide (EO) or acetaldehyde (AA). Silver: light gray, oxygen: red, carbon: black, hydrogen: blue. [5]

2.2 Silver as active metal in the epoxidation of ethylene

Various metals have been tested as catalyst for the epoxidation reaction of ethylene. However, only silver gives a high selectivity towards ethylene oxide, where most metals cause a complete combustion of ethylene [19]. By using gold or copper as catalyst, ethylene oxide is produced as well, but the selectivity is considerably lower [5]. For catalytic reactions in general, the interaction strength of the adsorbates is very important. This interaction needs to be strong enough to hold and stabilize the adsorbates, but should not be too strong, since the products should be able to desorp from the catalytic surface [20]. Using silver, this optimal interaction strength is achieved. The weak Ag–O bonding activates the C=C double bond instead of the C–H bond, leading to the formation of ethylene oxide instead of CO_2 and H_2O [5].

Additionally to the interaction strength, the surface structure plays a role in the selectivity of the epoxidation reaction. In Figure 3, the OMC surface intermediate is shown on the Ag(100) (left) and Ag(111) (right) surface. The angle of the C–C–O bond in the OMC surface intermediate varies with the structure of the silver.

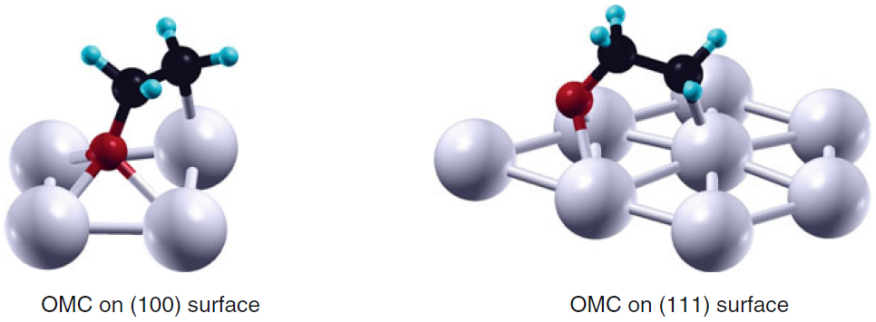

Figure 3: OMC surface intermediate on the surface of silver. [5]

Using density function theory, Christopher *et al.* proposed that the selectivity towards ethylene oxide was higher when performed onto a Ag(100) surface compared to onto an Ag(111) surface, because the Ag(100) surface helps most with the closure of the ring in the oxametallacycle surface intermediate [21]. Hence, to increase the selectivity, particles mainly consisting of an Ag(100) surface are favored. This was tested by Christopher *et al.*, who synthesized silver cubes and rods containing large Ag(100) facets and silver spheres containing both Ag(100) and Ag(111) facets. These particles were placed onto an α-alumina support and were tested in the epoxidation of ethylene [3]. The outcome of this research is that particles with large Ag(100) facets, as the cubes and rods, indeed are more selective towards ethylene oxide compared to spherical particles with mixed Ag(100) and Ag(111) facets [3].

The selectivity dependence on the size of spherical silver particles was investigated by Goncharova *et al.* and Bukhtiyarov *et al.* They found that particles between 50 and 100 nm are more selective than smaller particles and explained this by the proportion of active sites per particle [2, 22]. Larger particles contain more active sites, since larger Ag(100) facets are present, compared to smaller particles, which have in proportion more kinks and step sites consisting of Ag(111) facets. However, in this research, the influence of the particle size on the conversion of ethylene, which influences the selectivity as well, was not investigated. The influence of the conversion of ethylene on

the selectivity towards ethylene oxide is discussed in Section 7.3.2.

The selectivity of the epoxidation reaction is generally increased in industry by promoting the catalyst with a low amount of chloride [4]. Although the overall activity decreases, the selectivity towards ethylene oxide is increased [5]. The effects of chloride on the selectivity is mechanically as well as electronically. Cl blocks vacant sites next to active oxygen atoms mechanical, preventing absorption of ethylene onto the silver surface and suppressing the non-selective reaction, in which mainly oxide and CO_2 and H_2O is produced (Section 2.2) [5]. The electronic effect is the weakening of the Ag–O bond, which suppresses the combustion reaction of ethylene oxide [5]. Furthermore, Cl is considered to decrease the activation energy towards the formation of ethylene oxide instead of acetaldehyde via the OMC surface intermediate [5].

2.3 α-alumina as support material in the epoxidation of ethylene

Alumina (Al_2O_3) is a widely used support material due to its high thermal and mechanical stability. It is an electrical insulator and the point of zero charge is around pH 7.0 - 9.0 [23]. These properties play an important role during the impregnation of a metal onto the support and a small role during the catalytic reaction itself. In industry, silver particles are generally supported on α-alumina for the epoxidation of ethylene. The low density of hydroxyl groups on the surface of α-alumina are beneficial in the epoxidation reaction, because these groups are considered to isomerize ethylene oxide into acetaldehyde, whereupon complete combustion to CO_2 and H_2O follows [6].

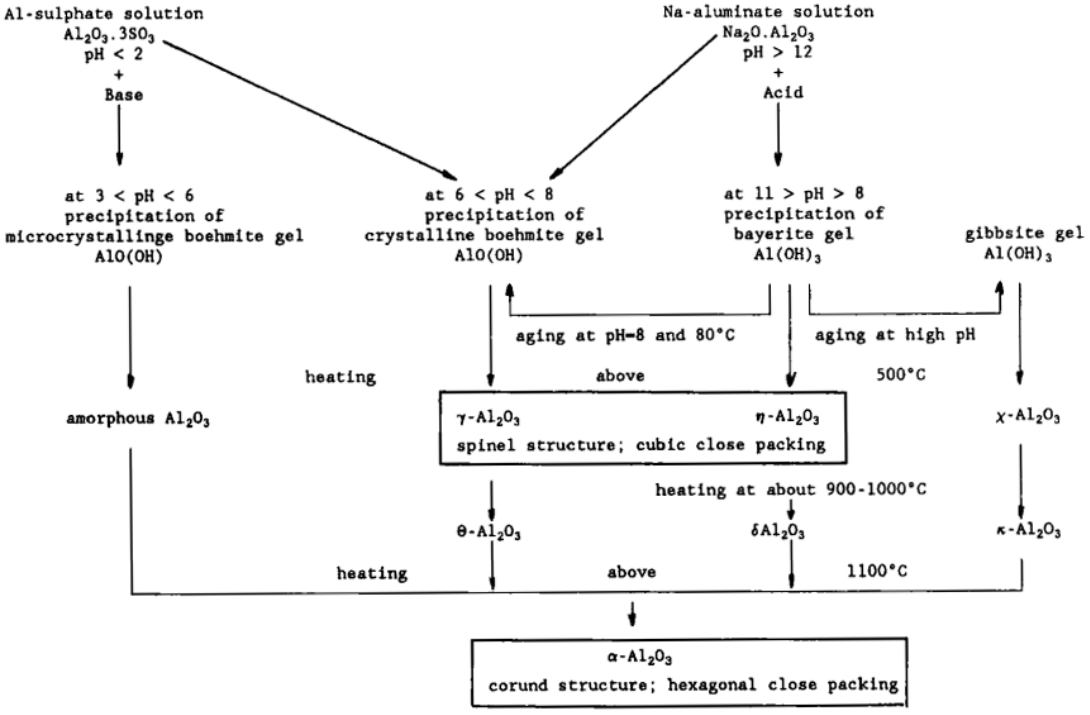

Figure 4: Schematic representation of the formation of various alumina structures. By calcining aluminum hydroxide at different temperatures, these various structures of alumina are obtained. Above 500 °C, γ- or η-alumina are formed and above 1100 °C, α-alumina is formed. [6]

Alumina is generally synthesized by the precipitation of an aluminum precursor via sol-gel chemistry [6]. A solid colloid dispersed in a liquid (sol) is formed by hydrolysis and condensation of the precursor. After further condensation, a three-dimensional gel is formed, which can be crystallized at elevated temperatures [6]. By changing the pH, precursor, temperature, reaction time and/or aging time, various alumina structures can be obtained, as is shown in Figure 4.

It is possible to transform all these different structures into α-alumina by applying a thermal treatment, in which the material is heated above 1150 °C. In catalysis, generally only η-, γ- and α-alumina are used as support material. Where η- and γ-alumina contain micro- and/or mesopores and are amorphous or (partly) crystalline, α-alumina is non-porous and crystalline. Therefore, α-alumina has a very low surface area (0.1 - 2 m^2/g) compared to γ- and η-alumina (15 - 300 m^2/g) [6].

2.4 Ordered meso- or macroporous materials

2.4.1 Soft templating

One commonly used method to increase the surface area of a material is by using soft or hard templates to introduce mesopores and/or macropores. Soft templates consist of a self-assembly of surfactants into micelles and/or liquid crystals. These assemblies form above the critical micelle concentration. The shape and size of the micelles depends on the structure, size and concentration of the surfactant molecules and can be, for instance, spherical, rod-like or disc-like. There are three different ways of soft templating: cooperative self-assembly, "true" liquid crystal templating and evaporation-induced self-assembly [14]. Schematic representations of these methods are shown in Figure 5.

- When cooperative self-assembly is used, precursor and template surfactants form small clusters after they are mixed together. These clusters self-assemble into larger structures, eventually forming mesostructures, in which the liquid crystalline phases are surrounded by precursor solution.
- In "true" liquid crystal templating, first surfactants self-assembly into a liquid crystal and afterward precursor is introduced around these self-assemblies.
- By using evaporation-induced self-assembly, thin films can be synthesized. A mixture of surfactant and precursor is spread out over a large area where the solvent is allowed to evaporate. As a result of the evaporation of the solvent, the concentration of precursor and surfactant increases and at some point, the critical micelle concentration is reached. At this point, the precursor and surfactants starts to self-assembly into a liquid crystalline phase.

In all methods, after the self-assembly is complete, the precursor is precipitated by applying a thermal or chemical treatment. Finally, the template is removed to obtain mesoporous material. [14]

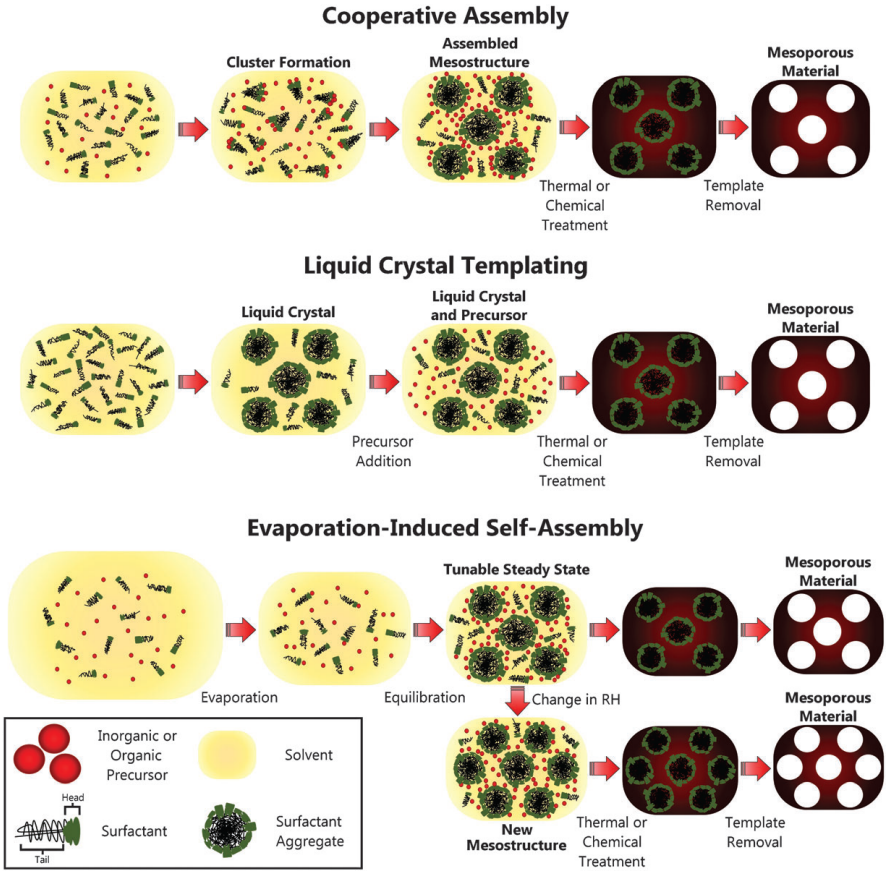

Figure 5: Schematic representation of three synthesis routes for the introduction of pores via soft templating; cooperative self-assembly (top), "true" liquid crystal templating (middle) and evaporation-induced self-assembly (bottom). [14]

2.4.2 Hard templating

By using hard templates, an existing material is used as (sacrificial) template. If an the used template is porous, the voids can be filled with precursor material. Two examples are given in Figure 6, in which ordered mesoporous silica is used as template. First carbon is introduced into the pores of the silica and afterward the carbon is solidified. After removal of the silica, an inverse replica of the pore structure, consisting of carbon, is obtained [24]. To produce a replica of the original silica structure, the inverse carbon replica is again used as hard template for the synthesis of another porous material. The obtained (inverse) replica will not be an exact (inverse) duplicate, because of shrinkage and diffusion of the precursor to empty parts of the material during drying and calcination steps.

By synthesizing inorganic porous materials, generally solution-based precursors are used, mostly a salt dissolved in a polar solvent. The hard template is soaked in this solution, to fill all voids of the material. The capillary forces help to fill these voids. To completely cover the material, the viscosity of the solution and the wetting degree of the solution/template interface are important. Vacuum suction can be used additionally, if the template is wetted insufficiently at atmospheric pressure. After the template is covered or filled with precursor and the excess of precursor is removed, the precursor

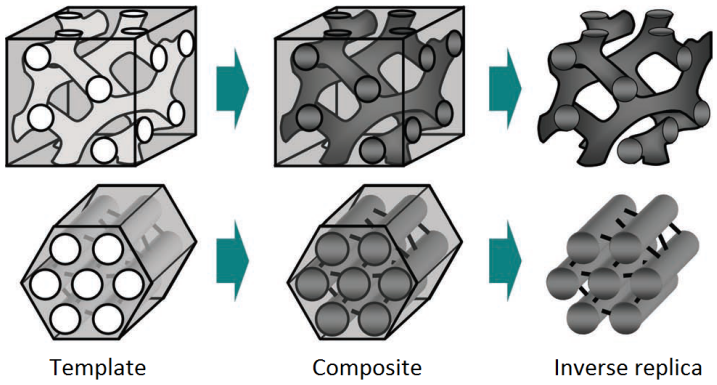

Figure 6: Schematic representation of two mesoporous silica syntheses using hard templating. MCM-48 (top) and SBA-15 (bottom) are used as template. [24]

is transformed into the metal oxide by a thermal or chemical treatment. In the final step, the template is removed by chemical etching, dissolution or calcination. [14]

Hard templates are mostly used to synthesize an inverse structure of an excising material, whereas soft templating is used to synthesize a porous structure bottom-up. By using soft templating, usually (ordered) mesoporous structures are obtained, since the used templates are generally too small for macroporous structures. Therefore, to obtain macroporous structures, generally hard templates are used.

2.5 Deactivation of the catalyst

As a result of increasing the surface area of the support material, an increased stability of the catalyst is expected, since the spacing between the silver particles is increased (at constant weight loading and paricle size) and therefore, sintering and aggregation of these particles is less likely to occur. However, this is not the only deactivation mechanism of the catalyst.

Three main deactivation mechanisms are poisoning, leaching and thermal degradation. The catalyst is poisoned when reactants, products or impurities absorb too strongly onto the silver. This blocks or prevents the catalytic reaction. The products or impurities can absorb onto the active sites of the silver or onto atoms next to the active sites, which prevents reactants to adsorb onto the active sites or blocks surface diffusion [25, 26].

When leaching occurs, (part of) the catalyst is slowly dissolved. Not only dissolution of the silver leads to deactivation, but dissolution of the alumina causes deactivation as well, since this potentially releases the silver particles [25, 26].

Thermal degradation of the catalyst is the loss of active surface area as a result of a high reaction temperatures, since sintering and aggregation or Ostwald ripening of the silver particles takes place. As a result, the total surface area of the silver decreases, leading to a decreased activity of the catalyst. Additionally, high temperatures may cause loss of active surface area by chemical transforming active sites into non-active sites or by inducing collapses of the alumina support material. [27]

3 Aims

The aims of this project are divided into two parts. The first aim is to synthesize, characterize and optimize ordered macroporous α-alumina and to use this material as support material to synthesize a catalyst consisting of large silver particles (60 - 100 nm) deposited in the cages of the α-alumina. The second aim is to gain better insight in how this catalyst influences the epoxidation of ethylene. This is done by comparing this catalyst (surface area: 20 m^2/g) to catalysts synthesized using commercial α-aluminas (surface area: 1 m^2/g and 8 m^2/g) in terms of stability, activity and selectivity.

In Figure 7, the synthesis route of ordered macroporous α-alumina is shown. In order to synthesize macroporous support material, first a template material is synthesized. PMMA spheres assembled into a colloidal crystal are used as sacrificial template for the synthesis of ordered macroporous α-alumina. After the support material is prepared, silver particles are deposited onto the support material by incipient wetness impregnation and the obtained catalyst is tested in the epoxidation of ethylene.

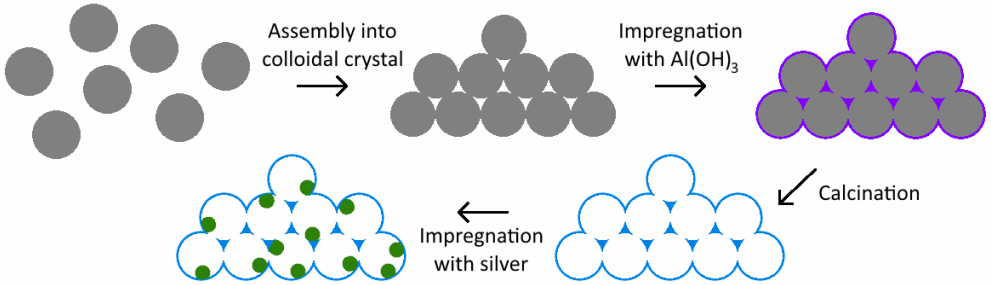

Figure 7: Schematic representation of the synthesis of ordered macroporous α-alumina (blue), in which colloidal crystals of PMMA spheres (gray) are used as sacrificial template and impregnated with aluminum hydroxide (purple). After synthesis, the support is impregnated with silver (green) in the last step.

The aims of this research are presented by the following research questions:

1. Which of the following synthesis methods provides the best PMMA spheres in terms of monodispersity and yield? Surfactant-free emulsion polymerization, oil-in-water solvent evaporation or water-in-oil solvent evaporation.
2. Which of the following methods gives the most ordered colloidal crystals? Centrifugation or solvent evaporation.
3. Are colloidal crystals consisting of PMMA spheres thermally stable enough to be used directly as template for the synthesis of macroporous α-alumina?
4. What are the characteristics (for example morphology and pore structure) of the obtained alumina when colloidal crystals are used as template?
5. Is it possible to distribute monodisperse silver particles equally into the pores of the support material?
6. What is the influence of ordered macroporous α-aluminas as support material on the stability, activity and selectivity of the silver particles in the epoxidation reaction of ethylene?

4 Characterization techniques

For characterization, dynamic light scattering (DLS), thermogravimetric analysis (TGA), mass spectroscopy (MS), transmission electron microscopy (TEM), (focussed ion beam) scanning electron microscopy (SEM/FIB-SEM), X-ray diffraction (XRD), N_2 physisorption, mercury intrusion, ultraviolet - visible light (UV-VIS) spectroscopy, gas chromatography (GC) and differential scanning calorimetry (DSC) are used.

The size of the PMMA spheres is measured with DLS and by using GPC, the chain length of the PMMA molecules is determined. The decomposition temperature of PMMA colloidal crystals is determined with TGA and MS is used to the characterize the decomposition products. DSC is used to determine the phase transition temperature of the PMMA colloidal crystals. With XRD, the crystallinity of the alumina materials are determined, EM is used to look at the morphology and size of the alumina pores and at the size and distribution of the PMMA spheres and silver particles. The pore volume and surface area of the alumina is measured by using N_2-physisorption and mercury intrusion. By using UV-VIS spectroscopy, optical properties are measured. Furthermore, this technique was used as bulk characterization method to compare the quality of the cage structure of macroporous alumina materials. The TPR/TPO setup is used to calcine impregnated colloidal crystals in a reactor. The obtained products of the epoxidation reaction of ethylene are determined by using GC.

The following list contains the used devices:

- DLS: ALV/LSE-5003
- GPC: Alliance Waters 2695 Separations module
  RI detector: Waters 2414, UV detector: Waters 2487 dual λ (254 nm)
- TGA: Perkin Elmer Thermogravimetric Analyzer Pris 1
  MS detector: Knick Präzisions-spanningsgeber
- XRD: Bruker D2 Phaser (Cu or Co source) and D8 advance (Co source)
  Co source is generally used. When the Cu source is used, this is indicated.
- SEM: FEI Phenom and FEI XL30 FEG
  FEI XL30 FEG is generally used. When the FEI Phenom is used, this is indicated.
- FIB-SEM: Nova-NanoLab600
- TEM: Tecnai12 iLem and Tecnai12 iCor
- TPR/TPO: Micromeritics Autochem II RS232 chemisorption Analyzer
- N_2-physisorption: Micromeritics TriStar Surface Area and Porosity Analyzer
- Mercury intrusion: Micromeritics AutoPore IV 9500
- UV-VIS: Varian Cary 500 scan
- UV-VIS microscope: Craic AX10
- DSC: Mettler Toledo

5 Part I: Synthesis of template material

In this chapter, the synthesis and characterization of PMMA spheres and the assembly of these spheres into a colloidal crystals is described. These spheres are used as template material for ordered macroporous α-alumina in Chapter 6. Polymethyl methacrylate (PMMA) spheres are synthesized by surfactant free emulsion polymerization (SFEP). The PMMA spheres were assembled into a colloidal crystal by solvent evaporation and centrifugation. First the formation of PMMA spheres is described, afterward, experimental data of this synthesis is given and finally the results are presented and discussed. Aside from using SFEP, oil-in-water solvent evaporation (OIW) and water-in-oil solvent evaporation (WIO) were used to synthesize PMMA spheres. These methods were not suited for the synthesis of large quantities of PMMA spheres. A description of these methods, experimental data and obtained results can be found in Appendix A.

5.1 Methods

5.1.1 Surfactant free emulsion polymerization

A commonly used method to synthesize PMMA spheres is by surfactant free emulsion polymerization, from methyl methacrylate (MMA). The MMA molecules are dispersed as small droplets in water. The amount and size of these MMA droplets depends on the concentration and type of the solvent, initiator and monomer, on the temperature and on the stirring rate [28]. During polymerization, MMA molecules are linked together in long polymer chains. These PMMA chains are confined in the small droplets which first consisted of MMA. Therefore, the size of the droplets defines the size of the PMMA spheres. [6]

In Figure 8, the reaction mechanism of the polymerization is shown. First, the initiator decomposes into two free radicals at elevated reaction temperature (70 - 80 °C) (1). During the initiation step (2), the free radical reacts with a MMA molecule, in which the C=C double bond is broken and a new radical is formed. This radical reacts with the next MMA molecule in the propagation step (3). This process is repeated n times (4), until a termination step takes place. Most times, the polymerization is terminated by the formation of a paired electron bond by two radicals (5). Alternatively, two separate molecules are formed when a hydrogen atom is transferred from one molecule to another (chain transfer). [28]

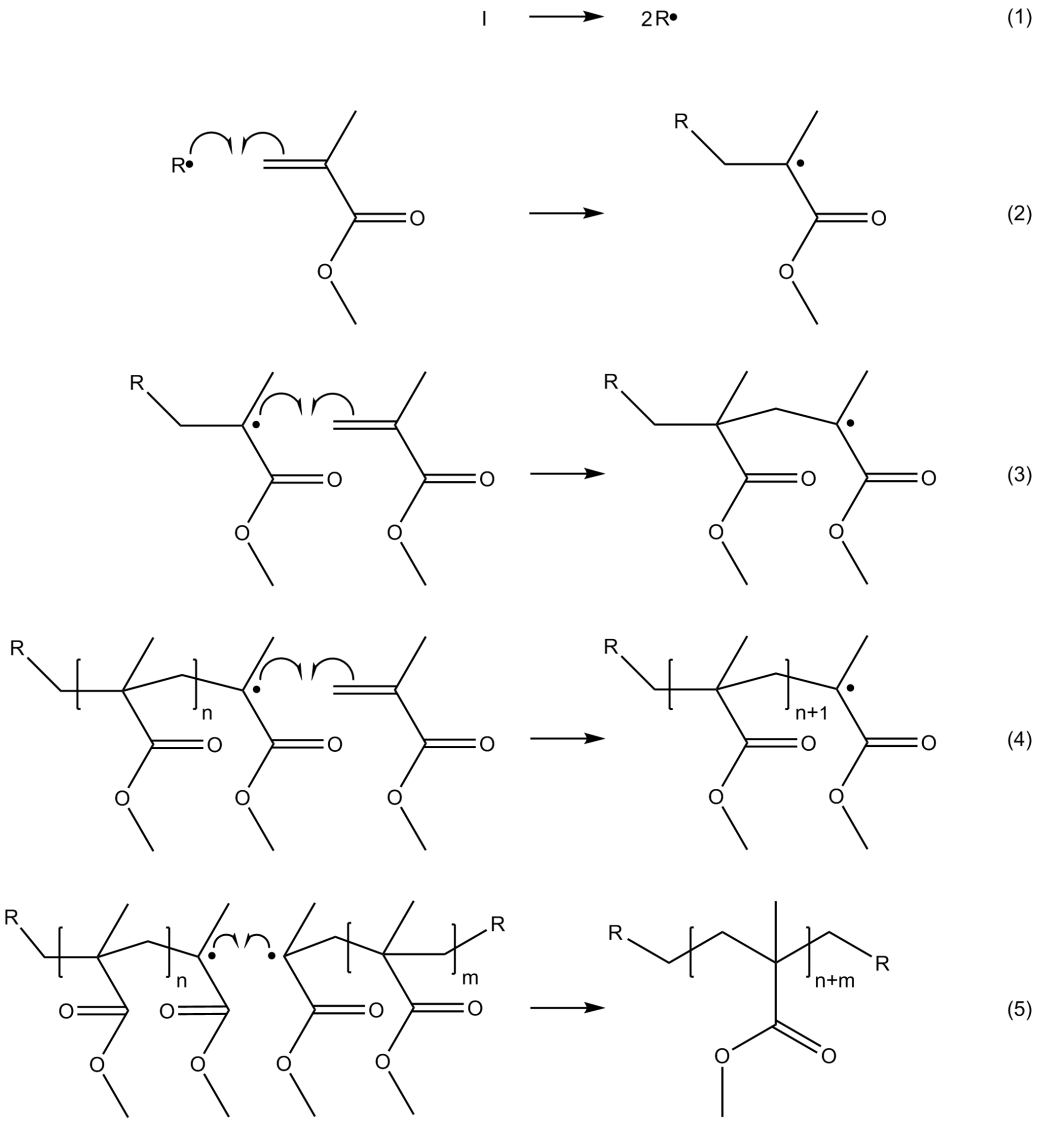

Figure 8: Reaction mechanism of the polymerization of methyl methacrylate (MMA). First, two radicals (R•) are formed by decomposition of the initiator (I) (1). These radicals react with a MMA molecule during the initiation step (2). Consequently, the C=C double bond is broken and a new radical is formed, which reacts with another MMA monomer during the propagation step (3). After this step is repeated *n* times (4), the polymerization is ended by the termination step, for example by combination of two radicals (5).

5.1.2 Assembly of PMMA spheres into colloidal crystal

The obtained PMMA spheres are assembled into colloidal crystals by centrifugation or by solvent evaporation. The spheres are stacked upon each other as a consequence of the difference in the density of the spheres and the solvent in which they are dispersed. When solvent evaporation is used, the dispersion is set aside and over time the solvent slowly evaporates, sedimenting the PMMA spheres. The colloidal crystal of PMMA spheres grows slowly as more solvent evaporates. By using centrifugation, the sedimentation process is sped up.

5.2 Experimental

5.2.1 Chemicals

In Table 1, the used chemicals for the synthesis of PMMA spheres using SFEP are listed. The chemicals were used as received, no extra purification was applied.

Table 1: Used chemicals, their formula and supplier.

Chemical	Formula	Supplier
Methyl methacrylate (MMA) (99 %)	$H_2C{=}C(CH_3)COOH_3$	Sigma-Aldrich
Potassium persulfate (KPS) (99.5 %)	$K_2S_2O_8$	Merck
Azobisisobutyronitrile (AIBN) (98 %, $\leq$ 30 ppm MEHQ)	$(CH_3)_2C(CN)N{=}NC(CH_3)_2CN$	Sigma-Aldrich

5.2.2 Synthesis of PMMA spheres

Surfactant free emulsion polymerization
The synthesis of PMMA spheres via SFEP is based on the procedure described by Zou *et al.* and Schroden *et al.* [29, 30]. In a typical reaction, 100 mL MMA and 400 mL demiwater were added to a 1L three-neck round bottom flask and this was stirred by a mechanical overhead stirrer at 450 rpm. The mixture was heated in an oil bath to 70 °C and a nitrogen flow was present for at least half an hour to deactivate the inhibitor present in the MMA by removing oxygen. After the temperature was stabilized, 0.069 g KPS dissolved in 20 mL demiwater was added to the MMA/water mixture (final concentration KPS: 0.0005 M). The mixture was left to react for 185 min. Afterward, the stirring was stopped and the flask was set aside to cool down. Finally, the PMMA dispersion was filtered trough a glass filter to remove any large chunks of PMMA and the dispersion was stored in a plastic bottle. The same synthesis can be performed using of an azo-compound as initiator instead of KPS, as was described by Schroden *et al.* [31]. We choose to use AIBN, and used 0.35 g to get a final concentration of 0.002 M. A complete overview of all performed syntheses is shown in Table 2.

Table 2: Performed syntheses SFEP.

No.	Initiator	Time	Temp	Result
1	KPS	285 min	70 °C	70 g 570 nm PMMA spheres‡
2	KPS	120 min	70 °C	27 g 350 nm PMMA spheres‡
3	AIBN	60 min	65 °C†	Slurry
4	AIBN	70 min	65 °C	Slurry
5	AIBN	80 min	65 °C†	Slurry + 0.1 g 400 nm PMMA spheres‡
6	AIBN	90 min	65 °C†	Hard block PMMA
7*	AIBN	120 min	65 °C†	Hard block PMMA

*Stirring bean used instead of mechanical overhead stirrer.
† Temperature oil bath could have been inhomogeneous.
‡ Size obtained using DLS

5.2.3 Assembly of PMMA spheres into colloidal crystal

Centrifugation
The PMMA dispersion was centrifuged for 20 hours at 3000 rpm. Afterward, the supernatant was decanted and the formed crystal was dried several days at room temperature. The crystal was crushed slightly into a powder and stored in a bottle.

Solvent evaporation
A small amount of PMMA dispersion was transferred into a bottle. The bottle was set aside whereupon the solvent slowly evaporated over time, sedimenting the PMMA spheres. After several days, all solvent was evaporated and a crystal was obtained.

5.2.4 Characterization

DLS samples were prepared by diluting PMMA dispersions with demiwater. SEM samples were prepared either by depositing a droplet of PMMA dispersion or depositing dried PMMA colloidal crystals on a carbon sticker attached to the sample stub. The samples received a sputter coating of platinum and palladium with a thickness of 10 nm for better conductivity. For GPC measurements, 25 mg PMMA colloidal crystals were dissolved in 5 mL THF and this solution was filtered trough a 0.45 μm filter. A wavelength of 254 nm was used in the UV detector. For TGA measurements, the sample was prepared by mixing PMMA colloidal crystals and commercial α-alumina (10 % PMMA by weight). Other characterization techniques used are UV-VIS spectroscopy and DSC.

5.3 Results and discussion

5.3.1 Synthesis of PMMA spheres

Surfactant free emulsion polymerization
Approximately 70 g of monodisperse PMMA spheres was obtained (Figure 9) by using KPS to initiate the polymerization reaction of MMA (Synthesis 1, Table 2).

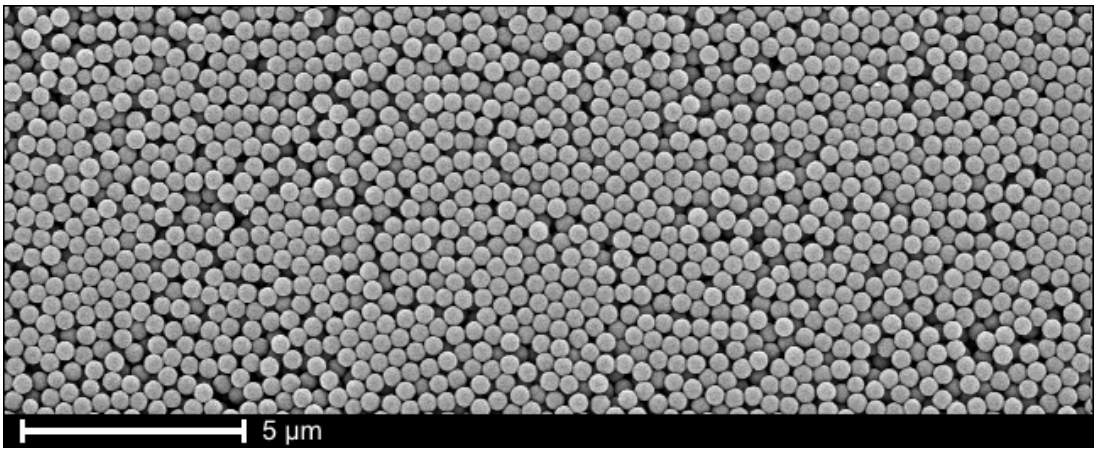

Figure 9: SEM picture of the monodisperse PMMA spheres obtained in Synthesis 1, Table 2.

The size of the spheres was measured both with DLS and SEM. Using DLS, a size of 570 nm was measured with a narrow size distribution (± approximately 1 nm) and using SEM, a size of 416 nm ± 17 nm was measured (104 particles counted). The size measured using DLS was larger compared to the size measured using SEM, since by using DLS, the PMMA spheres in dispersion were measured. As a result of this, both the particle and its ionic sphere were measured, whereby the size of this ionic sphere is unknown. Since by using SEM dried PMMA spheres were measured, the particle size obtained using SEM is more reliable.

The molecular weight of the PMMA molecules was determined using GPC. Both an ultraviolet light and a refractive index detector were used to detect polystyrene molecules of various molecular weights (calibration curve) and the PMMA sample. The molecular weight corresponding to the retention time of the PMMA sample was extrapolated in the calibration curves, since the molecular masses of the PMMA molecules were much larger than the molecular masses of the polystyrene in the available calibration solutions (580 - 371100 g/mol). The calibration curves can be found in Figure A51 (Appendix A). The average molecular weight of the PMMA molecules is approximately $6.8 \cdot 10^5$ g/mol. A more accurate molecular weight of the PMMA molecules might be obtained when a calibration curve is used with standards close to the weight of the PMMA sample.

When the reaction time during the synthesis was shortened (Synthesis 2, Table 2), the obtained spheres were smaller in size (350 nm, measured using DLS), and less PMMA spheres were formed (approximately 27 g). About 50 mL of MMA was still present in the reaction mixture after the reaction was stopped, as is shown in Figure 10A. Probably, the reaction time was too short to polymerize all present MMA. This resulted in smaller PMMA spheres with a larger size distribution compared to Synthesis 1, as is shown in Figure 10B. Instead of changing the reaction time, the particle size of the PMMA can be varied by adjusting reaction parameters such as the concentration MMA or the reaction temperature.

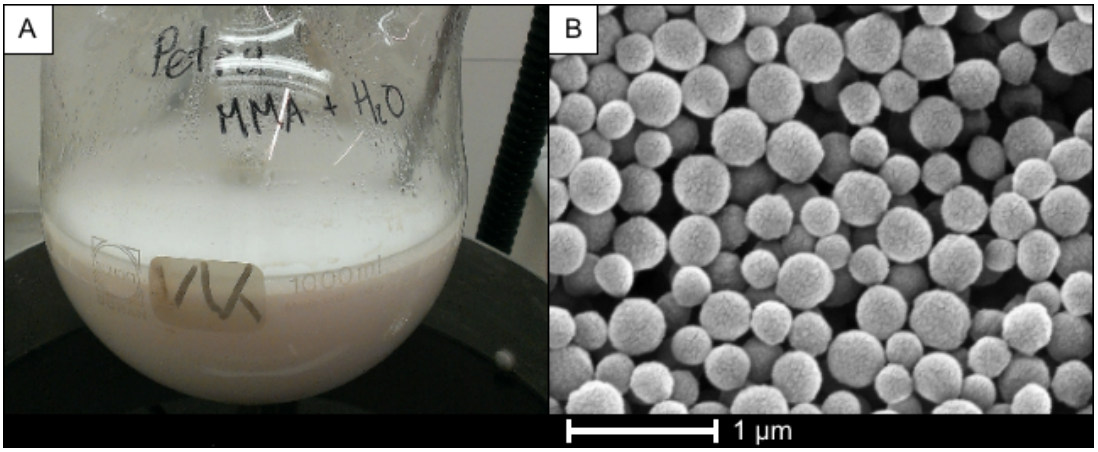

Figure 10: Pictures of the obtained PMMA spheres in dispersion (Synthesis 2, Table 2), with a layer of leftover MMA on top (A) and the PMMA spheres measured with SEM (B). Spheres with a larger size distribution were obtained, compared to Synthesis 1.

In syntheses 3 - 7, AIBN was used to initiate the polymerization reaction. The results of these reactions are shown in Figure 11. When the reaction times were 60 to 80

min (Synthesis 3, 4 and 5), the obtained mixture contained a very low concentration of PMMA spheres in dispersion on top of a thick slurry of PMMA. Since the PMMA spheres were not charged, the spheres were not stabilized and therefore, most spheres aggregated, and a thick slurry was formed. When the reaction time was increased (Synthesis 6 and 7), this slurry transformed into a hard block of PMMA. Since AIBN was not able to stabilize the formed spheres, this was not a suitable initiator for the synthesis of PMMA spheres.

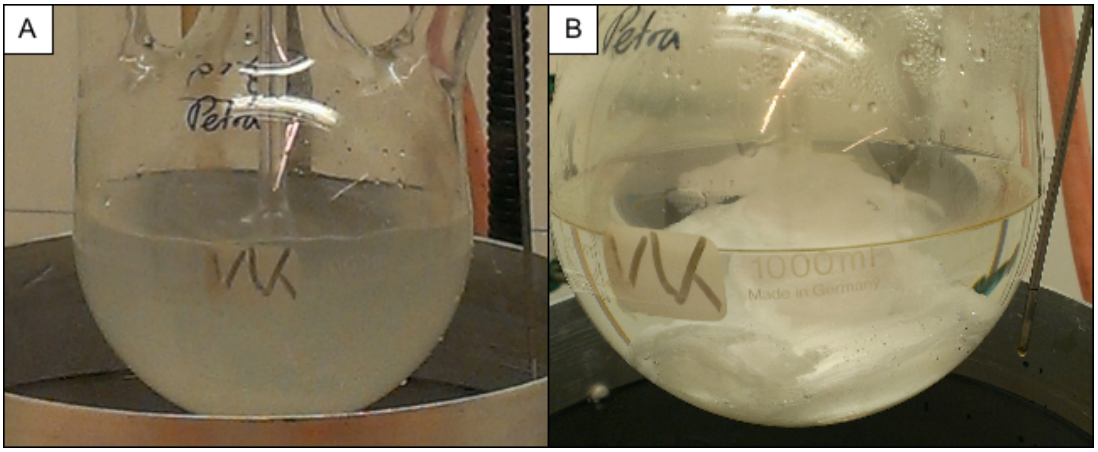

Figure 11: Pictures of the obtained PMMA slurry (A) and the large block of PMMA (B) synthesized using AIBN as initator.

5.3.2 Colloidal crystals of PMMA

Both by using solvent evaporation and centrifugation, the spheres were arranged in an ordered fashion into a colloidal crystal. Using SEM, ordering of the crystals was visualized (Figure 12). Although the crystals obtained by using solvent evaporation seem to contain less defects, centrifugation was used to synthesize colloidal crystals, since centrifugation was much faster.

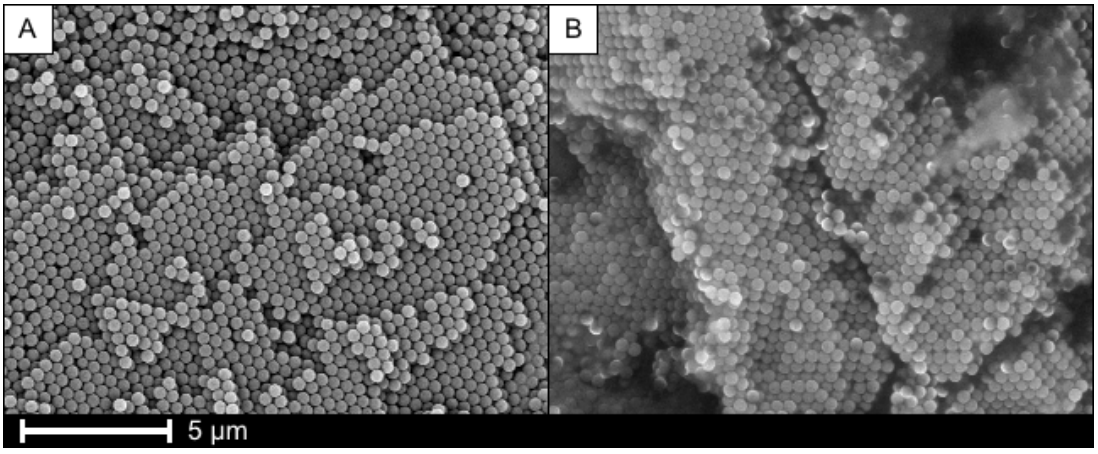

Figure 12: SEM pictures of colloidal crystals of PMMA spheres, assembled by solvent evaporation (A) and assembled by centrifugation (B).

Since the size of the spheres were in the range of visible light and the spheres were arranged in an ordered fashion, optical characteristics as a result of this ordering were present. An UV-VIS spectrum was taken of the PMMA colloidal crystals, this spectrum is shown in Figure 13.

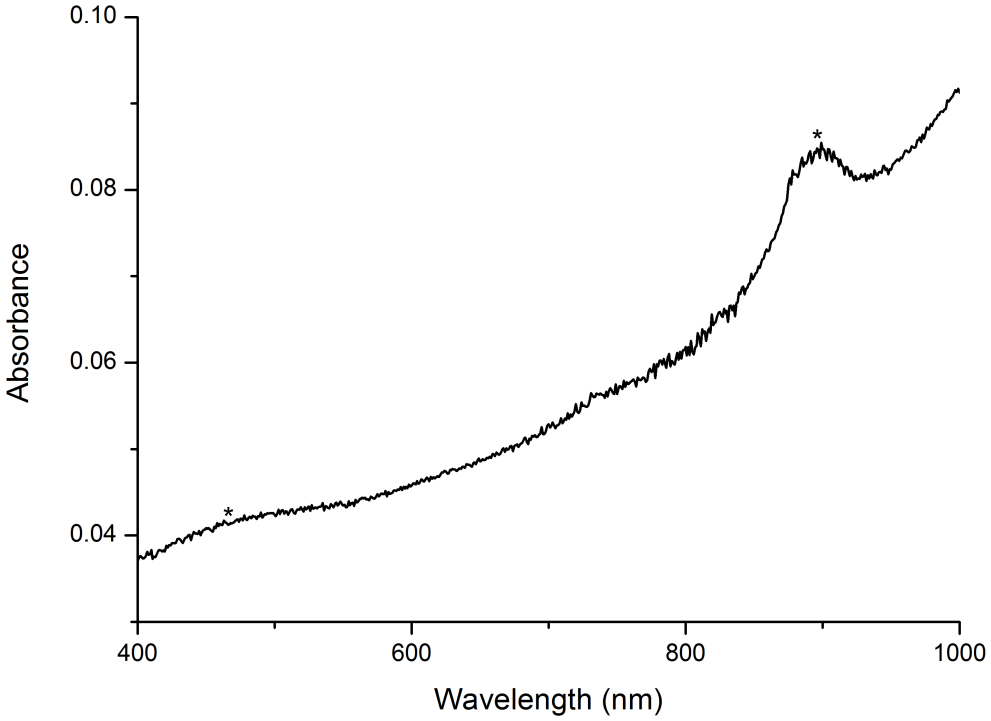

Figure 13: UV-VIS spectrum of the PMMA colloidal crystals, in which two peaks are visible and indicated with $\star$. The peak at 890 nm corresponds to 400 $\pm$ 5 nm PMMA spheres [32]. Part of the spectra (800 - 1000 nm) is corrected for changing lamps.

Besides the obvious peak at 890 nm, a second peak around 465 nm may be present. By combining the derivative of Bragg's law with Snell's law, an equation for the particle size of the PMMA spheres is produced, which is shown in Equation 5 [30, 32].

$$\lambda_{\max} = \frac{2d_{hkl}}{m}\sqrt{n^2_{\text{material,avg}} - n^2_{\text{air}} * sin^2\theta} \tag{5}$$

$\lambda_{\max}$ is the wavelength of the maximum of the peak, d_{hkl} is the interplanar spacing, which is $0.8165D$ for FCC crystals, where D is the particle size. θ is angle between the incident light and the surface normal of the material. Since the material is oriented randomly, θ is set at 0 [30, 32]. m is the order of the Bragg's diffractions and n is the average refractive index, which is 1 for air. Equation 5 is rewritten in Equation 6.

$$D_{\text{spheres}} = \frac{m * \lambda_{\max}}{1.633 n_{\text{material,avg}}} \tag{6}$$

$n_{\text{material,avg}}$ is calculated using Equation 7. For PMMA spheres in a FCC crystal, the fraction of PMMA, $f_{\text{PMMA,bulk}}$, is 0.26 and the fraction of air, f_{air}, is 0.74. $n_{\text{PMMA,bulk}}$ is 1.492 at 25 °C [32], which gives $n_{\text{PMMA,avg}}$ a value of 1.364.

$$n_{\text{material,avg}} = n_{\text{material,bulk}} * f_{\text{material,bulk}} + n_{\text{air}} * f_{\text{air}} \tag{7}$$

For the determination of the size of the PMMA spheres, the peak at 890 nm is used, which is most likely produced by the first order Bragg's diffractions ($m = 1$). By using in Equation 6, the calculated size of the PMMA spheres is 400 $\pm$ 5 nm. This is around the same size as measured using SEM, indicating that these techniques are more reliable compared to DLS. The second peak around 465 nm could be caused by the second order Bragg's diffractions ($m = 2$).

Since the PMMA is used as sacrificial template, the melting point and decomposition temperature of the PMMA colloidal crystals might influence the synthesis of the macroporous alumina. Differential scanning calorimetry (DSC) measurements were performed on the PMMA colloidal crystals to determine the melting point of the crystals. These measurements were performed twice, using the same batch PMMA colloidal crystals. In Figure 14, the energy increase or decrease at certain temperatures is shown, in which the black and red curves belong to one sample and the blue and green curves belong to another sample. The increase or decrease in energy is a result of phase transitions in the material, and therefore the height of the peaks are dependent on the amount of sample measured.

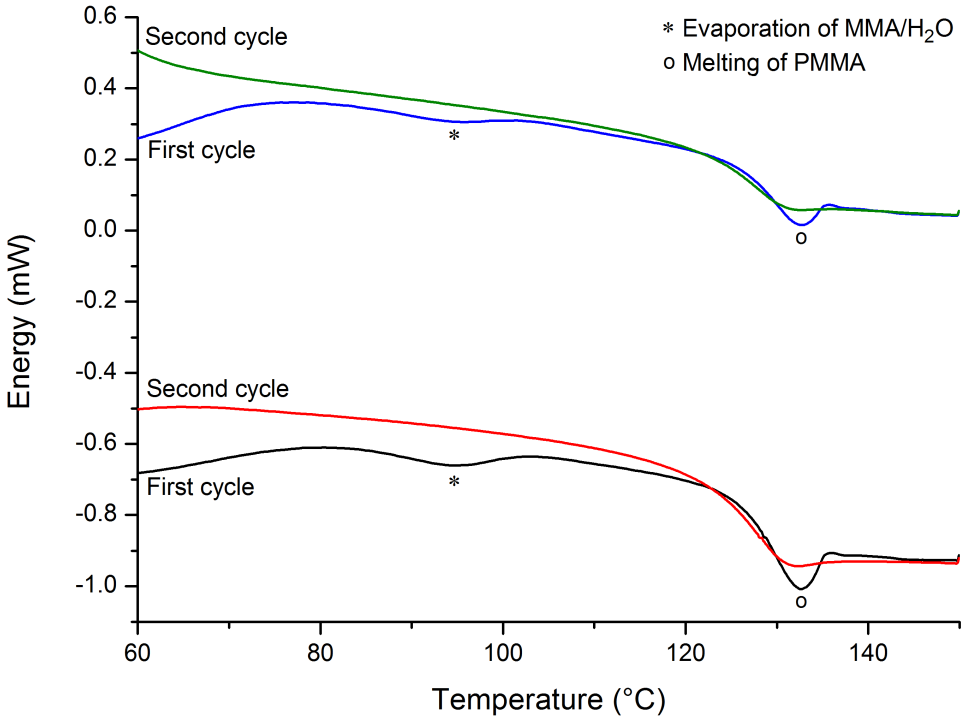

Figure 14: DSC curve of two samples containing PMMA colloidal crystals in which the black and red curves belong to one sample and the blue and green curves belong to another sample. During the first cycle, MMA and H_2O still present in the crystals evaporated around 95 °C (indicated by $*$). Therefore, this peak is not observed in the second cycle. The melting point of the PMMA colloidal crystals was around 130 °C (indicated by $\circ$). The increase in energy measured in the beginning of the first cycle is caused by the imbalance of heat capacity between the sample and reference (start-up hook).

To obtain the black and red curves, 10.3 mg of PMMA colloidal crystals were used, whereas to obtain the blue and green curves, 6.3 mg of PMMA colloidal crystals were used. The PMMA colloidal crystals were heated twice from 50 °C to 150 °C, with 5 °C/min, whereupon the material was cooled down again to 50 °C (20 °C/min). First, around 95 °C, residual MMA and H_2O evaporates (indicated by $*$). Around 130 °C, the PMMA melted (indicated by $\circ$). When the material was cooled down afterward, the PMMA solidified again. During the second heating cycle, the peak around 95 °C is no longer observed, since the MMA and H_2O is already evaporated during the first cycle. The melting point of the PMMA colloidal crystals is again present around 130 °C. The change in the shape of this peak between the first and second heating cycle, indicates that during the first heating cycle part of the material melted and part of the material evaporated, whereas during the second heating cycle only material melted. H_2O and MMA could be entrapped in the crystals, which was released when the PMMA colloidal crystals melted at 130 °C. When the obtained value of the melting point is compared to literature, this is slightly higher than values found in literature, where values of 120 - 125 °C were presented [33, 34].

Using thermogravimetric analysis (TGA), the decomposition temperature of the PMMA under air flow was determined. The decomposition curve (Figure 15) shows that the decomposition started at 250 °C. The decomposition temperatures of PMMA presented in literature are moderately higher (300 - 400 °C) [33, 34]. At 400 °C, all PMMA seems to be decomposed. The values of these melting and decomposition temperatures are used to clarify differences in obtained alumina materials in Sections 6.3.3 and 6.3.6.

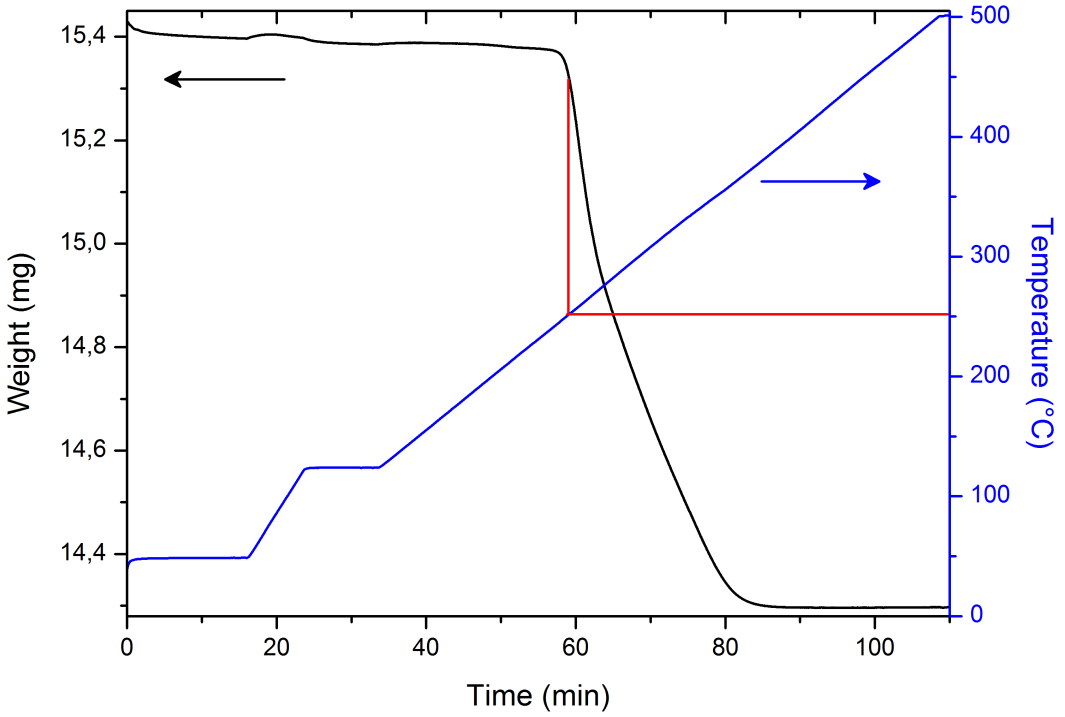

Figure 15: TGA of the PMMA colloidal crystals in air flow, heating ramp: 10 °C/min (5 °C/min up to 125 °C). The red line indicates the start of the decomposition, which is at 250 °C.

6 Part II: Synthesis of support material

In this chapter, the synthesis, characterization and optimization of ordered macroporous α-alumina is described. The materials are synthesized by using the PMMA colloidal crystals obtained in Chapter 5. The macroporous α-alumina obtained in this chapter is used as support material for silver particles in Chapter 7. First, the synthesis method is explained, whereupon experimental details are given. Finally, the obtained materials are characterized and discussed.

6.1 Methods

6.1.1 Synthesis of ordered macroporous α-alumina

Three-dimensional ordered macroporous (3-DOM) α-alumina can be produced via sol-gel chemistry by using colloidal crystals composed of PMMA spheres as hard template [16]. A schematic representation of vacuum-assisted infiltration is shown in Figure 16. In this method, the vacuum helps to remove the excess of aluminum precursor after the voids of these crystals are filled. A thin layer of colloidal crystals is deposited onto a filter paper in the büchner funnel and precursor is drop-wise added to completely wet the crystal. [35]

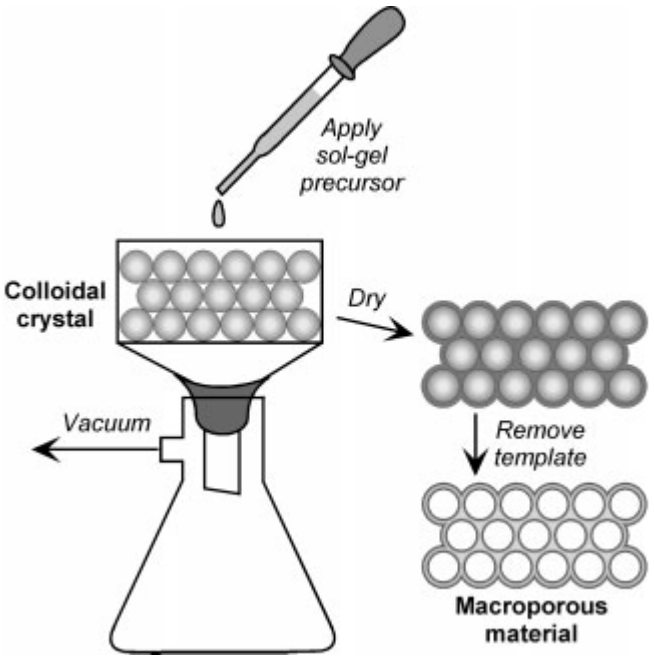

Figure 16: Schematic representation of the synthesis of ordered macroporous materials. By soaking a colloidal crystal in an aluminum precursor, the voids between the spheres are filled. The excess of precursor is removed by vacuum filtration, whereupon the material is dried. After drying, the template is removed by calcination. [35]

When an aluminum hydroxide slurry or a dispersion of α-alumina seed crystals is used as precursor, the bulk of the crystals is not penetrated and therefore, the voids stay empty [16]. However, aluminum nitrate can be used to fill all voids and after addition of ammonium hydroxide, aluminum hydroxide is formed in the voids. The aluminum

hydroxide is transformed into α-alumina and the template material is burned away during a calcination at 1150 °C. In Figure 17, a colloidal crystal of PMMA spheres (A) and the obtained 3-DOM α-alumina using these PMMA spheres (B) synthesized by Sokolov *et al.* are shown. [16]

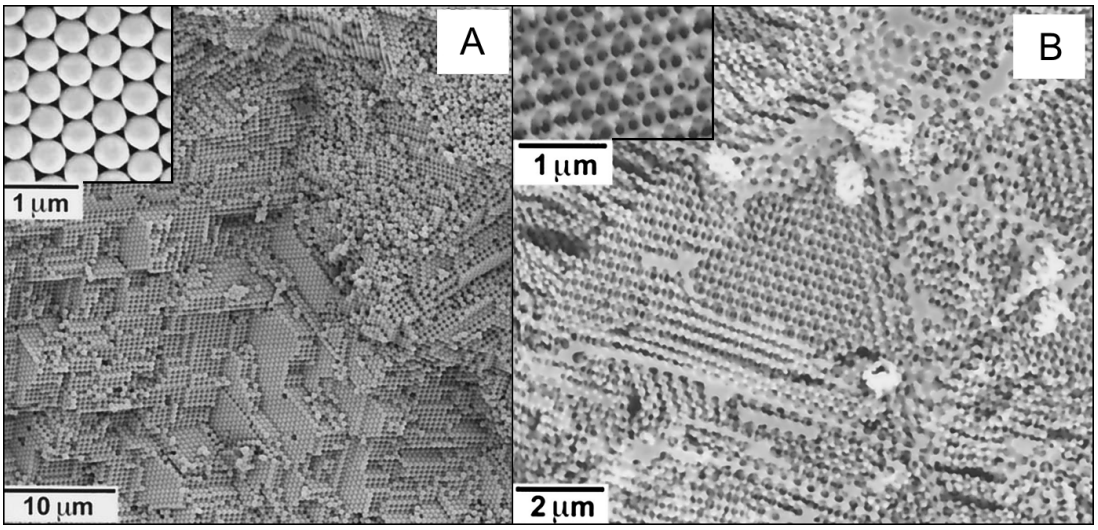

Figure 17: TEM pictures of (A) a colloidal crystal of PMMA spheres and (B) the inverse replica of (A), 3-DOM α-alumina. [16]

6.2 Experimental

6.2.1 Chemicals

In Table 3, the used chemicals for the synthesis of alumina are listed. The chemicals were used as received, no extra purification was applied.

Table 3: Used chemicals, their formula and supplier.

Chemical	Formula	Supplier
Aluminium nitrate nonahydrate (98+ %)	$Al(NO_3) \cdot 9\ H_2O$	Fluka Analytical
Ammonia (28-30 %)	NH_3	Sigma-Aldrich
Methanol (99+ %)	CH_3OH	Acros Organics

6.2.2 Synthesis of ordered macroporous α-alumina

The synthesis of ordered macroporous α-alumina is based on the procedure described by Sokolov *et al.* [16]. The cage structure of the α-alumina obtained using this method was best preserved compared to other synthesis performed. 1.5 g PMMA colloidal crystals, prepared in Section 5.2.3, was transferred into a büchner funnel. A 1 M aluminum nitrate nonahydrate solution in a 1:1 volume mixture of demiwater and methanol was used as precursor solution. Approximately 3 mL of this solution was added to completely cover the PMMA colloidal crystals. After 2 minutes of soaking

time, the excess of solution was removed by vacuum suction. By drying the crystals, the precursor solution outside the voids of the PMMA colloidal crystals was removed. After 20 minutes, the PMMA colloidal crystals were dry and the suction was turned off. To convert the aluminum nitrate into aluminum hydroxide, the PMMA colloidal crystals were soaked for 2 min in approximately 3 mL of 1:1 volume mixture of methanol and ammonia, in which the PMMA colloidal crystals were again completely covered with solution. Again, the excess was removed and the material was dried by applying vacuum suction for 20 min. These two impregnation steps were repeated three times to increase the amount of aluminum hydroxide in the voids of the PMMA colloidal crystals. Afterward, the PMMA colloidal crystals were set aside to dry even further overnight.

To convert the aluminum hydroxide into alumina, the PMMA colloidal crystals were calcined at 1150 °C (5 °C/min) under nitrogen flow (0.5 - 1 L/min), for 6 hours. To obtain α-alumina, the sample was calcined again at 1150 °C (5 °C/min) under air flow (0.5 - 1 L/min), for 6 hours. During the first calcination, the color of the sample turned from white into blue/black to green/black, during the second calcination the color of the sample turned white.

This synthesis method was adjusted multiple times to investigate the influence of several parameters. These adjustments are described in the following sections. An overview of all performed syntheses is given in Tables B9 and B10 (Appendix B).

6.2.3 Number of impregnation steps applied and larger scale

The influence of the amount of impregnation steps on the structure and amount of alumina formed was tested by impregnating the PMMA colloidal crystals multiple times. Furthermore, this synthesis was performed on a larger scale. An overview of these syntheses is given in Table 4, in which Synthesis 1.5_3_b is the synthesis described in Section 6.2.2 (marked with *). The synthesis method described by Sokolov *et al.* corresponds to Synthesis 1.5_1_a.

Table 4: Influence number of impregnation steps and amount PMMA on yield alumina.

Synthesis	Amount PMMA used (g)	Number of impregnations	Alumina obtained per g PMMA (mg)
1.5_1_a	1.5	1	19
1.5_2_a	1.5	2	31
1.5_3_b*	1.5	3	31
1.5_4_a	1.5	4	41
1.5_3_a	1.5	3†	27
6_3_a	6	3	39
6_3_b	6	3	34

a: Calcined once, air flow, 1150 °C. b: Calcined twice, nitrogen and air flow, 1150 °C.
* Synthesis described in Section 6.2.2.
† PMMA colloidal crystals were soaked three times in an aluminum hydroxide solution and once in an ammonium/methanol mixture instead of three times in both solutions.

PMMA colloidal crystals were impregnated one, two and four times. Additionally, the PMMA colloidal crystals were impregnated three times with the aluminum nitrate solution whereupon the ammonium/methanol mixture was added once. After impregnation, these samples were calcined once under air flow only.

Furthermore, two syntheses were performed using 6 g PMMA. By using a larger amount, the time needed to dry the colloidal crystals in between the impregnation steps increased as a result of increased thickness of the PMMA layer in the büchner funnel. By using a larger büchner funnel, this drying time was again 20 min. Since this amount of PMMA did not fit in one calcination boat, the sample was split in two and calcined separately during the first calcination step under nitrogen flow.

6.2.4 Calcination temperature and atmosphere

In these experiments, the influence of the calcination temperatures and atmospheres was investigated. The PMMA colloidal crystals were impregnated only once with the aluminum nitrate solution and the ammonium/methanol mixture before calcination. The following prepared materials were calcined at 200 °C, 400 °C, 600 °C, 800 °C, 1000 °C or 1150 °C:

1. Aluminum hydroxide without PMMA colloidal crystals present, which were calcined under nitrogen flow for half an hour (the sample calcined at 1150 °C was calcined again at this temperature for three more hours)
2. Impregnated PMMA colloidal crystals which were calcined under air flow for 6 hours
3. Impregnated PMMA colloidal crystals which were calcined under nitrogen flow for 6 hours

The material calcined under nitrogen flow at 1150 °C for 6 hours, was calcined again under air flow at 600 °C, 700 °C, 800 °C and 900 °C.

6.2.5 Pretreatment PMMA colloidal crystals

The influence of drying temperature on the structure of the macropores was researched by using PMMA colloidal crystals dried for several days at 60 °C and 120 °C.

6.2.6 Calcination in combustion boat versus plug flow reactor

Impregnated colloidal crystals were calcined in a plug flow reactor, in which the gas flow was adjusted trough the sample. The material was first calcined for 6 hours at 1090 °C (5 °C/min) under argon atmosphere, whereupon the material was calcined again for 18 hours at 1050 °C (5 °C/min) under an helium atmosphere containing 5 % oxygen. Gas flows of 100 mL/min were used, which is 5 to 10 times as low as the gas flows used in the flow oven. The obtained alumina was calcined a third time in a muffle oven for 2 hours at 1150 °C.

6.2.7 Strength of the macropores

The strength of the pores was investigated by making pellets. A force of 1.5 ton and 3 ton was applied to the macroporous α-alumina.

6.2.8 Characterization

Microtomed material was dispersed in the polymer Epo-Fix cat. #1232 resin and hardener (ratio 2:15), which was placed in an oven at 60 °C overnight to harden. This material was cut in slices and placed onto a TEM grid covered with a thin layer of carbon film. SEM samples were prepared by depositing the alumina material on a carbon film sticker attached to the sample stub. Samples characterized with the FEI XL30 FEG received a sputter coating of platinum and palladium with a thickness of 10 nm for better conductivity. Other characterization techniques used are XRD, UV-VIS spectroscopy (combined with microscopy), N_2-physisorption and mercury intrusion.

6.3 Results and discussion

In this part, the results of the obtained macroporous alumina are presented and discussed. Firstly, the influence of the alumina production at a larger scale and the number of impregnation steps is reviewed, since the products of these larger batches were used for some characterization techniques. Next, the characteristics of the alumina obtained in Section 6.2.2 are discussed. Afterward, the influence of various synthesis parameters are investigated.

6.3.1 Number of impregnation steps applied and larger scale

The calculated maximum amount of alumina what can be obtained using the synthesis method described by Sokolov *et al.* is only 19 mg alumina/g PMMA, assuming all voids of the close packed PMMA colloidal crystals were filled with 1 M aluminum hydroxide. The calculation of this theoretical maximum yield can be found in Appendix B, alongside with the assumptions made. The amount of synthesized alumina in Synthesis 1.5_1_a (Table 4, Section Se:scalestepsalumina) was 19 mg alumina/g PMMA. Although this theoretically gives a yield of 100 %, presumably a very small part of the obtained alumina was non-porous, which increased the density of the obtained alumina material slightly.

By optimizing the method presented by Sokolov *et al.*, the obtained amount of ordered macroporous α-alumina was increased. This was done by applying multiple impregnation steps and by using more PMMA colloidal crystals as start material. SEM was used to visualize the cage structure of the obtained materials. Increasing the amount of PMMA did not seem to affect the cage structure of the alumina, whereas by increasing the amount of impregnation steps, the cage structure seemed to be improved. By applying several impregnation steps, more voids of the PMMA colloidal crystals were filled with aluminum hydroxide, yielding a better preserved cage structure. However, to quantify this, bulk characterization (for example UV-VIS spectroscopy) is needed.

Foremost, both alternations increased the yield of the synthesis, as is shown in Table 4 (Section 6.2.3).

6.3.2 Properties/characteristics of α-alumina

In this section, several characteristics of the obtained alumina in Synthesis 1.5_3_b are described, in which ordered macroporous α-alumina, with the best preserved cage structure, was obtained. As described in the experimental section, alumina was synthesized using two different calcination steps. After the first calcination under nitrogen flow, a black/blue powder was obtained (Figure 18B). The black color originates from a thin layer of carbon which was formed as a result of pyrolysis of the PMMA spheres. The color of the material turned white during the second calcination step under air flow (Figure 18C), since during this calcination the carbon burned off.

Figure 18: Pictures of the impregnated PMMA colloidal crystals (A), the obtained material after the first calcination step (B) and after the second calcination step (C).

The diffractograms of the alumina materials obtained after the first and second calcinations (Figure 18B and C) are shown in Figure 19. After the first calcination, the material consisted mainly of γ-alumina (black line), whereas after the second calcination all alumina was converted into α-alumina (red line). All peaks visible in the red diffractogram correspond to the α-phase of alumina, indicating a high crystallinity of the α-alumina. The larger peaks originate from the κ-α radiation, whereas the smaller peaks originate from the κ-β radiation of the Co source. The peak assigned by $*$ is an artifact, which was observed in some measurements. In Figure B58 (Appendix B), two samples of the same material are shown, in which in one of these diffractograms this peak is observed.

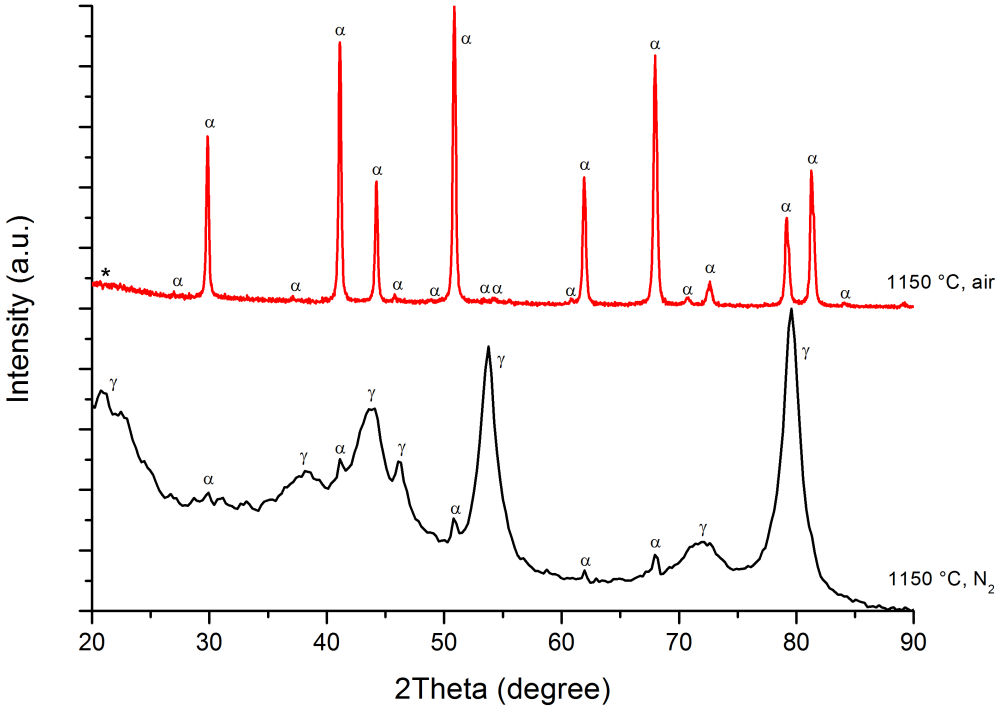

Figure 19: XRD diffractogram of the alumina materials shown in Figure 18A and B. The alumina obtained after the first calcination consisted mostly of γ-alumina, which was converted into α-alumina during the second calcination. The peak assigned by ∗ is an artifact of the XRD measurement.

In Figure 20, SEM pictures of the carbon covered γ-alumina obtained after the first calcination under nitrogen flow (A) and of the white α-alumina obtained after the second calcination under air flow (B) are shown. The ordered macroporous structure is clearly visible in both materials. An overview of the measured pore size, window size and wall thickness of both materials is given in Table 5.

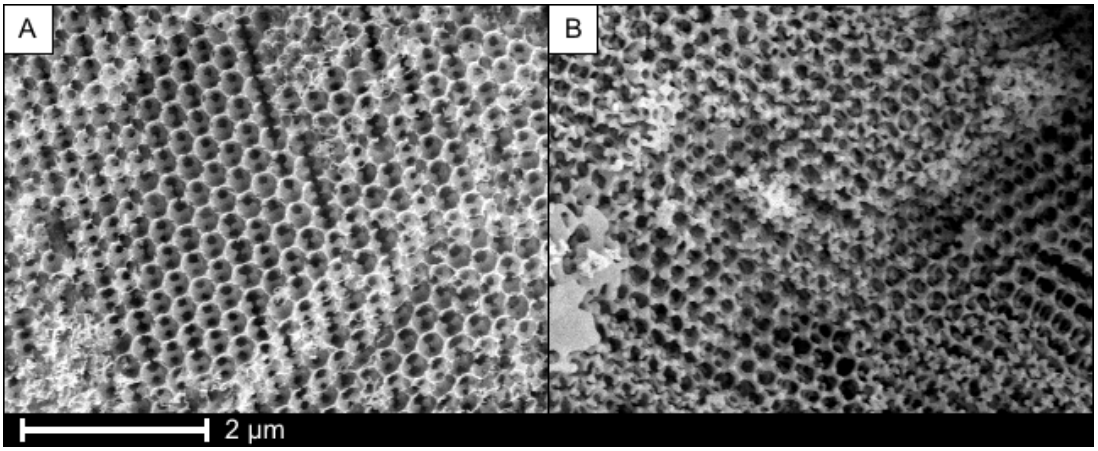

Figure 20: SEM pictures of the obtained carbon covered macroporous γ-alumina (A) and macroporous α-alumina (B).

Table 5: Pore size, window size and wall thickness and their size distributions of carbon covered γ-alumina and of α-alumina. For the pore sizes, 200 pores were measured. For the window sizes and wall thicknesses, 50 - 100 windows and walls were measured. All measurements were performed using iTEM.

Material	Pore size (nm)	Window size (nm)	Wall thickness (nm)
γ-alumina	249 ± 16	83 ± 14	21 ± 5
α-alumina	219 ± 16	104 ± 12	36 ± 6

Since the ordering of the pores in Figure 20 was continuous, Fourier transformations performed using iTEM on these SEM pictures reflected the ordering of the pores. The results are shown in Figure 21. From the distance between the dots, the pore sizes were determined, since the distance indicated in red corresponds to 1 divided by the pore size. This gave pore sizes of 242 nm for the γ-alumina and 217 nm for the α-alumina.

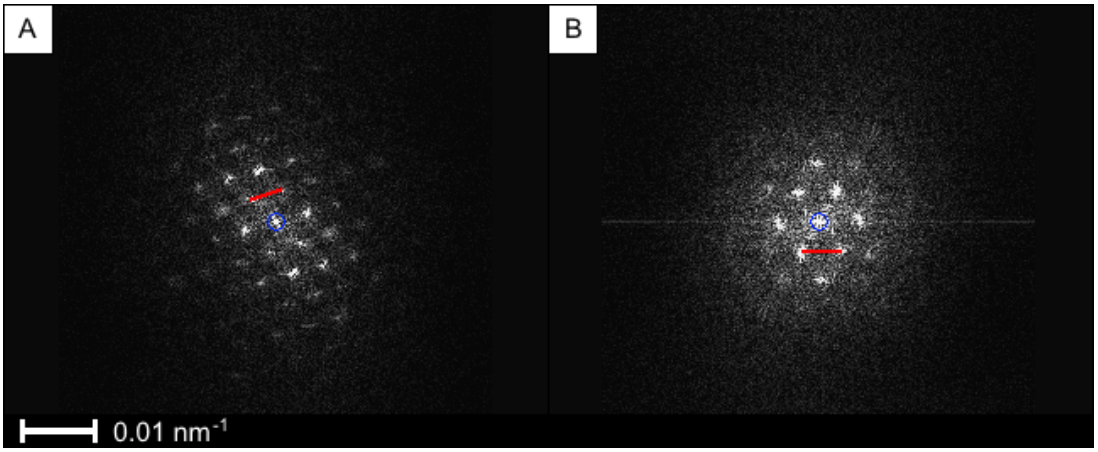

Figure 21: Fourier transform performed on carbon covered macroporous γ-alumina (A) and macroporous α-alumina (B) using iTEM. The SEM pictures shown in Figure 20 were used. The dots represent the ordering of the pores in the materials and the distance between two dots (indicated in red) corresponds to 1 divided by the pore size.

Whereas macropores were observed in all parts of the sample, the cage structure was lost at some places. In Figure 22, a part of the material is visible in which the ordered cage structure was partially not preserved.

By using SEM, only the outside of the particles was visualized, but the pore structure on the inside of the particles could be different. TEM measurements on the alumina particles gave no extra information, since the grain size of most particles was 35 - 90 μm and no pore structure was visible using TEM. Therefore, the inside of the alumina particles was visualized by removing a part of the surface of the particle using FIB-SEM. In Figure 23, FIB-SEM pictures of the γ- and α-alumina are shown. Holes of 7.5 μm deep were made using the ion beam, to expose the pore structure beneath the surface. In Figure 23B, the cage structure inside the particles was even better compared to the cage structure on the surface. This indicates that particles without cage structure visible on the surface, may still contain macropores on the inside.

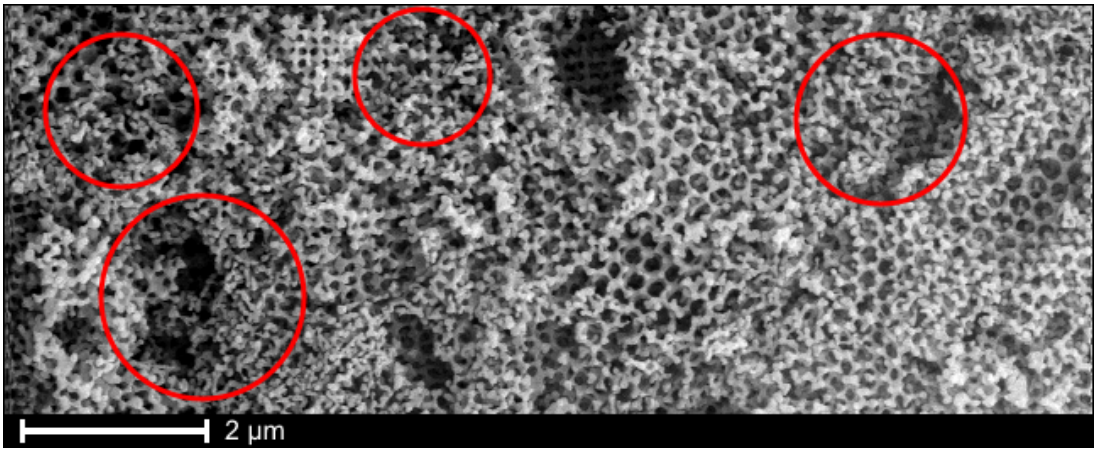

Figure 22: SEM picture of a part of the same sample, where the ordered pore structure was partially not preserved (red circles).

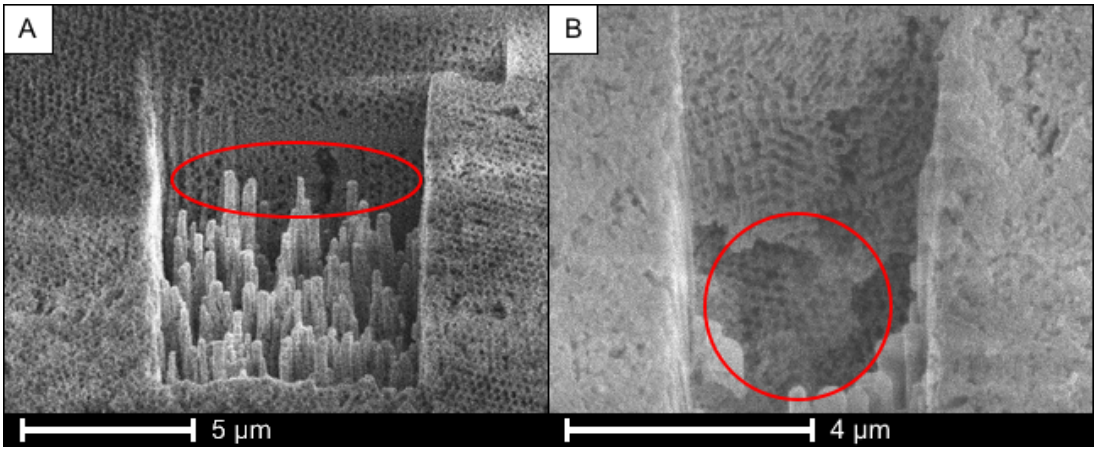

Figure 23: FIB-SEM pictures of carbon covered macroporous γ-alumina (A) and macroporous α-alumina (B), in which 7.5 µm of the alumina top layer was removed using an ion beam. In both pictures, pore structure is visible below the surface of the particles (indicated in red).

Although the pore structure a few microns beneath the surface already gives an indication of the pore structure in the middle of the particle, the particles were microtomed for verification. First, the alumina particles were dispersed in a polymer, whereupon slices of 400 nm were cut. These slices were measured using TEM. One of these slices is shown in Figure 24A, in which two layers of pores are visible on top of each other. In Figure 24B, one of these layers is indicated in red and in Figure 24C the other layer is indicated in blue. In Figure 24D, both layers are indicated.

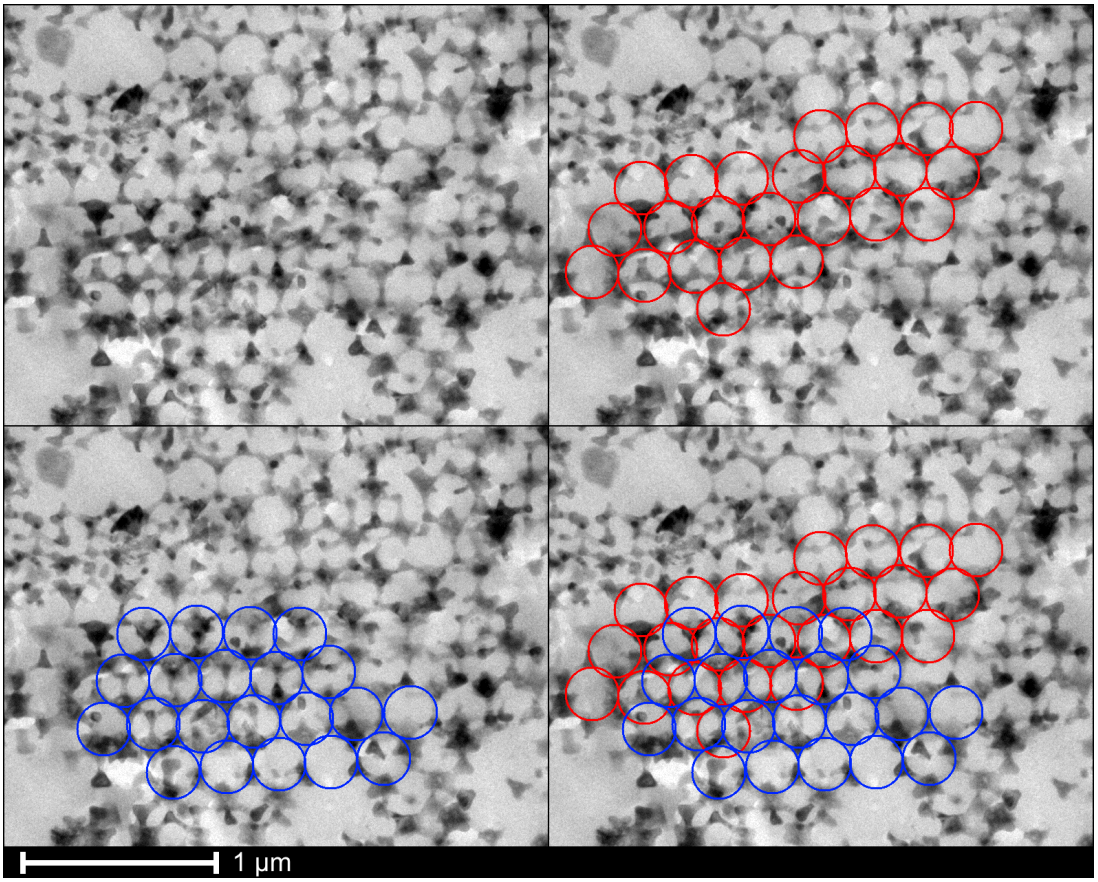

Figure 24: Four times the same TEM picture of microtomed macroporous α-alumina. In B, C and D, two different layers of pores are indicated in red and blue. The thickness of the slides is 400 nm.

As a result of the size of the pores and their ordering, the macroporous alumina had optical properties in the UV-VIS region of light, analogous to the PMMA spheres. By using an UV-VIS microscope, UV-VIS spectra of small parts (50 x 50 µm) of the sample were obtained, in which the measured part of the sample was visualized using the microscope. In Figure 25, both the spectra (A) and the part of the sample which was used for the spectra, visualized using the microscope (B) are shown.

The various colors visible in Figure 25B are due to Braggs reflections as a result of the ordered macropores. The UV-VIS spectrum shows a negative peak around 465 nm, caused by these Bragg's reflections, since the wavelengths around 465 nm are reflected by the pores. Equation 6 (Section 5.3.2) was used to calculate the size of the pores, in which λ_{min} was used instead of λ_{max}, since this material is an inverse structure of the PMMA colloidal crystals. The average refractive index of the macroporous material is calculated using Equation 7 (Section 5.3.2). In macroporous alumina, in which the pores are in an FCC structure, the alumina fills 26 % and air 74 % of the volume. The refractive index of bulk alumina is 1.760, which gives the macroporous α-alumina a refractive index of 1.198 [36]. The calculated pore size of this material is 238 ± 3 nm, which is slightly larger compared to the size measured using SEM.

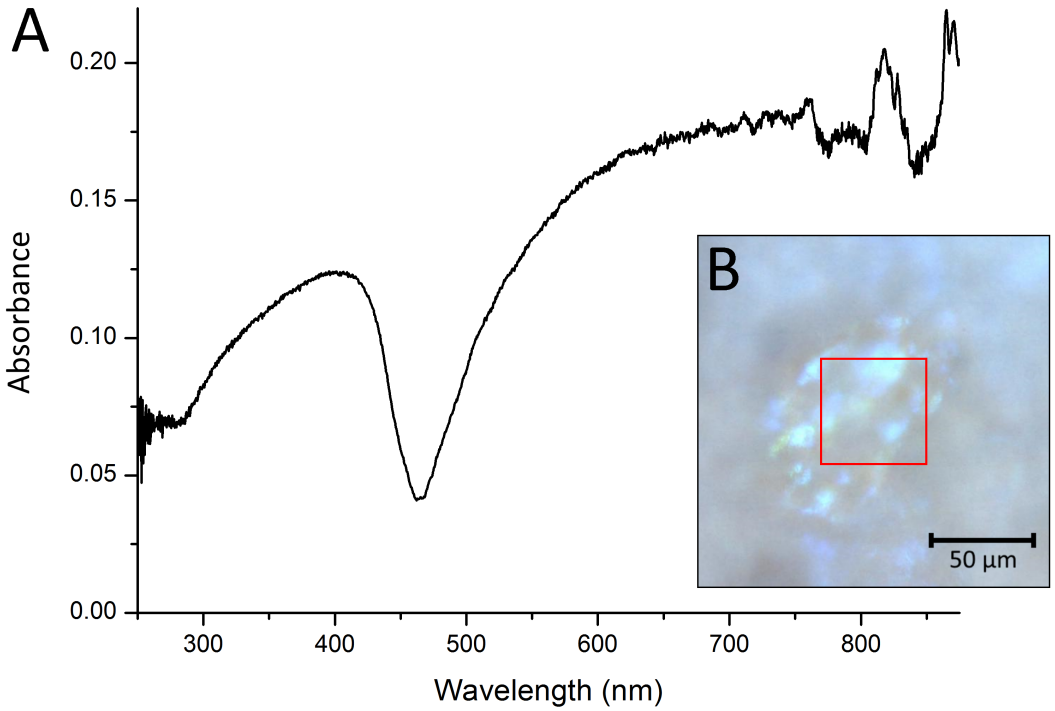

Figure 25: UV-VIS spectrum measured on 50 x 50 µm (red square) of macroporous alumina material (A) and the picture of this part of the material (B). The light around 465 nm is reflected by the ordered macroporous material, which give the material the colors observed in the picture. By using the UV-VIS microscope, only direct reflection was measured.

UV-VIS spectra of other measured areas of this material are shown in Appendix B, Figure B54. Although most parts showed Bragg's reflections, the intensity of the colors measured using the microscope and the difference in absorbance measured using the UV-VIS spectrophotometer was generally less intense compared to the spectrum showed in Figure 25. This is explained by the different orientations of the alumina particles. The differently oriented pores reflect the light in different directions, but only direct reflection was measured using the UV-VIS microscope. Therefore, most times, only a small part of the reflections was collected, which resulted in a less intense reflectance peak. Intense Bragg's reflections were only measured if the material was oriented in the right way.

Since only the direct reflections were measured and only a small part of the sample was measured using the UV-VIS microscope, additional measurements were performed on the macroporous alumina using a regular UV-VIS spectrophotometer, equipped with an integrating sphere to collect all reflected light. To distinguish between peaks originating from the macropores and peaks originating from the sample holder or non-porous α-alumina, a background measurement of the sample holder filled with non-porous α-alumina (1 m^2/gram) was used. The obtained UV-VIS spectra of the macroporous α-alumina is shown in Figure 26, in which a peak is visible at 430 nm. This correlates to a pore size of 220 $\pm$ 5 nm, which is similar to the pore size measured using SEM.

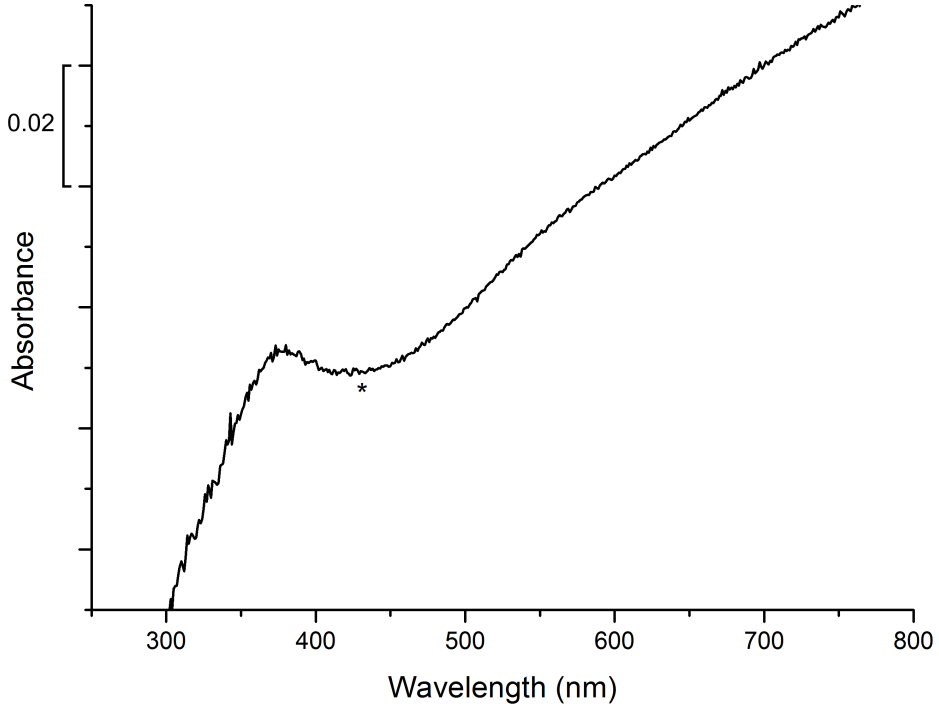

Figure 26: UV-VIS spectrum of the macroporous α-alumina, in which a measurement of a non-porous α-alumina was used as background. The negative peak at 430 nm (indicated with $\star$) corresponds to a pore size of 220 nm. For this measurement, an integrating sphere was used to collect all reflections.

N_2-physisorption and mercury intrusion measurements were performed to determine the surface area, window size and pore volume of the material. The surface area of the material according to N_2-physisorption measurements performed on several macroporous materials is approximately 20 m^2/g. This value is a good indication, but contains a large margin of error (of approximately 5 m^2/g), since only a small amount (max 200 mg) of sample with a relatively low surface area was measured. Although this surface area is very high for α-alumina, it is low compared to other carrier materials.

Although this value is only an approximation, this value is very close to the theoretical surface area of macroporous alumina with pores of 250 nm and windows of 100 nm. This calculated surface area is 17 m^2/g. The calculation for this theoretical surface area can be found in Appendix B, along with the assumptions made and the isotherm of the measured material (Figure B55). The shape of the isotherm indicates that the material contains no micro- or mesopores. This is positive, since these pores would be too small for silver particles, but would provide unwanted hydroxyl groups.

To gain an indication of the pore volume, macroporous alumina (Synthesis 6_3_a, Table 4) was dried at 120 °C. Afterward, water was added dropwise to fill the pores. After 0.0145 g of water was added to 10 mg of alumina, the pores of the material were completely filled, since after one extra drop was added, the material was wet. A simple calculation gives a pore volume of 1.45 mL/g alumina.

For the mercury intrusion measurement, approximately 200 mg of ordered macroporous α-alumina material was needed. Therefore, instead of using the material obtained in

Synthesis 1.5_3_b (Table 4, Section 6.2.3), material obtained in Synthesis 6_3_b was used. The obtained isotherm (Figure B56, Appendix B) shows that the pore volume was 4.5 mL/g, which is three times higher compared to the value obtained when water was used to fill the pores. This large difference might be originating from the drying procedure used. The material measured with mercury intrusion was dried at high temperature under vacuum, whereas before the measurement with water, the alumina was simply dried in an oven at 120 °C. Furthermore, since in the measurement with water only 10 mg of alumina was used, the error in this measurement is large. Therefore, the mercury intrusion measurement for the determination of the pore volume is more accurate. The measured surface area using mercury intrusion was 36 m^2/g, which is about two times the theoretical value and the value measured using N_2-physisorption. No explanation for this large difference could be found.

The pore size distribution versus the incremental surface area is shown in Figure 27. Although the mercury intrusion measurement was intended to obtain a pore size, neither the intrusion data, nor the extrusion data could be used to obtain the pore size. Instead, the size of the windows was obtained. During a mercury intrusion measurement, pressure is needed to fill the pores with mercury. In materials containing spherical pores, the windows are bottle necks during the measurement, and the actual pore diameter has no influence on the pressure needed to fill the pores [37]. The pores are filled after the pressure is high enough to fill pores with a certain window size, as is shown in Figure B57 (Appendix B). In this figure, a schematic representation of the pore filling process is shown. As a consequence of the spherical pores, all surface area measured at the pressure needed to intrude the mercury trough the windows, is subscribed to the size of the windows, instead of to the size of the pores [37].

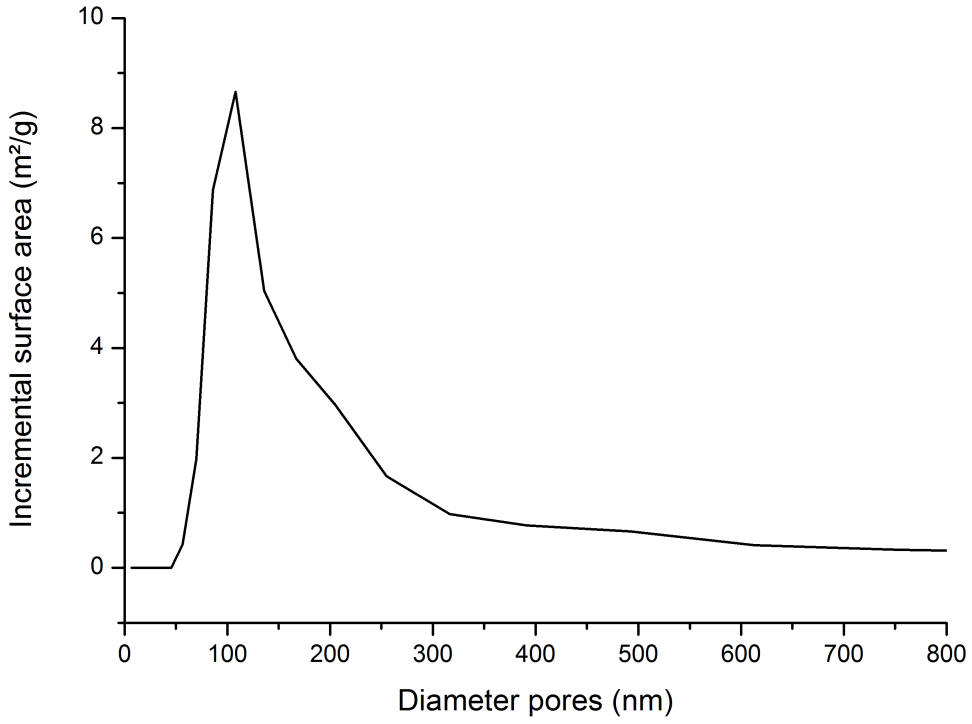

Figure 27: Pore size distribution correlated to incremental surface area, obtained during the intrusion of mercury in the pores.

As shown in Figure 27, a window size of 110 nm was measured, which is about the same size as was obtained using SEM. Since the mercury stays inside the pores during extrusion as an effect of the spherical pore structure (Figure B57f), extrusion data cannot be used for the determination of the pore size [37]. However, the large amount of mercury left inside the pores after all pressure was released indicates that the pores present mainly consist of ink-bottle-like pores.

6.3.3 Calcination temperature and atmosphere

As described in Section 2.3, the calcination temperature determines which structure of alumina is obtained. To see which phase transitions occur during the synthesis of macroporous α-alumina, materials prepared in three different ways were calcined at various temperatures under air and/or nitrogen flow. The obtained materials were measured with XRD. In Figure 28, XRD diffractograms of aluminum hydroxide prepared without the PMMA colloidal crystals as template, dried at 60 °C and calcined for 30 min at 200 °C, 400 °C, 600 °C, 800 °C, 1000 °C or 1150 °C (30 min and 3 hours) are shown.

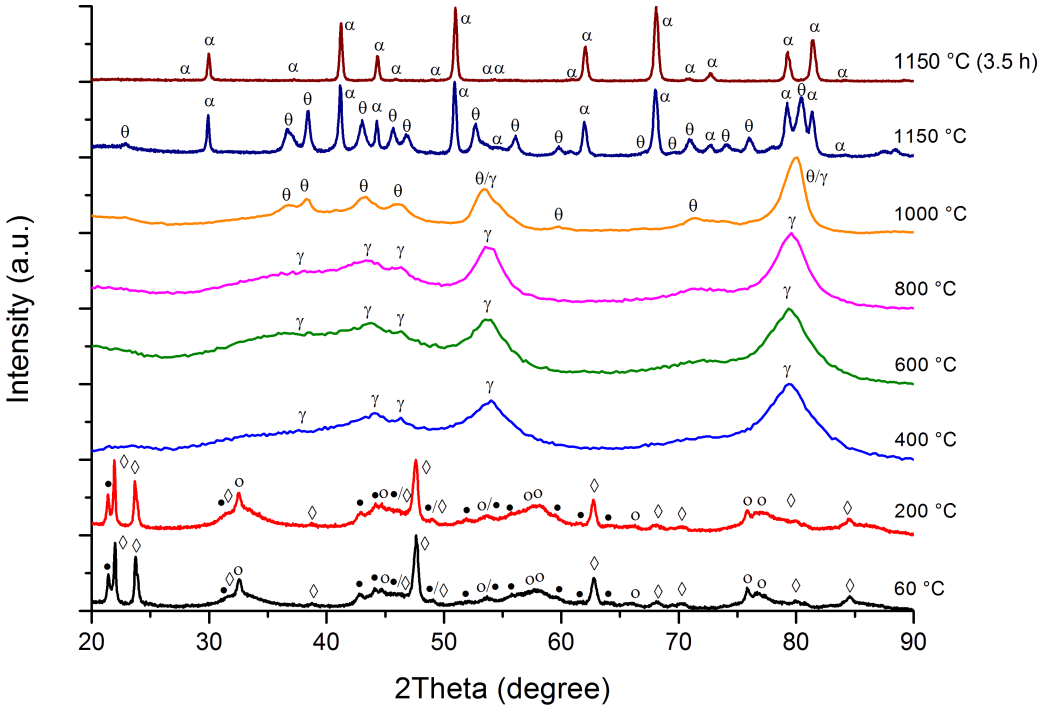

Figure 28: XRD diffractograms of aluminum hydroxide dried at 60 °C and after calcination for 30 min at 200 °C, 400 °C, 600 °C, 800 °C, 1000 °C or 1150 °C (30 min and 3 hours) under nitrogen flow. The diffractograms of the material calcined at 60 °C and 200 °C show peaks of aluminum hydroxide (● = gibbsite, ○ = boehmite and ◊ = bayerite). The diffractograms of the materials heated at 400 °C and higher contain peaks originating from γ-, θ- and/or α-alumina.

In the XRD diffractograms of the material dried at 60 °C and the material calcined at 200 °C, three different structures of aluminum hydroxide are visible: gibbsite, boehmite and bayerite. When the material was calcined at 400 °C, γ-alumina was formed, and

at 1000 °C, a part of the sample transferred into θ-alumina. At 1150 °C, this was slowly transformed into α-alumina. After 3.5 hours, this transformation was complete and the only structure observed is α-alumina. All these structure transformations are comparable to the ones described in literature (Figure 4, Section 2.3).

When impregnated colloidal crystals were calcined, some of the alumina transformations were delayed in temperature, as is shown in Figure 29. The impregnated PMMA colloidal crystals were heated at 200 °C, 400 °C, 600 °C, 800 °C, 1000 °C or 1150 °C for 6 hours, under air flow. The XRD diffractograms of the impregnated PMMA colloidal crystals at room temperature and after calcination at 200 °C show the structure of PMMA [38]. After the impregnated PMMA colloidal crystals were heated above their decomposition temperature (250 °C, Section 5.3.2), peaks attributed to PMMA disappeared and an amorphous alumina structure was obtained (400 °C and 600 °C). Calcination at 800 °C was needed to transform the alumina structure into γ-alumina. This is much higher compared to the temperature needed when alumina was formed without PMMA colloidal crystals present (400 °C, Figure 28).

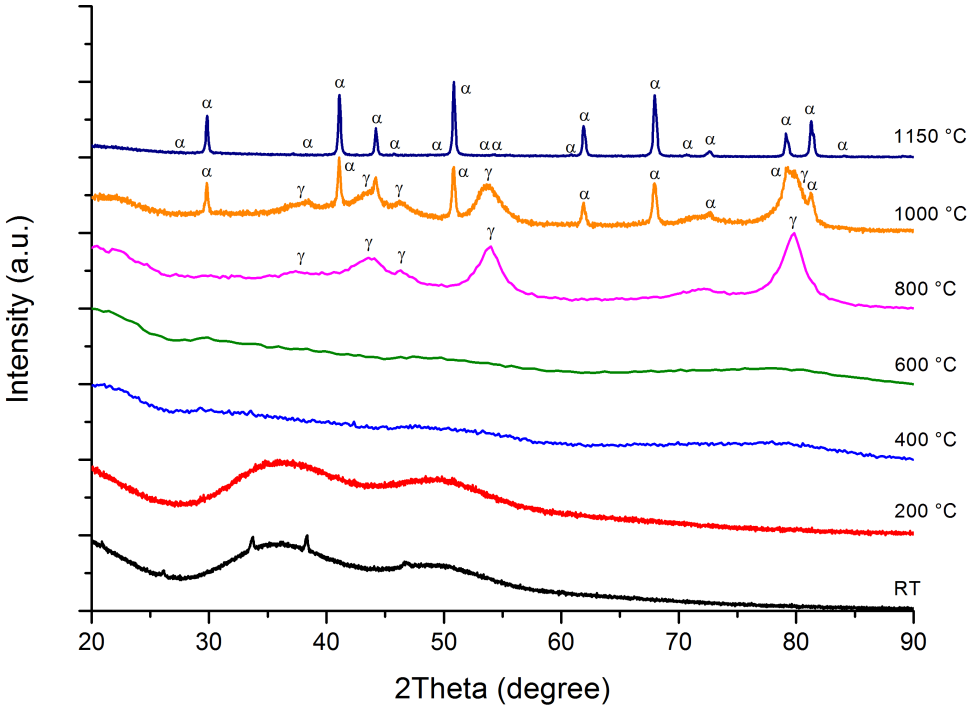

Figure 29: XRD diffractograms of impregnated PMMA colloidal crystals with aluminum hydroxide at room temperature and after calcination for 6 hours at 200 °C, 400 °C, 600 °C, 800 °C, 1000 °C or 1150 °C under air flow. The diffractograms of the material at room temperature and calcined at 200 °C show peaks of PMMA. The sharp peaks visible in the diffractograms of the material at room temperature could not be identified, but could be originating from aluminum hydroxide. The diffractograms of the materials heated at 800 °C and higher contain peaks originating from γ- and/or α-alumina.

Although decomposition of PMMA starts at 250 °C, the color of the sample after calcination at 200 °C, 400 °C and 600 °C was not white, as is shown in Figure 30. Based on TGA measurements performed on the PMMA crystals (Figure 15, Section 5.3.2), complete decomposition was expected at 400 degrees. However, the coloring

shows clearly that this was not the case. This delay in decomposition could be a result of mass transfer limitations. The sample turned white again during the calcination at 800 °C, indicating complete removal of the template material.

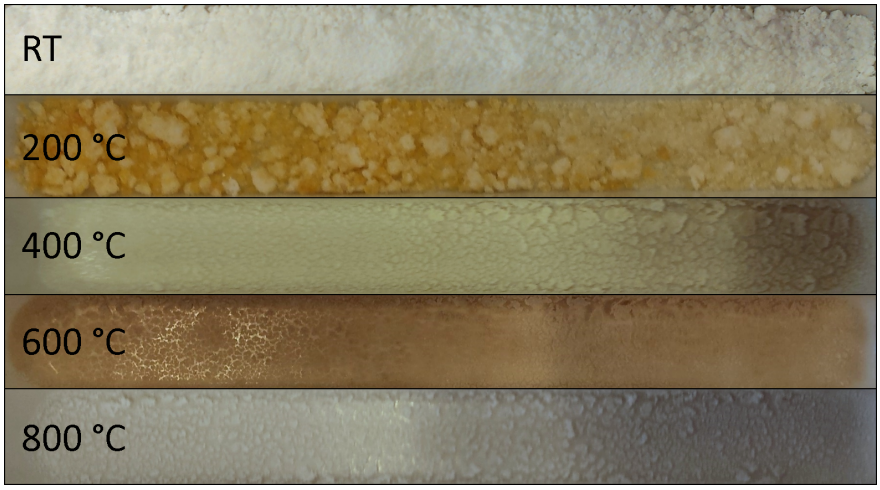

Figure 30: Pictures of the impregnated PMMA colloidal crystals with aluminum hydroxide at room temperature and after calcination for 6 hours at 200 °C, 400 °C, 600 °C or 800 °C. The sample at room temperature is white, just as the sample calcined at 800 °C. In between, the color of the samples is yellow or brown.

The structure of the material at room temperature and calcined at 200 °C, 400 °C or 600 °C were visualized using SEM (Figure 31). The ordering of the PMMA spheres was clearly visible in the impregnated PMMA colloidal crystals at room temperature, but during the calcination at 200 °C, large particles of about 150 µm - 300 µm were formed, presumably as a result of aggregation of PMMA colloidal crystals. The surface of these aggregates lost their structure completely, which was probably caused by melting of the PMMA spheres on the outside of the aggregates (the melting point of PMMA is 130 °C, Section 5.3.2). However, most of the PMMA spheres on the inside of the crystals were apparently still intact, since the materials calcined at 400 °C or higher contained macropores. The PMMA spheres on the inside of the aggregates were most likely stabilized by the aluminum hydroxide present in the voids of the colloidal crystals. On the outside of the colloidal crystals, the PMMA spheres were easier deformed, since no or less aluminum hydroxide was present.

After calcination at 1000 °C, some α-alumina peaks appeared, and after calcination at 1150 °C, only α-alumina peaks were present (Figure 29). In contradiction with the transformation into γ-alumina, the transformation into α-alumina was not delayed. This was expected, considering the complete removal of the template material at 800 °C. A temperature of 1000 °C was high enough to partly transformation γ-alumina into α-alumina, since the material was calcined for 6 hours each time. α-alumina peaks were not observed in the diffractogram of pure aluminum hydroxide calcined at 1000 °C (Figure 28), since this sample was calcined for 30 min instead of 6 hours.

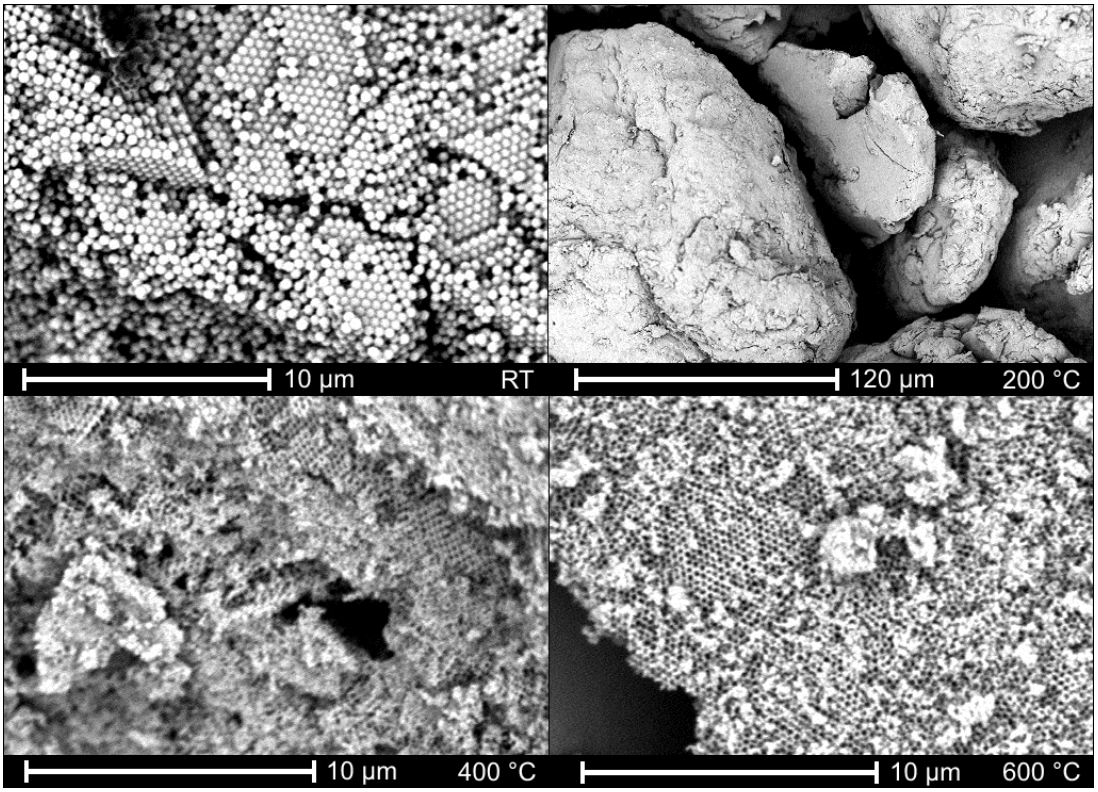

Figure 31: SEM pictures of the impregnated PMMA colloidal crystals with aluminum hydroxide at room temperature and after calcination for 6 hours at 200 °C, 400 °C or 600 °C. These SEM pictures were obtained using the FEI Phenom.

The impregnated PMMA colloidal crystals containing aluminum hydroxide were calcined under nitrogen flow, at 200 °C, 400 °C, 600 °C, 800 °C, 1000 °C or 1150 °C for 6 hours. The XRD diffractograms of the materials obtained are shown in Figure 32. Up to 600 °C, the diffractograms of these materials look the same as the materials calcined under air flow (Figure 29). However, the transition into γ-alumina was even further postponed, since γ-alumina was formed at 1000 °C instead of 800 °C.

Furthermore, the transition into α-alumina was postponed as well, since α-alumina is not formed at all under nitrogen flow, even not at 1150 °C (which was expected from literature, Figure 4 in Section 2.3). This delay is caused by the thin layer of carbon formed as result of the pyrolysis of the PMMA spheres. A second calcination at 1150 °C under air flow was needed to burn this carbon layer off and to transform the alumina into α-alumina (Figure 19).

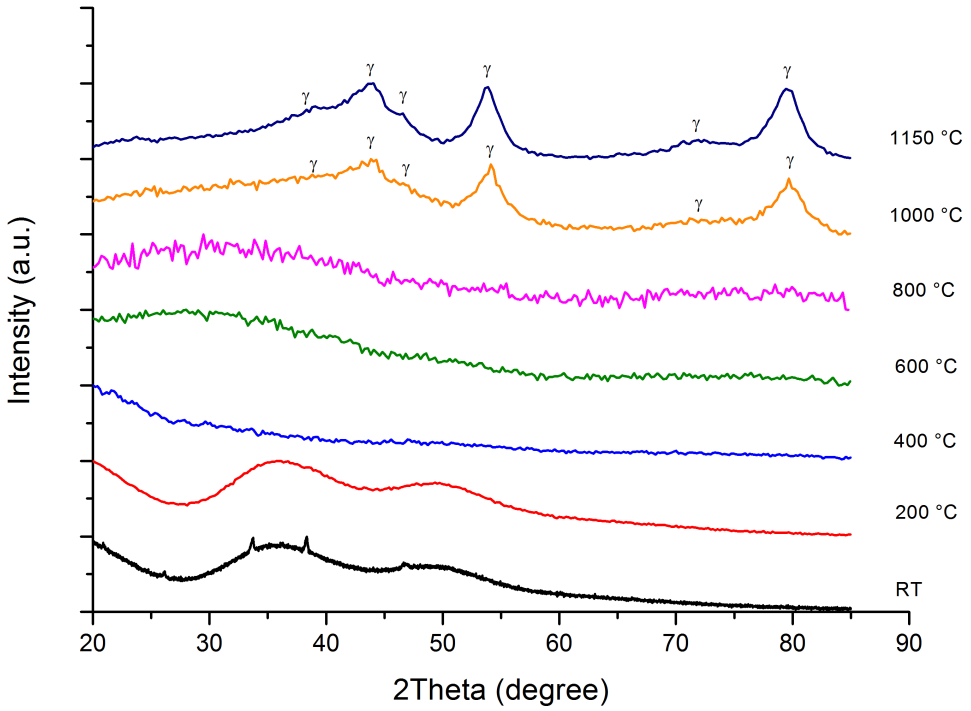

Figure 32: XRD diffractograms of PMMA colloidal crystals containing aluminum hydroxide at room temperature (same diffractogram as shown in Figure 29) and after calcination for 6 hours at 200 °C, 400 °C, 600 °C, 800 °C, 1000 °C or 1150 °C under nitrogen flow. The diffractograms of the material at room temperature and calcined at 200 °C show peaks of PMMA. The sharp peaks visible in the diffractograms of the material at room temperature could not be identified, but could be originating from aluminum hydroxide. The diffractograms of the materials heated at 1000 °C and 1150 °C contain peaks originating from γ-alumina.

6.3.4 Synthesis of ordered macroporous γ-alumina

To determine at which temperature the carbon template decomposes, a TGA-MS measurement was performed on the material obtained after calcination at 1150 °C under nitrogen flow (blue line in Figure 32. The results of these measurements are shown in Figure 33. The TGA measurement shows that the sample decreased in weight around 580 °C (black line). The waste products were detected with MS, and at the m/z of 44 (assigned to CO_2), a large peak was observed at the same temperature (blue line), indicating a carbon decomposition temperature of around 580 °C.

To check the obtained decomposition temperature, the material was calcined for 6 hours at 600 °C. However, the color of the calcined material was still black, and therefore still contained carbon. The calcination temperature was increased to see at which temperature the carbon would burn off, but after calcination at 700 °C and 800 °C for 6 hours, carbon was still present. Finally, after the material was calcined at 900 °C for 6 hours under air flow, the carbon was burned off and the material lost its black color.

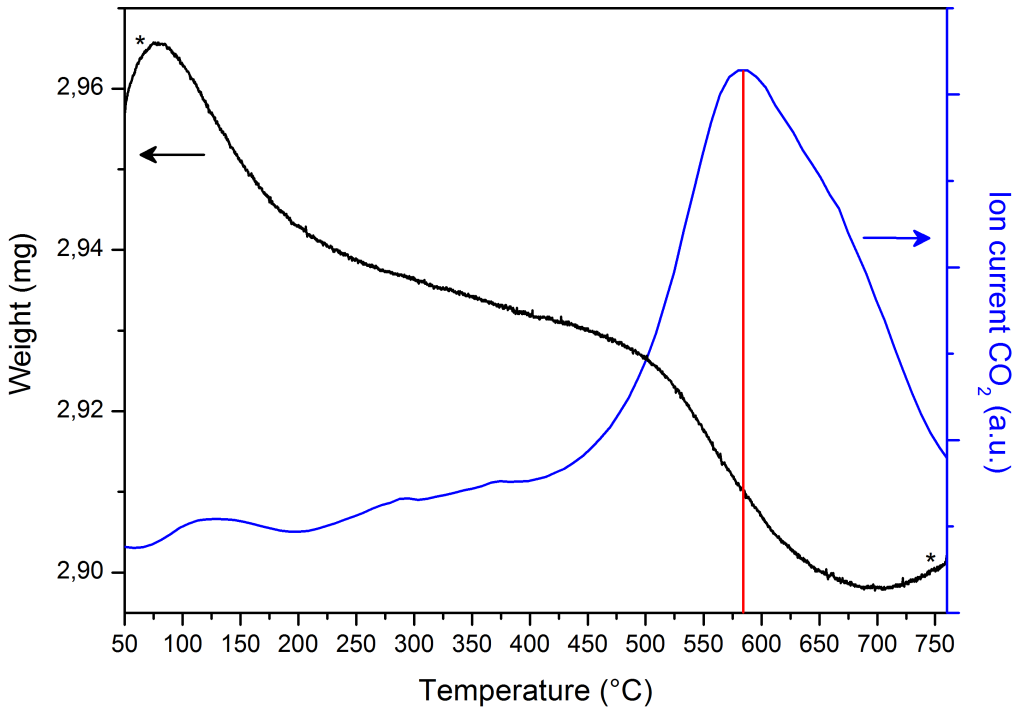

Figure 33: TGA-MS measurement of γ-alumina covered with carbon under air flow, heating ramp: 10 °C/min. The black line is the TGA measurement and the blue line is the MS measurement, in which the m/z of 44 (assigned to CO_2) is shown. Around 580 °C, a decrease in mass is observed in TGA, which corresponds to the detection of CO_2 with the MS, caused by burning off the carbon template. The peaks assigned with ⋆ are buoyancy effects caused by the low amount of sample measured.

XRD was used to determine the structure of the obtained alumina. The XRD diffractogram of the alumina obtained after the calcination at 900 °C is the red line shown in Figure 34, whereas the blue line is the diffractogram of the material after the first calcination at 1150 °C under nitrogen flow. The structure of both materials was γ-alumina. No structure transformation occurred during the calcinations under air flow, which is as was expected from literature (Figure 4, Section 2.3).

Therefore, by decreasing the calcination temperature of the second calcination under air flow to 900 °C, carbon free γ-alumina was obtained. The pore structure of this material is shown in Figure 35. Since the carbon was present during the transformation into γ-alumina and no structure transformations took place after the carbon was removed, the pore structure was preserved remarkably well. The peak assigned by ∗ is an artifact, which was observed in some measurements, and is observed in Figure B58 (Appendix B) as well.

By using N_2-physisorption and mercury intrusion, the surface area of this carbon free γ-alumina was determined. In contrast to the obtained α-alumina materials, this material contained both macropores and mesopores. The mesopores, present in the walls of the macropores, increased the surface area significantly, to 80 m^2/g (mercury intrusion) - 90 m^2/g (N_2-physisorption). The macropores of this γ-alumina were approximately the same size as the macropores present in the obtained α-alumina.

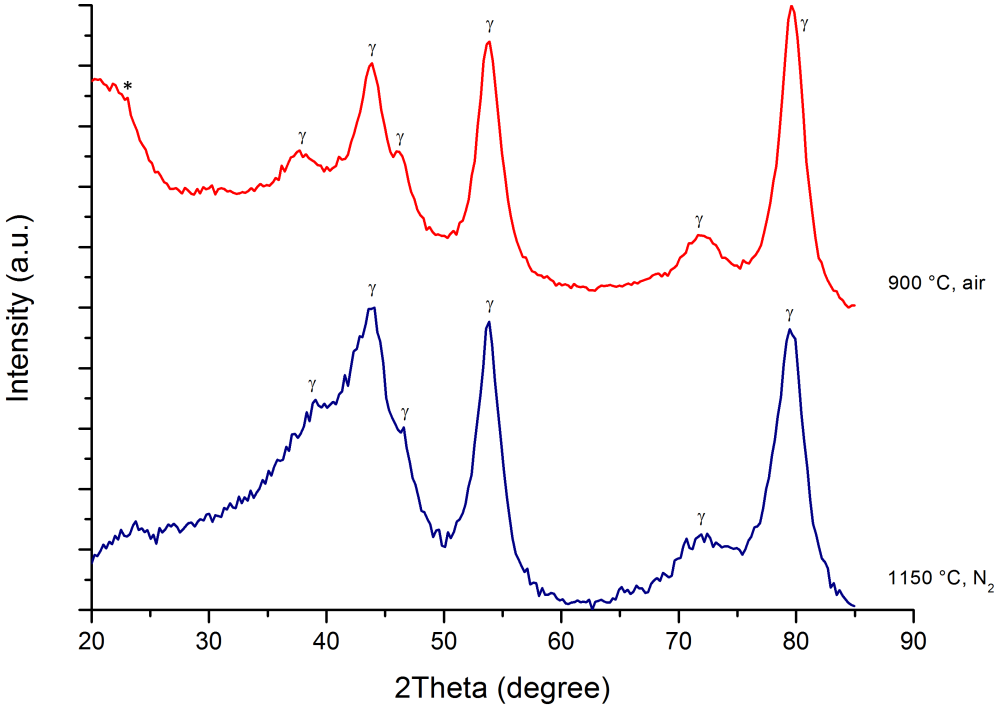

Figure 34: XRD diffractograms of alumina calcined under nitrogen flow at 1150 °C (blue line) and after this material was calcined for 6 hours at 600, 700, 800 and 900 °C under air flow. The structure of both materials is γ-alumina. The peak assigned by ∗ is an artifact of the XRD measurement.

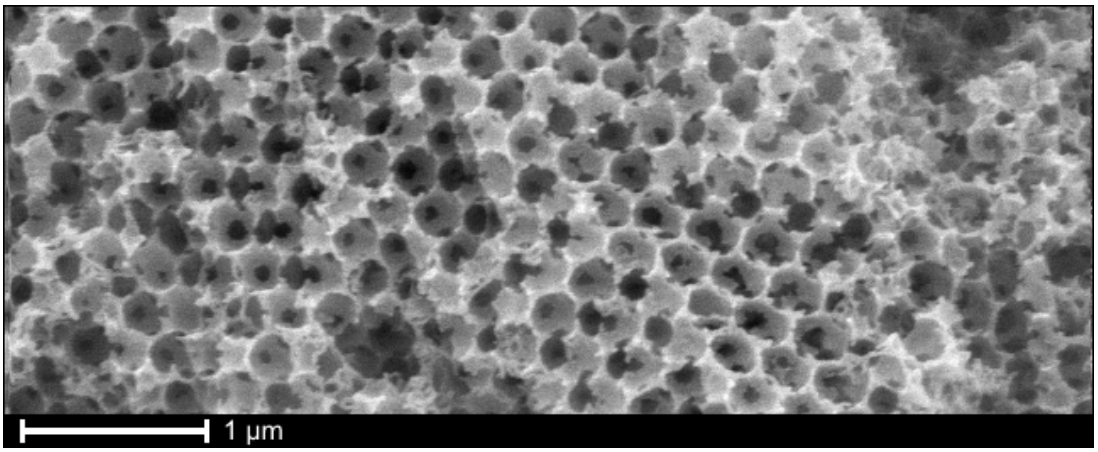

Figure 35: SEM picture of the obtained γ-alumina material after the final calcination at 900 °C under air flow.

6.3.5 Influence calcination step under inert atmosphere

As already noted in the introduction, the size of the used PMMA spheres correlates with the preservation of the cage structure as a result of the varying thickness of the walls. In this research, PMMA spheres of 416 ± 17 nm were used, which were even smaller in size compared to the smallest PMMA spheres used by Sokolov *et al.* [16]. By using the same synthesis procedure (Synthesis 1.5_1_a, Table 4, Section

4), alumina material was obtained which contained both regions in which the cage structure was preserved and regions in which the cage structure was (partially) lost. In this synthesis, the PMMA template was completely burned off before γ-alumina was formed and therefore the template could not offer support during the phase transitions of amorphous alumina into γ-alumina and eventually into α-alumina.

By calcining the impregnated crystals first under nitrogen atmosphere, pyrolysis of the PMMA colloidal crystals took place, which resulted in the formation of a small layer of carbon. Although this carbon template delayed the structure transformations of the alumina material (Figure 32), it stabilized the cage structure during this transformation. Almost no loss of cage structure was observed in the obtained carbon covered γ-alumina materials.

The structure transformation of γ-alumina into α-alumina was delayed simultaneously as a result of the carbon template (Figure 32). Unfortunately, no oven was available to heat the sample above 1150 °C under inert atmosphere, and therefore, no carbon covered α-alumina was obtained. Instead, to obtain α-alumina, first the carbon template needed to be removed in a second calcination under air flow. At 900 °C, the carbon template burned off (Section 6.3.4) whereupon α-alumina was formed after the temperature was increased to 1150 °C.

Since the template was already removed before the transformation of γ-alumina into α-alumina, no template was present to stabilize the cage structure. Although no substantial cage deformations were observed, the thickness of the alumina walls increased and the overall pore size decreased during this phase transformation. Compared to α-alumina obtained by calcination in air flow only, in total, less loss of cage structure was observed. By using SEM and UV-VIS spectroscopy, the quality of the cage structure and the ordering of the pores of α-alumina material prepared using one and two calcination steps were compared. These comparisons demonstrate the positive influence of the extra calcination step.

In Figure 36, the cage structure of the alumina prepared in Synthesis 1.5_4_a (Table 4, Section 6.2.3, one calcination step), shown in A and C, is compared to the pore structure of material prepared in Synthesis 1.5_3_b (Table 4, two calcination steps), shown in B and D. Both materials contained parts of very thin alumina walls (A, B) and parts of somewhat thicker alumina walls (C, D). Although the difference in the cage structure is not obvious, the cage structure was slightly better preserved in the material prepared in Synthesis 1.5_3_b (B, D). In A, walls between some cages were missing, creating sheetlike pores (indicated with the red oval shapes) instead of the separated cages shown in B. In C, the connection points of the walls in between the cages were even thicker compared to these points shown in D.

This comparison is not completely fair, since in Synthesis 1.5_4_a, PMMA colloidal crystals were impregnated four times (instead of three times) with both impregnation solutions. As noted in Section 6.3.1, the quality of the cage structure seems to improve by increasing the amount of impregnation steps. Of all syntheses performed in which the impregnated colloidal crystals are calcined under airflow only, this material showed the best preserved cage structure. In Figure 37, two SEM pictures of material obtained in Synthesis 6_3_a (Table 4) are shown, in which the PMMA colloidal crystals were impregnated three times and only calcination under air flow was applied. In Figure 37B, again walls between some cages are missing, which generated sheetlike pores. The

difference in the quality of the cage structure between this material and the material obtained in Synthesis 1.5_3_b (Figure 36B and D) is more pronounced.

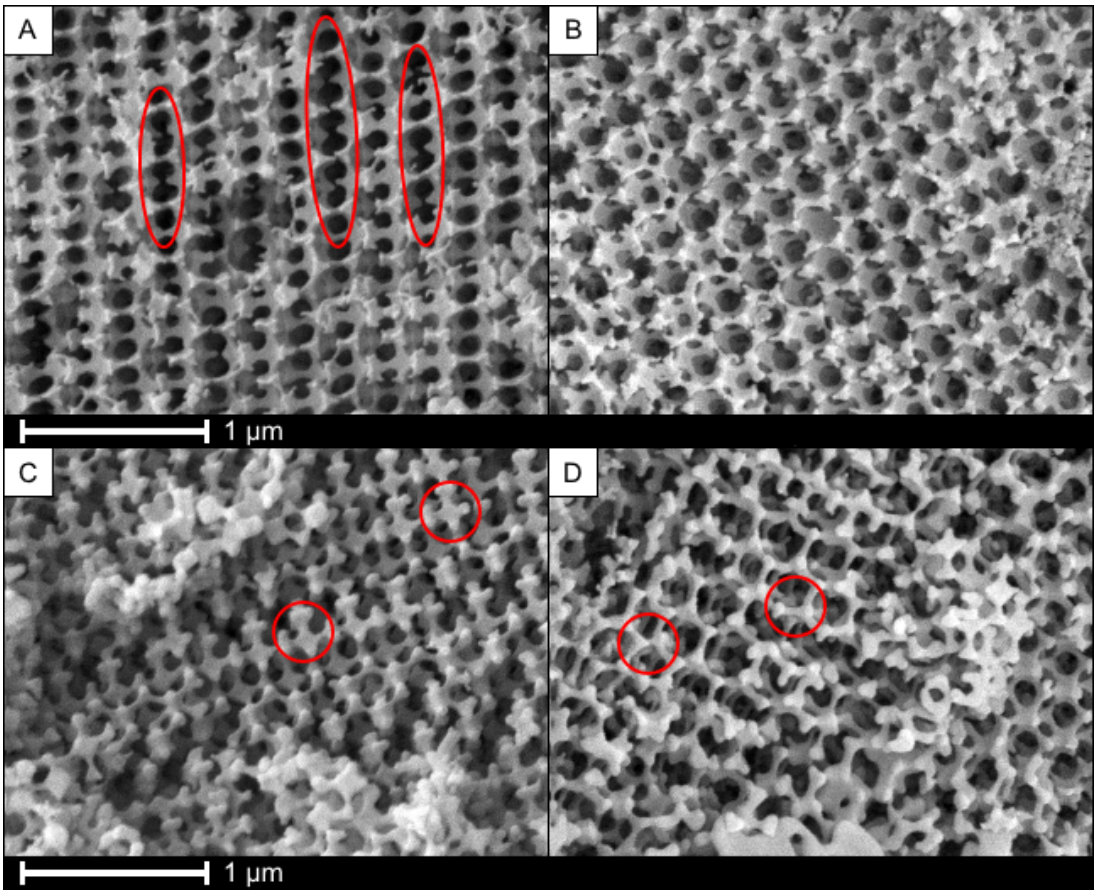

Figure 36: SEM pictures of macroporous α-alumina obtained by calcining impregnated PMMA colloidal crystals under air flow only (Synthesis 1.5_4_a) (A, C) and by applying a calcination under nitrogen flow prior to the calcination under air flow (Synthesis 1.5_3_b) (B, D). Although both samples contained parts with thinner pore walls (A, B) and thicker pore walls (C, D), the cage structure was better preserved in Synthesis 1.5_3_b.

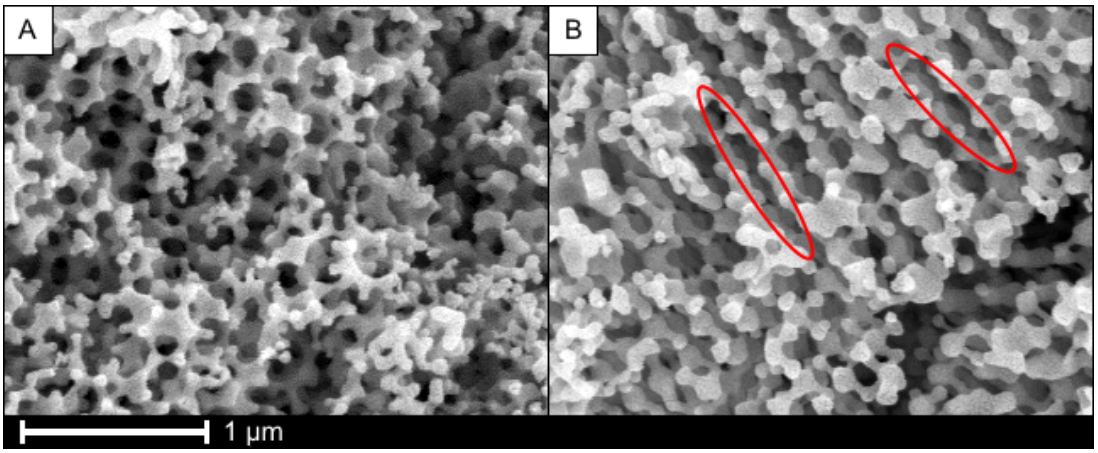

Figure 37: SEM pictures of macroporous α-alumina synthesized by calcining impregnated PMMA colloidal crystals under air flow only (Synthesis 6_3_a).

The quality of the cage structure of different macroporous alumina materials can be compared using UV-VIS, as a result of the correlation between the intensity of the reflection peak and the ordering and quality of the cage structure of the alumina. Since the α-alumina prepared in Synthesis 6_3_a was used for other purposes, no material was left for UV-VIS measurements. Therefore, in Figure 38, UV-VIS spectra of material obtained in Synthesis 1.5_4_a (green line) was compared to spectra of material obtained in Synthesis 1.5_3_b (black line). Although in both spectra a reflection peak was observed, the reflection peak in the spectrum of the alumina obtained in Synthesis 1.5_4_a was significantly less pronounced compared to the reflection peak in the spectra of the material obtained in Synthesis 1.5_3_b. This indicates that the cage structure of the material obtained in Synthesis 1.5_3_b was better preserved compared to the cage structure of the material obtained in Synthesis 1.5_4_a and demonstrates the positive influence of the extra calcination step under nitrogen flow prior to the calcination under air flow.

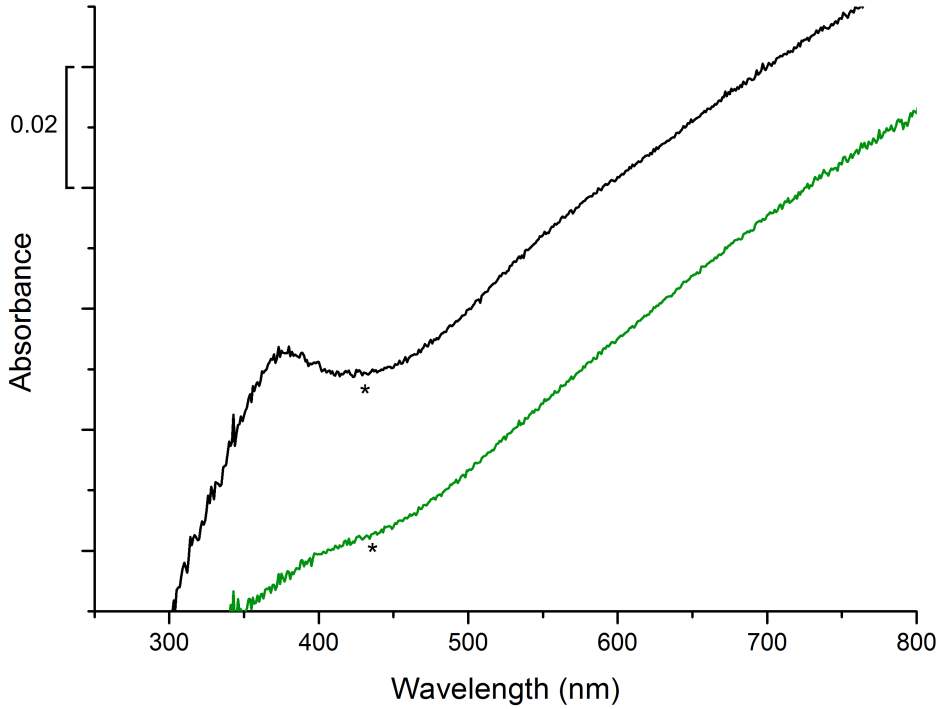

Figure 38: UV-VIS spectra of material calcined under air flow (Synthesis 1.5_4_a) (green line) and of material calcined under nitrogen flow prior to calcination under air flow (Synthesis 1.5_3_b) (black line). In both spectra, a peak around 430 nm was observed (indicated with ⋆), although the intensity of the reflection peak is significantly different, indicating a better preserved cage structure present in the material obtained in Synthesis 1.5_3_b compared to Synthesis 1.5_4_a. Starting at 300 nm, a steep increase in the black spectrum is visible. This may be a peak caused by the second order Bragg's diffractions, but could also be an artifact caused by using non-porous α-alumina as background. For these measurements, an integrating sphere was used to collect all reflections.

6.3.6 Pretreatment PMMA colloidal crystals

Generally, the PMMA colloidal crystals were dried for several days at room temperature before impregnation (Section 5.2.3). However, as shown in the DSC curve of the PMMA colloidal crystals (Figure 14, Section 5.3.2), the crystals still contained MMA and water. To see whether drying the PMMA colloidal crystals at elevated temperatures had an influence on the obtained alumina, the PMMA colloidal crystals were dried at 60 °C and 120 °C. In Figure 39, SEM pictures of alumina samples prepared with these PMMA colloidal crystals are shown.

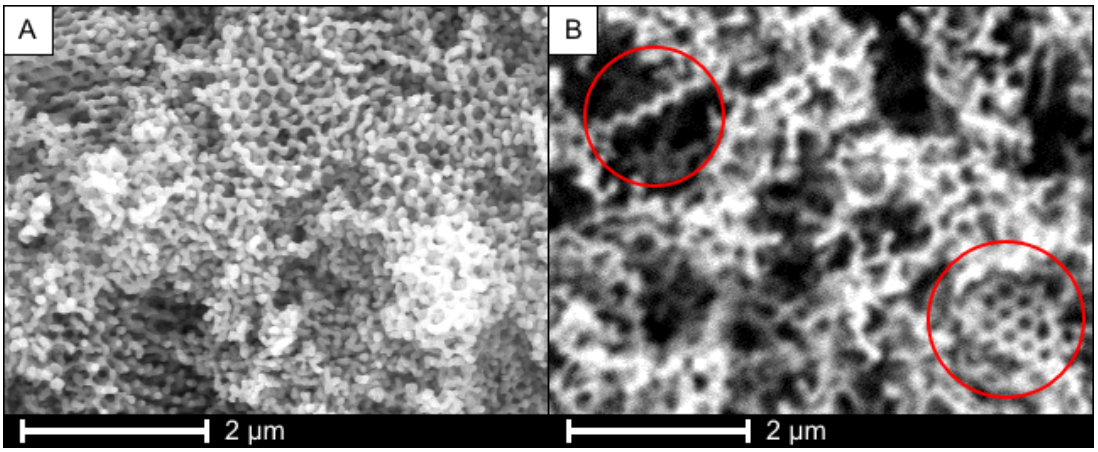

Figure 39: SEM pictures of macroporous α-alumina synthesized using PMMA dried at 60 °C (A) and 120 °C (B). The SEM picture in (B) was obtained using the FEI Phenom.

The alumina displayed in Figure 39A (synthesized by using PMMA colloidal crystals dried at 60 °C) is comparable to the material obtained when PMMA colloidal crystals were dried at room temperature (Figure 37). Therefore, we conclude that drying the material at 60 °C has no significant influence on the pore structure of the material. On the other hand, it does have a positive influence on the yield, since using 1.5 g dried PMMA colloidal crystals provided 37 mg of α-alumina, instead of 20 - 30 mg. This is explained by the removal of the MMA and water in the voids. More precursor solution was able to penetrate the pores, since more empty space was available.

Increasing the drying temperature to 120 °C has a negative influence on the obtained alumina. The alumina displayed in Figure 39 B (synthesized by using PMMA colloidal crystals dried at 120 °C) consisted mostly out of strings and sheets, as indicated in the red circles. There could be multiple reasons for this. One explanation is that the surface groups of the PMMA were changed, which had an influence in the wetting degree of the precursor. A more solid explanation is that the PMMA spheres were partly merged, since the drying temperature is quite close to the melting point of the PMMA colloidal crystals (Figure 14 Section 5.3.2), which resulted in decreased void sizes. An schematic representation of this effect is shown in Figure 40. As a result of the partly merged PMMA spheres in the colloidal crystal, the windows of the obtained alumina material increased, which decreased the thickness and strength of the walls. As a consequence, the material broke on several places, leading to strings and plates of alumina, instead of three dimensional ordered cage structures.

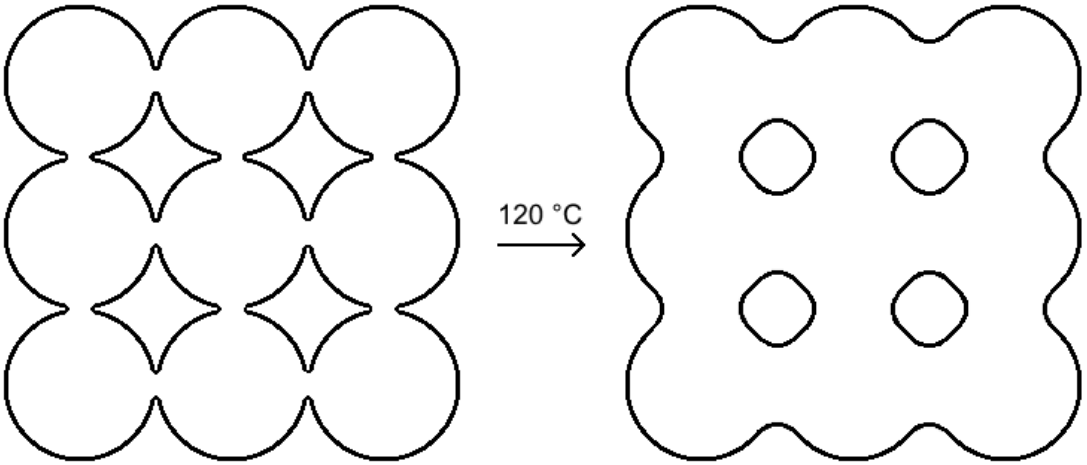

Figure 40: PMMA colloidal crystals before and after drying at 120 °C. Since the melting point of the colloidal crystals is 130 °C, the spheres partly merged.

6.3.7 Calcination in combustion boat versus plug flow reactor

Unregulated and poor drainage of waste products formed during the combustion or pyrolysis of the PMMA and the formation of alumina in a combustion boat may have a negative influence on the pore structure. Therefore, the calcination was performed in a plug flow reactor. In this reactor, the calcination flow goes trough the material instead of over the material as in a combustion boat. Impregnated PMMA colloidal crystals were divided over a combustion boat and a reactor, whereupon both samples were calcined first under inert atmosphere and afterward under oxygen containing atmosphere. The calcination parameters of the calcination in the combustion boat were different from the calcination parameters in the reactor, as described in Sections 6.2.2 and 6.2.6. For both calcinations performed in the reactor, the gas flow was 5 - 10 times lower and the calcination temperatures were slightly lower. Furthermore, the material in the reactor was calcined 3 times as long under air flow compared to the material calcined in the combustion boat. Still, by comparing the obtained materials calcined in a combustion boat and in a reactor, an indication of the influence of this parameter was obtained.

In Figure 41, XRD diffractograms of the material calcined in a combustion boat are compared to material calcined in a plug flow reactor. Most problems with unregulated and poor drainage were expected during the calcination under inert atmosphere, since decomposition of PMMA colloidal crystals took place during this calcination. Furthermore, during this calcination, a large amount of water was formed during the conversion of aluminum hydroxide into alumina as a result of the condensation process.

However, no significant differences were observed in the XRD diffractograms of the materials calcined under inert atmosphere (black and blue line). In both diffractograms, peaks of γ-alumina are visible. The second calcination under oxygen containing atmosphere was expected to make no significant difference, but here differences were clearly visible in the diffractograms (red and green line). Whereas all alumina was converted into α-alumina after calcination in the combustion boat, material calcined in the reactor still consisted partly of γ-alumina, even after calcination for 18 hours. Since

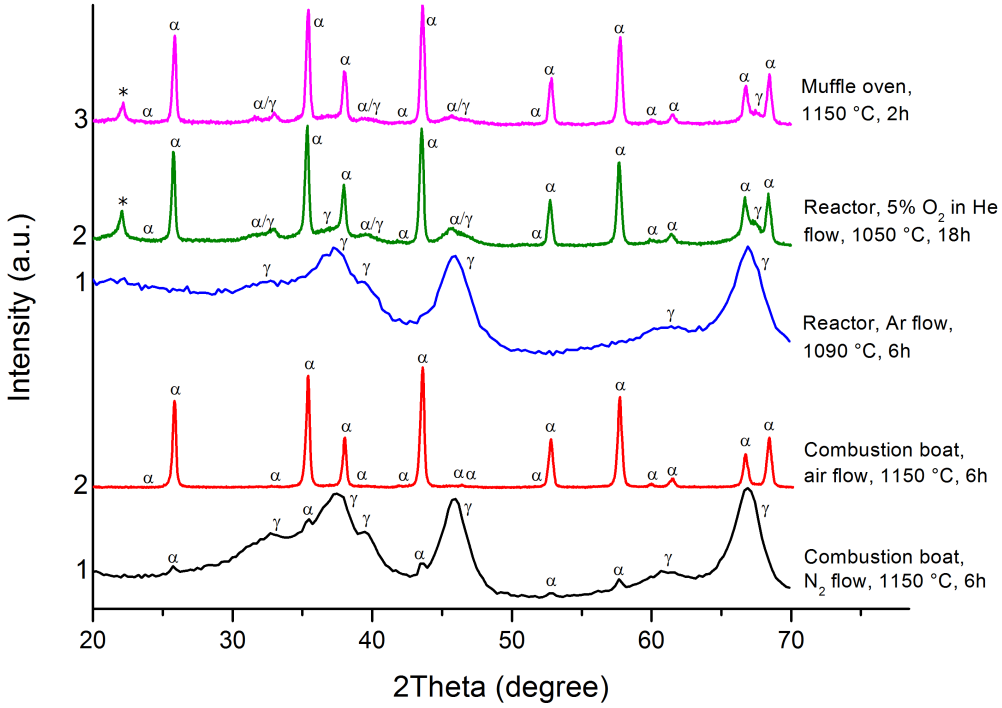

Figure 41: XRD diffractograms of material calcined in a combustion boat (black and red line) and in a plug flow reactor (blue, green and pink line). The alumina obtained after the first calcination in a combustion boat under N_2 flow consists mostly of γ-alumina, which is converted into α-alumina after the second calcination under air flow. During the first calcination in the reactor under argon flow, γ-alumina is formed likewise, but this was not completely converted into α-alumina during the second calcination under a flow of 5 % O_2 in He, which was carried out at 1050 °C for 18 hours. The peak assigned by ∗ could not be identified. The 2Theta value of these peaks is different from all other diffractograms in this report, since these diffractograms were measured using a Cu source instead of a Co source.

we wanted to make a comparison between two α-alumina materials, the material was calcined again in a muffle oven, for 2 hours at 1150 °C. However, the diffractogram of this material (pink line) shows that the material is still partly consisting of γ-alumina.

By using SEM, the cage structure of these materials was compared. In Figure 42, SEM pictures of the materials obtained after the first calcination step under inert atmosphere are shown. In both materials, the cage structure was preserved and no significant differences were observed, suggesting that the different calcination setups have no obvious influence on the obtained alumina material.

In Figure 43, SEM pictures of the material calcined after the second calcination under atmosphere containing oxygen are shown (A, B, C). The pore structure of the material calcined in the plug flow reactor (Figure 43B) might be better preserved compared to the material calcined in the combustion boat (Figure 43A). However, the material shown in Figure 43B consist both of γ- and α-alumina, whereas the material shown in Figure 43A consist only of α-alumina. Although the material calcined a third time (Figure 43D) still partly consisted of γ-alumina, the pore structure of this material is now comparable to the α-alumina obtained by calcination in the combustion boat (Figure 43A).

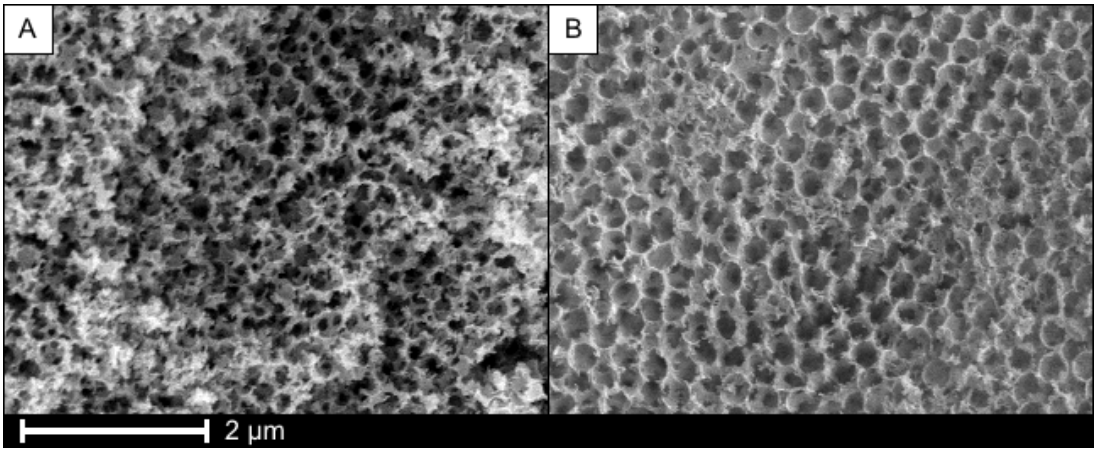

Figure 42: SEM pictures of carbon covered macroporous γ-alumina obtained after calcination under inert atmosphere in a combustion boat at 1150 °C (A) and in a plug flow reactor at 1090 °C (B).

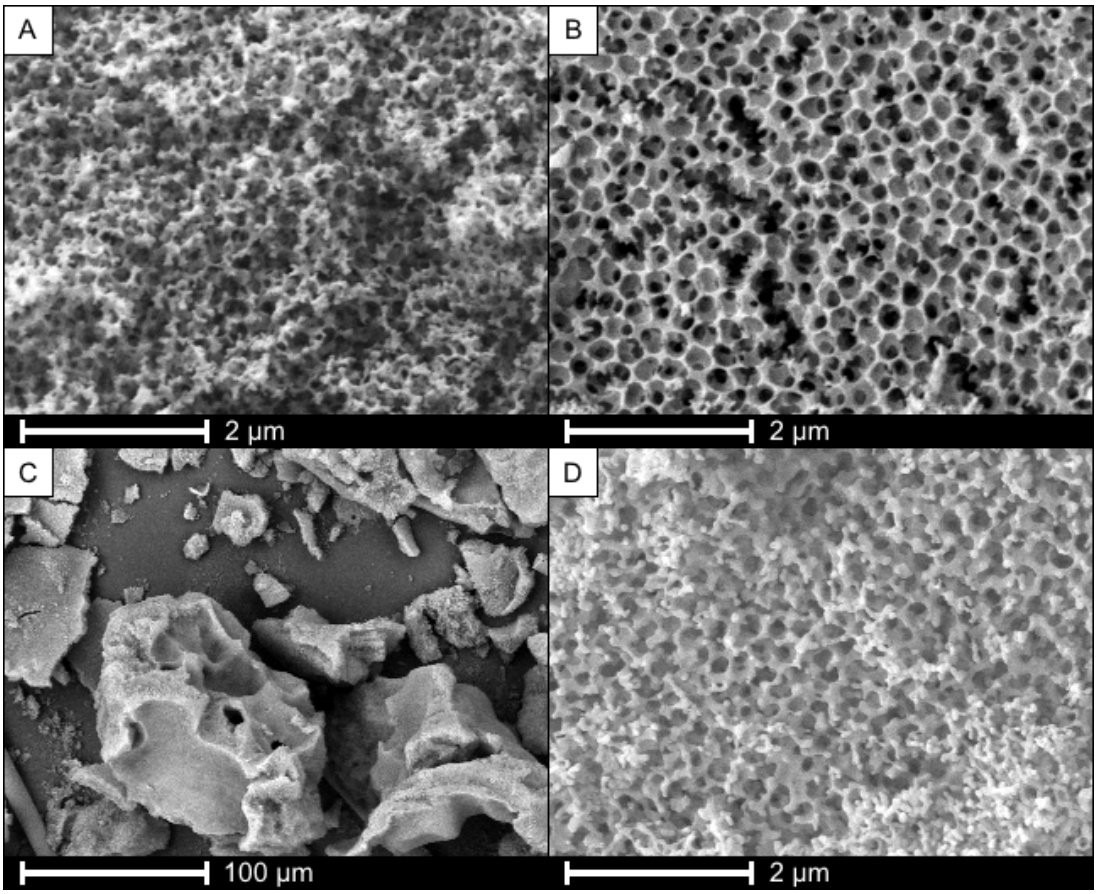

Figure 43: SEM pictures of material shown in Figure 42 calcined a second time under atmosphere containing oxygen in a combustion boat at 1150 °C for 6 hours (A) and in a plug flow reactor at 1050 °C for 18 hours (B, C). This last material was calcined a third time in a muffle oven at 1150 °C for 2 hours (D).

Furthermore, in both the materials calcined in the combustion boat and in the plug flow reactor, large, irregular formed alumina particles were observed (Figure 43C).

These particles were presumably formed during the impregnation, as a result of too short drying times during the impregnation of the PMMA colloidal crystals. Since, as a consequence of this short drying times the cage structure was less preserved, it is hard to compare these materials only using SEM. However, the maximum amount of alumina synthesized by calcining the impregnated PMMA colloidal crystals in the plug flow reactor was not enough to use UV-VIS spectroscopy as bulk technique. Based on the obtained results, no significant differences between the calcination in a combustion boat and calcination in a plug flow reactor were observed, but more characterization is needed to confirm this.

6.3.8 Strength of cage structure macroporous alumina

In order to use ordered macroporous α-alumina as support material for a catalyst, the material should be resistant to attrition. Besides that, the catalysts is usually sieved to a certain sieving fraction, to avoid pressure drops in the reactor. To use as much material for sieving as possible, particles smaller than the preferred size are usually pressed together under several tons of weight. When 3 ton was applied to the macroporous α-alumina, the structure was lost, as is shown in Figure 44B. On the other hand, 1.5 ton was applied to the material shown in Figure 44A, and here, the pore structure is still clearly visible. This demonstrates that the cage structure is strong enough to endure pressures at least up to 1.5 ton for a short amount of time, but that the cage structure is destroyed when a weight of 3 ton is applied.

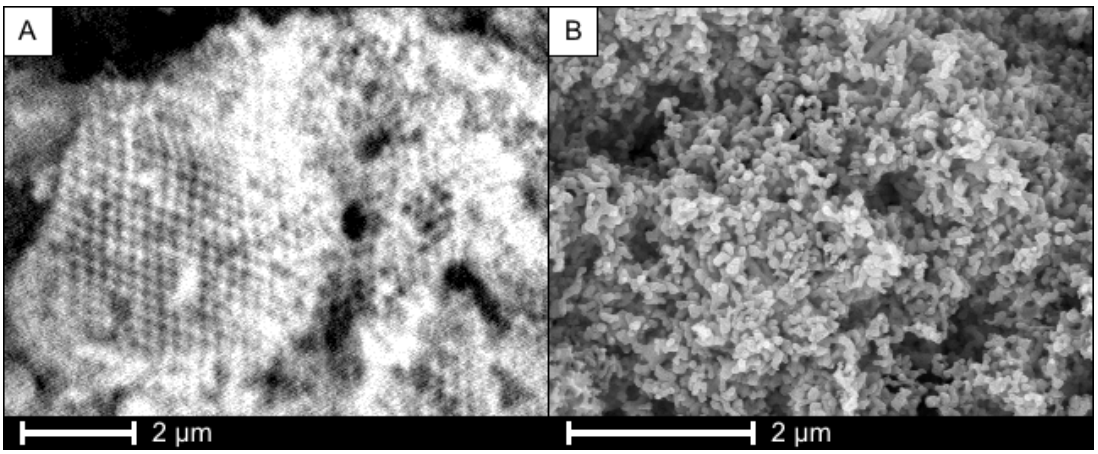

Figure 44: Macroporous α-alumina pressed under 1.5 ton (A) and under 3 ton (B). The SEM picture in (A) was obtained using the FEI Phenom.

7 Part III: Synthesis of catalyst and catalytic testing

In this chapter, support material obtained in Chapter 6 was impregnated with silver, by using incipient wetness impregnation and the synthesized catalyst was tested in the epoxidation of ethylene. First, the impregnation method is explained, whereupon experimental details are given. Finally, the catalyst is characterized and results of the catalytic test are described and discussed.

7.1 Methods

7.1.1 Incipient wetness impregnation

The silver particles are attached on the macroporous α-alumina support by incipient wetness impregnation. Using this method, enough precursor solution is added to the support material to exclusively fill the pores. The pores are filled with precursor solution by capillary force. Therefore, the viscosity of the precursor solution and wetting degree of the precursor/support interface is important, likewise in filling the pores of hard templates (Section 2.4.2). After the pores are filled, the support material is dried in an oven [39]. After drying, the material is calcined, to convert the precursor into a metal oxide. [6, 40]

7.2 Experimental

7.2.1 Chemicals

In Table 6, the used chemicals for the impregnation of the alumina with silver are listed. The chemicals were used as received, no extra purification was applied.

Table 6: Used chemicals, their formula and supplier.

Chemical	Formula	Supplier
Silver nitrate (99+ %)	$AgNO_3$	Sigma-Aldrich
Oxalate dihydrate (99.5 %)	$C_2H_2O_2 \cdot 2\,H_2O$	Merck
Ethylenediamine (*en*) (99+ %)	$C_2H_4(NH_2)_2$	Sigma-Aldrich

7.2.2 Impregnation of α-alumina

Incipient wetness impregnation was used to impregnate the synthesized α-alumina with silver. First the precursor (silver oxalate) was prepared, using a method based on the procedure described by Pourmortazavi *et al.* [41]. Oxalate dihydrate and silver nitrate were both dissolved in water. These solutions were mixed in a 1:2 molar ratio of oxalate dihydrate and silver nitrate, which resulted in immediately precipitation of the silver oxalate. This was collected by centrifugation and washed three times with water. The silver oxalate was dried in an oven at 60 °C and finally stored in a dark bottle to protect the silver oxalate against sunlight.

The aimed loading of the catalyst was 15 wt% silver. This was achieved by dissolving 0.068 g silver oxalate in 0.34 g solvent (ratio: H_2O/en = 0.73 in volume). 0.27 g alumina support (prepared using the same synthesis conditions as in Synthesis 6_3_b, Table 4, Section 6.2.3) was dried in a heating mantle (setting 3-4) under vacuum for 2 hours. Afterward, the vacuum was removed and a syringe was used to add small drops of precursor on top of a stirring bean distributing the precursor in even smaller drops over the support (see Figure 45). This way, the precursor was equally distributed over the support material. After all precursor was added, the support was completely wet, indicating that the volume of the precursor solution was moderately too large. The sample was dried overnight at 60 °C and finally calcined for 2 hours at 250 °C (ramp: 5 °C/min). After the calcination program was finished, the oven was opened to let the sample cool down quickly.

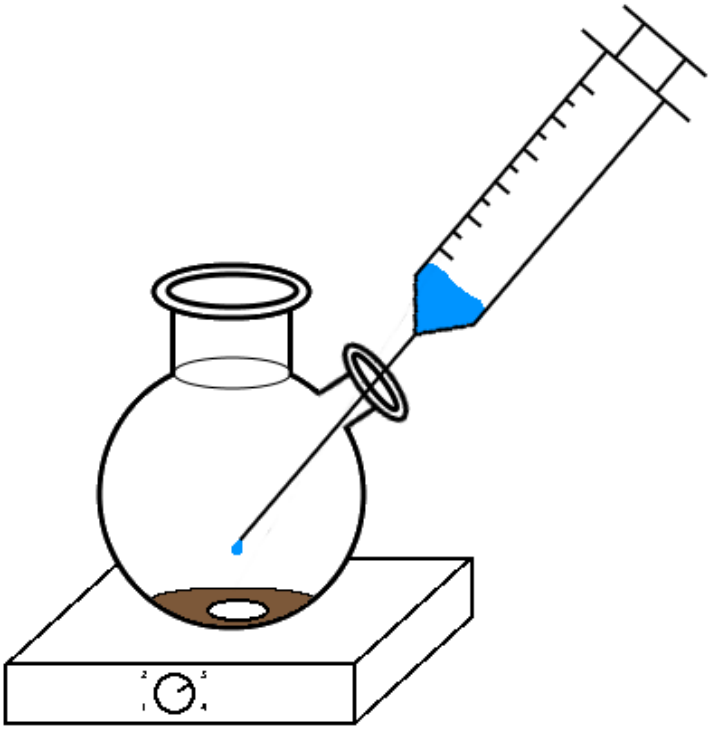

Figure 45: Schematic overview of the incipient wetness impregnation setup.

7.2.3 Characterization

SEM samples were prepared by depositing the catalyst powder on a carbon film sticker attached to the sample stub. The samples received a sputter coating of platinum and palladium with a thickness of 10 nm for better conductivity. For TEM measurements, first the catalyst was grinded into a fine powder, which was dispersed in ethanol by sonication. A droplet of this dispersion was placed on a TEM grid covered with a thin layer of carbon film and afterward, the grid was set aside to let the ethanol evaporate. Other characterization techniques used are XRD and GC.

7.2.4 Catalytic testing in ethylene epoxidation setup

The catalyst was tested in the epoxidation of ethylene, the setup is shown in Figure 46. 150.0 mg catalyst was placed in the reactor between two plugs of glass wool. A down flow of premixed gasses (62% helium, 30% ethylene and 8% oxygen) was connected to the reactor and the reactor was heated using a temperature program from 180 °C up to 260 °C. The reaction products were characterized using gas chromatography.

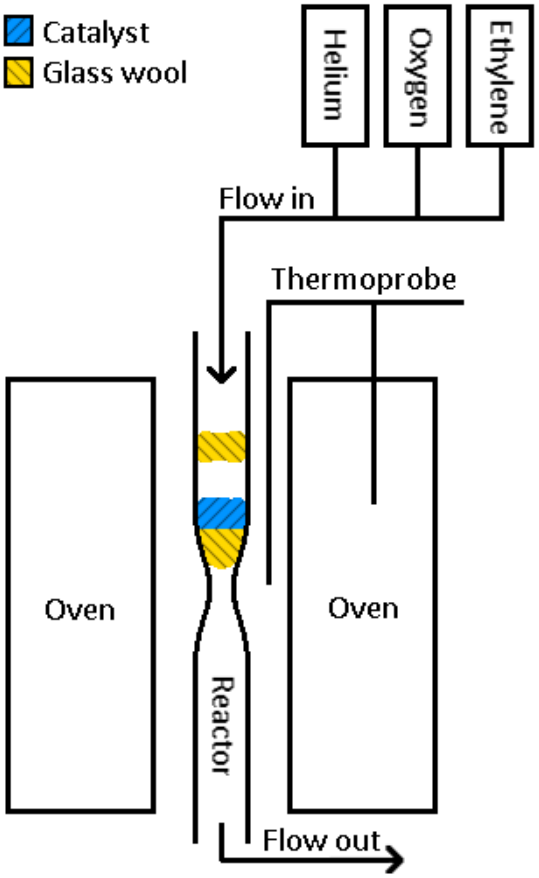

Figure 46: Schematic overview of the ethylene epoxidation setup.

7.3 Results and discussion

7.3.1 Impregnation of α-alumina

TEM and SEM pictures of the catalyst are shown in Figure 47. Only a low amount of silver particles was observed using these techniques. By measuring 30 particles, the estimated size range of the silver particles is 20 to 80 nm. However, this is only an indication of the actual particle size of the silver particles inside the pores, since these silver particles could not be visualized using TEM and SEM.

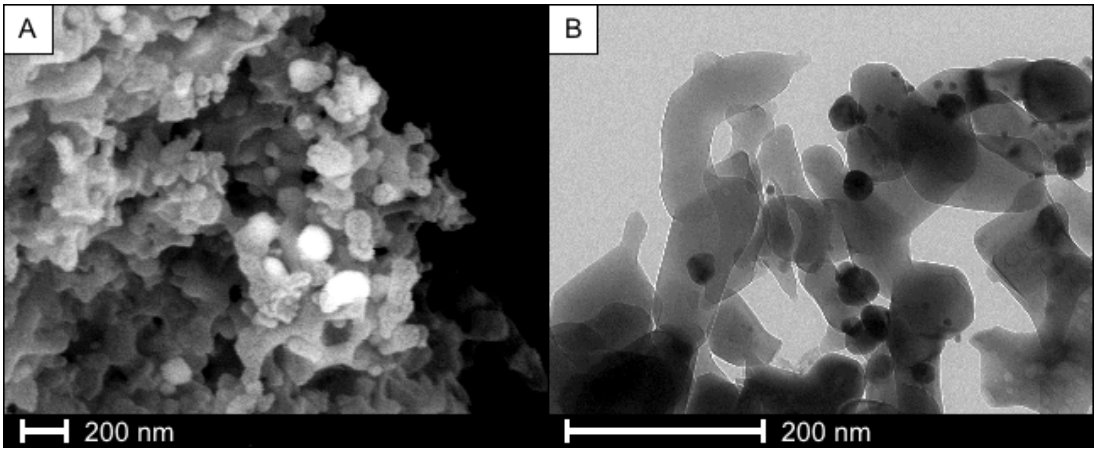

Figure 47: SEM (A) and TEM (B) pictures of the synthesized catalyst. In the SEM picture, the silver is visible as white spherical particles. In the TEM picture, the silver is visible as the darker spherical particles.

In Figure 48, the XRD diffractograms of the support material (black line) and the catalyst (red line) are shown. The peaks originating from the α-alumina are visible in both diffractograms, extra peaks originating from silver are clearly visible in the diffractogram of the catalyst.

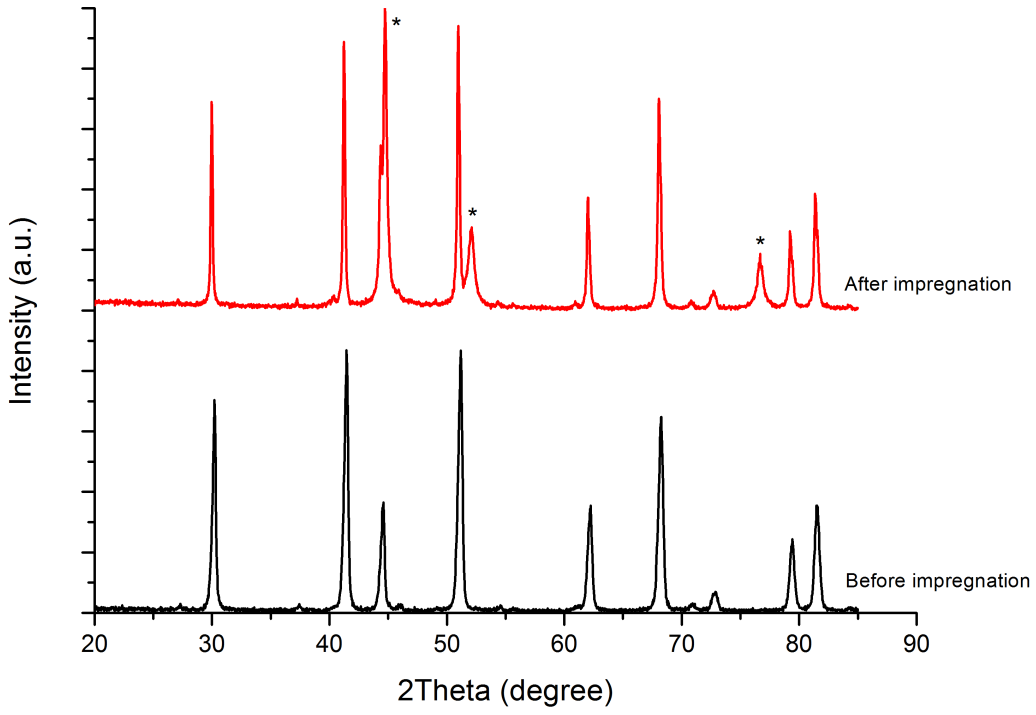

Figure 48: XRD diffractogram of the support material before impregnation (black line) and the catalyst (red line). In the diffractogram of the catalyst, in addition to the peaks originating from α-alumina, peaks originating from silver are visible, assigned by $\star$.

The crystallite size of the silver particles is calculated using the Scherrer equation, from the width of the peaks at half the maximum intensity, and is approximately 32

nm. The peak used for this calculation is the peak at 77 degree. Since silver particles may contain more crystallites, this size is only an indication for the crystallite size and not for the actual particle size.

7.3.2 Catalytic testing in ethylene epoxidation setup

The conversion and selectivity during the epoxidation reaction is dependent on the reaction temperature. This correlation is visible in Figure 49, in which the conversion of ethylene, selectivity towards ethylene oxide and reaction temperature of the epoxidation are shown. In the beginning, activation of the catalyst took place, since the selectivity increased significantly at constant temperature. Therefore, the first 20 hours are not visible in Figure 49. The complete graph is placed in Appendix C, Figure C60. After the activation period, the selectivity was much higher compared to before activation. However, a slight increase in selectivity is still visible, implicating that the activation was not yet complete after 20 hours. In Figure 49, it is shown that the selectivity decreased as the temperature increased, while the conversion increased up to a maximum conversion of 10% (at which point no free oxygen to react with was present anymore).

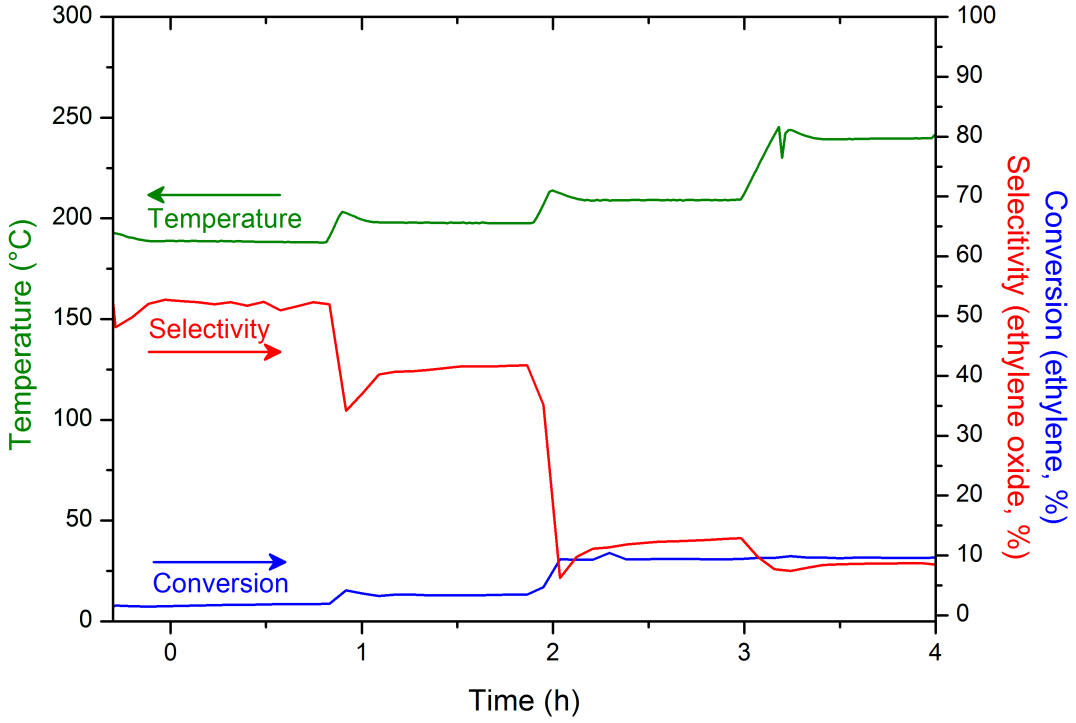

Figure 49: Conversion of ethylene (blue), selectivity towards ethylene oxide (red) and reaction temperature (green) of the epoxidation reaction of ethylene after an activation period of 20 hours (activation period is removed from the graph). As a result of the rising temperature, the conversion increases. The selectivity depends on the conversion, and decreases as the conversion increases.

The correlation between the increase in conversion of ethylene and the decrease in selectivity towards ethylene oxide is linear, and is visualized in Figure 50 (black line). In addition, the correlation between the selectivity and conversion using catalysts

prepared with commercial support materials with less surface area (purple and green line) are shown[1]. Again, in all cases, increasing the reaction temperature causes an increase in conversion and a decrease in selectivity. Furthermore, when a high surface area support material is used, the selectivity decreases compared to when a lower surface area support material is used. This is explained by the amount of hydroxyl groups present, which facilitate a complete combustion reaction (see Section 2.3). As a consequence of the rapid decrease of selectivity towards ethylene oxide at increasing conversion of ethylene, in industry the conversion of the catalytic reaction is generally held up to 3% [42, 43].

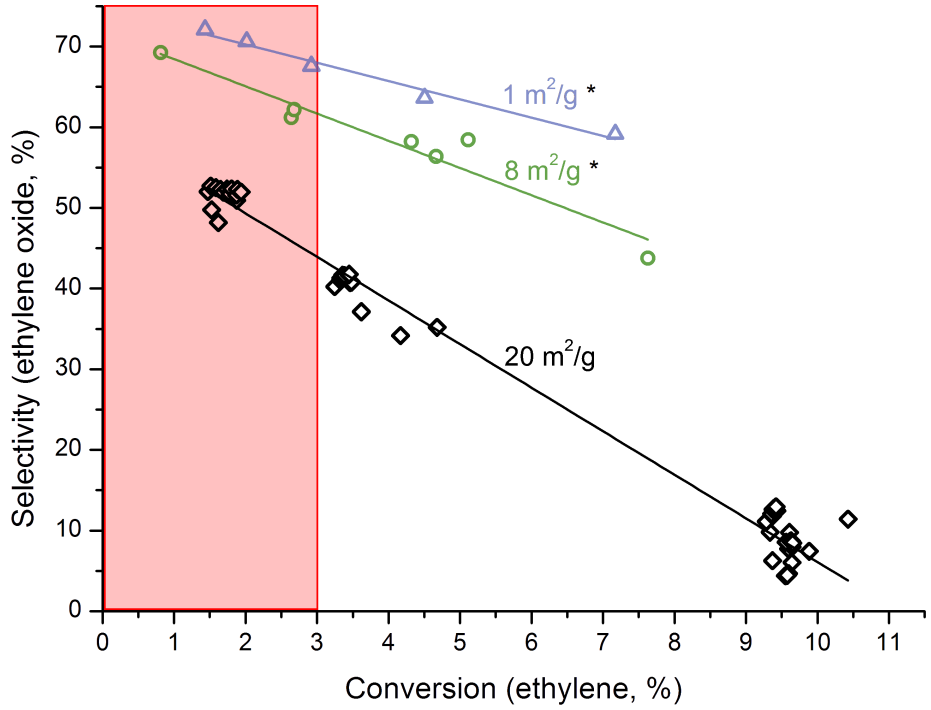

Figure 50: Conversion of ethylene versus selectivity towards ethylene oxide of the epoxidation reaction of ethylene using three different support materials (surface area: 1 m^2/g, 8 m^2/g and 20 m^2/g). At increasing reaction temperature, the conversion increases and the selectivity decreases. Furthermore, a clear trend between the surface area of the support material and the selectivity towards ethylene oxide is observed, since the selectivity decreased at increased support surface area. The catalysts assigned with $\star$ were prepared by Jeroen van den Reijen.

The stability of the catalyst composed of ordered macroporous α-alumina is expected to be higher compared to catalysts composed of low surface area α-alumina materials. However, this was not researched (beyond these 24 hours) using the ethylene epoxidation setup, since not enough measurement time on this setup was available.

[1]These catalysts were prepared by Jeroen van den Reijen.

8 Conclusions

In this research, ordered macroporous α-alumina was synthesized, the pore structure of the material was optimized and the materials were characterized. Colloidal crystals of PMMA spheres were used as template material. The obtained ordered macroporous α-alumina was used as support material in the epoxidation of ethylene, after silver particles were attached to the alumina.

The PMMA colloidal crystals were prepared by surfactant-free emulsion polymerization, oil-in-water solvent evaporation and water-in-oil solvent evaporation. By using oil-in-water and water-in-oil solvent evaporation methods, only small amounts of PMMA was synthesized. Surfactant-free emulsion polymerization was the preferred method, since a large amount (approximately 70 g) of monodisperse PMMA spheres was synthesized. The size of the PMMA spheres is around 410 nm (SEM and UV-VIS spectroscopy). The molar mass of the PMMA chains is approximately $6.8 \cdot 10^5$ g/mol (GPC). The melting point of the PMMA was around 130 °C (DSC) and the decomposition of PMMA started around 250 °C (TGA).

The spheres were assembled into a colloidal crystal by solvent evaporation and by centrifugation. The crystals obtained by both methods were highly ordered. Since the formation of colloidal crystals by solvent evaporation took several days to weeks and large amounts of crystals were obtained in relatively short time by using centrifugation, centrifugation was the preferred method.

The colloidal crystals consisting of PMMA spheres were used as sacrificial template in the synthesis of macroporous α-alumina. The PMMA colloidal crystals were impregnated with both an aluminum hydroxide solution and a mixture of ammonia and methanol, which resulted in the formation of aluminum hydroxide inside the voids of the PMMA colloidal crystals. Ordered macroporous α-alumina was obtained by calcining impregnated PMMA colloidal crystals under air flow at 1150 °C, but the cage structure of the macroporous alumina was only preserved in parts of the material. The PMMA colloidal crystals were decomposed completely at 800 °C, at which temperature γ-alumina was formed. Therefore, the PMMA template could not offer support during this and later phase transitions, which caused partially loss of cage structure.

By calcining the impregnated crystals under nitrogen flow at 1150 °C for 6 hours, carbon covered γ-alumina was formed. This carbon template was formed as a result of the pyrolysis of the PMMA spheres and formed a thin layer on top of the alumina. This layer of carbon stabilized the cage structure during the transformation of amorphous alumina into γ-alumina. A single test was performed to determine the decomposition temperature of this carbon template, which was 900 °C. After the carbon template was burned off, macroporous γ-alumina is obtained.

During a second calcination under air flow at 1150 °C for 6 hours, besides burning away the carbon template, the γ-alumina was transferred into α-alumina. By using 1.5 g of PMMA, 46 mg of α-alumina was obtained. This material only contained macropores and no meso- or micropores. The macroporous structure was present both on the outside and on the inside of the particles. By using SEM, the measured pore size was 219 ± 16 nm and by using UV-VIS, the measured pore size was 220 nm. The size of the windows was 104 ± 12 nm and the walls were 36 ± 6 nm thick (measured

using SEM). This window size corresponds to the window size of 110 nm measured using mercury intrusion. By using N_2-physisorption, the measured surface area of the material was 20 ± 5 m^2/g.

The cage structure of macroporous α-alumina obtained by calcining impregnated PMMA colloidal crystals under nitrogen flow prior to the calcination under air flow was better preserved compared to macroporous α-alumina obtained by calcination under air flow only. This was concluded both from SEM and UV-VIS measurements and is caused by the stabilization of the carbon template present during the conversion of amorphous alumina into γ-alumina.

Three impregnation steps of both the precursor and the ammonia/methanol mixture were used both to increase the amount of alumina synthesized and to improve the pore structure. Using more PMMA as start material did not seem to affect the pore structure. When PMMA colloidal crystals were dried at 60 °C before impregnation, more alumina was synthesized. The drying effect did not seem to have a significant influence on the pore structure. By drying PMMA colloidal crystals at 120 °C, the voids of the alumina decreased in size. Less alumina material was obtained by using these crystals and the obtained alumina consisted mostly of strings and sheets. No significant differences in the quality of the cage structure were observed when alumina obtained by calcination in a combustion boat was compared to alumina obtained by calcination in a plug flow reactor.

Macroporous α-alumina was used as support material for silver particles. Silver particles of about 20 - 80 nm were deposited onto the alumina by incipient wetness impregnation. The distribution of silver particles over the support was not researched. The average crystallite size of the silver particles was 32 nm. The catalyst was tested in the epoxidation reaction of ethylene, in which the conversion and selectivity were measured on various temperatures. The correlation between the conversion and selectivity in the temperature range between 190 and 230 °C was compared to catalysts composed of silver on low surface α-alumina materials (1 and 8 m^2/g). The selectivity towards ethylene oxide is lower for catalysts composed of high surface area alumina compared to catalysts composed of low surface alumina materials. By comparing these catalysts, a clear trend between the selectivity towards ethylene oxide and the amount of in hydroxyl groups present on the support material was obtained. Although no stability tests were performed, the stability of this catalyst is expected to be higher compared to catalysts composed of lower surface area alumina materials.

9 Outlook

Although most of the research questions drafted at the beginning of the project were answered, quite some more questions were raised during this project. In this chapter, an overview of interesting topics correlated to the research described in this thesis is given. These ideas are divided in the subjects related to the template material, the support material and the catalyst.

9.1 Template material

9.1.1 Use of larger PMMA spheres

As discussed in the introduction and in Section 6.3.5, the quality of the cage structure is correlated to the size of the pores [17]. In this research, macroporous material with a pore size of 220 nm was synthesized, but it might be interesting to synthesize α-alumina containing larger pores, using the optimized synthesis method. By both using the optimized synthesis method and by increasing the pore size, ordered macroporous α-alumina with an even better preserved pore structure may be obtained.

9.1.2 Preparation of PMMA colloidal crystals

Further optimization is possible on the assembly of the PMMA spheres into a colloidal crystal. In this research, the PMMA dispersion obtained by surfactant free emulsion polymerization were assembled directly into a colloidal crystal. Only one centrifugation cycle was applied. Therefore, besides MMA and water, traces of KPS (the used initiator) may still be present in the crystals, although no traces were detected using XRD. These traces might influence the catalytic reaction. Additionally, the PMMA spheres in the obtained crystals were ordered for quite large areas, but did include quite some defects. By optimizing the centrifugation step and by applying washing steps, PMMA colloidal crystals of a higher quality may be obtained.

9.2 Support material

9.2.1 Alkoxides precursors or melt impregnation

The amount of obtained macroporous α-alumina is, even after applying several impregnation steps, quite low. The reason for this is the maximum solubility of aluminum nitrate in the methanol/water mixture, which is used as precursor solution.

By using other precursors, such as alkoxides, the yield of the synthesis may be increased, since solutions of these precursors contain higher concentrations of aluminum. The downsides of using an alkoxide as precursor is the limited stability of the smaller molecules and the difficulty of penetrating the voids of the PMMA colloidal crystals when more bulky molecules are used.

Another method to increase the yield of the alumina, is by applying melt impregna-

tion. The difficulty of this method is the low melting point of the PMMA colloidal crystals (130 °C). Some tests were performed using aluminum nitrate nonahydrate, since literature provides a melting point of 73.5 °C for this precursor [44]. However, no melting of the aluminum nitrate nonahydrate was observed when the material was heated up to 160 °C in an oil bath. DSC measurements of this material are shown in Figure B59 (Appendix B), whereby the material was heated twice to 95 °C and to 150 °C. In both measurements, no melting or solidification peaks of the aluminum nitrate nonahydrate were observed around 73.5 °C. However, a large negative peak is observed in curves 1 at 84 - 86 °C, which is most likely a result of the formation of anhydrous aluminum nitrate. Moreover, peaks in XRD diffractograms of material heated to 85 °C, 100 °C and 160 °C could not be identified and showed no overlap with each other. This indicates that decomposition of the aluminum nitrate was already taking place. Other aluminum precursors with a low melting point may give better results.

9.2.2 Bulk characterization by using UV-VIS spectroscopy

UV-VIS spectroscopy showed to be an useful method in addition to SEM to research the quality of the pore structure and to see the influence of the extra calcination step applied during the synthesis of ordered macroporous α-alumina (Section 6.3.5). Therefore, in addition, this characterization technique can be used to investigate the influence of other alternations on the synthesis method simultaneously. In particular, it would be interesting to confirm the influence of multiple impregnation steps on the quality of the pore structure of the obtained alumina material.

Likewise, UV-VIS spectroscopy can be used to compare material calcined in a reactor to material calcined in a combustion boat. As mentioned in Section 6.3.7, the first calcination under inert atmosphere is expected to play the largest role. However, since the color of this material is black, and is therefore difficult to measure with UV-VIS spectroscopy, it might be wise to calcine the material again under air flow above 900 °C, to remove all residual carbon.

Furthermore, the comparison of UV-VIS spectra of macroporous γ-alumina after burning away the carbon and of macroporous α-alumina might be interesting. By using SEM, the quality of the cage structure of the γ-alumina seems higher compared to the quality of α-alumina, but no bulk characterization was performed on the ordered macroporous γ-alumina.

9.2.3 Calcination parameters

By adjusting calcination parameters, various alumina materials were obtained. The addition of the calcination step under inert atmosphere certainly had a positive influence on the quality of the pore structure of the obtained alumina materials. It would be very interesting to obtain macroporous α-alumina by increasing the temperature of the calcination under inert atmosphere, since the carbon template would still be present in this case to stabilize the pore structure. However, to obtain α-alumina under these conditions, the calcination temperature needs to be increased above 1150 °C. At the research group Condensed Matter and Interfaces (Utrecht University), an oven is available where this calcination could be performed. To start with, I would suggest

an temperature of 1300 °C. This temperature is significantly higher compared to 1150 °C, so this could be high enough to convert the γ-alumina into α-alumina, but might still be low enough to prevent extreme sintering of the alumina.

Another study could be performed about the calcination ramp, since by lowering the ramp, the structure transformations might occur more gradually, which might improve the quality of the pore structure. On the other hand, a lower ramp leads to a longer calcination time, which could lead to increased sintering and deformation of the cage walls.

9.2.4 γ-alumina

Although for the epoxidation reaction of ethylene α-alumina was preferred as support material, for multiple other catalytic processes γ-alumina is used. One example of these reactions is the hydrodemetallization catalyst, which is used in the oil refinery. By using macroporous γ-alumina as a model support material, information about the deactivation mechanism of several other types of catalysts may be researched. New insights in deactivation mechanisms were already gained by using other ordered mesoporous support materials [11–13].

9.3 Catalyst

9.3.1 Impregnation

In this research, incipient wetness impregnation was applied to attach silver particles to the support material. More research can be performed on the impregnation on macroporous materials, for instance on the particle size and distribution.

9.3.2 Characterization

Minimal characterization was performed on the obtained catalyst. The size and distribution of the silver particles was not researched and therefore, qualitative conclusions cannot be drawn. By microtoming the catalytic particles, the particle distribution may be visualized. Furthermore, the size of the silver particles inside the pores of the support material can be measured this way. The particle size may also be measured by using UV-VIS spectroscopy, as a result of surface plasmon resonance of the silver particles, and by H_2-O_2 chemisorption titration measurements. Finally, by using a small sieve fraction (< 38 μm) or by crushing or dissolving the alumina material, silver particles on the inside of the pores will be visible in pictures obtained using TEM or SEM.

9.3.3 Stability tests

Finally, stability tests should be performed on catalysts containing ordered macroporous α-alumina as support material. The purpose of using this material as sup-

port material, is to research the deactivation mechanism of the catalyst, since ordered macroporous α-alumina can be used as a model system.

Besides stability tests in the epoxidation reaction of ethylene, sintering tests can be performed by heating the catalysts in an oven. Both the increase in surface area as the morphology could play a role during the sintering. To see the influence of only one of these factors, three different sets of catalyst should be prepared, which are listed in Table 7.

Table 7: Catalysts to prepare for stability tests

Catalyst	Surface area alumina (m^2/g)	Size silver (nm)	Loading silver (wt%)
1	20	20	0.1
2	1	20	0.1
3	20	80	0.1
4	1	80	0.1
5	20	20	5
6	1	20	5

Morphology
The influence of the morphology of the alumina (the macroporous structure) can be researched by comparing particle growth of four different catalysts in which the silver loading is kept around 0.1 wt% and the particle size is varied (catalysts 1 - 4).

If a difference is observed in particle growth between both catalysts with large silver particles (catalyst 3 and 4), whereas a significant minor difference is observed in particle growth between both catalyst with small silver particles (catalyst 1 and 2), the morphology of the support influences the stability of the silver. This, because the morphology is expected be of less influence to smaller silver particles.

Surface area
The influence of the increased surface area can be researched by comparing particle growth of four different catalysts in which the silver particle size is 20 nm and the loading is varied (catalysts 3 - 6).

In this case, the increase in surface area is expected to mainly provide extra stability in the case of the high silver loadings, since here the silver particles will be closer together compared to the catalyst with low loading silver. Therefore, an influence of the increased surface area is present if there is a difference observed in particle growth between both catalysts with a high silver loading (catalyst 5 and 6), whereas no or a significant minor difference is observed in particle growth between both catalyst with a low silver loading (catalysts 1 and 2).

In this tests, there are some difficulties. It might not be possible to synthesize a catalyst in which silver particle of 20 nm in size are distributed over an 1 m^2/g α-alumina support with a loading of 5 wt%, since the maximum theoretical loading, whereby no space between the silver particles is present is 6.5 wt%. Another difficulty is measuring the size of the silver particles during or after sintering. An increase in crystallite size

might be detectable by using in situ high temperature XRD measurements, but ex situ XRD measurements on sintered material showed otherwise. The characterization methods mentioned in Section 9.3.2 might be used, but sintering experiments must be performed at various different temperatures to get a complete overview of the sintering process.

10 Acknowledgments

A lot of people helped me to perform the research described in this thesis. First of all, I would like to thank my supervisors. Jeroen, ik ben erg blij dat je mijn begeleider was voor dit project. Ik heb afgelopen jaar erg veel plezier in mijn onderzoek gehad, waarin het krijgen van goede begeleiding een grote rol heeft gespeeld. Vooral de discussies die we hadden over de aanpak van nieuwe ideeën, rare resultaten die we daardoor behaalden en conclusies die we er toch uit konden halen vond ik erg prettig. Ik heb erg veel geleerd van de kritische vragen die je me tijdens het project stelde. Bedankt dat je altijd beschikbaar was voor vragen en je altijd de tijd nam om dingen duidelijk uit te leggen. Petra, bedankt voor de prettige gesprekken die we hebben gehad waarbij tijdens het bespreken van mijn resultaten altijd veel nieuwe goede ideeën ter sprake kwamen. Peter, thank you for taking the time to examine my thesis. Jovana Zečević, although you will not examine my thesis anymore, I would like to thank you for your enthusiasm about my performed work.

Furthermore, many people helped me to characterize my materials. Marjan Versluijs-Helder, bedankt voor het maken van de mooie SEM foto's, de instructie van en hulp met het maken van XRD diffractogrammen en voor het doen van de TGA-MS metingen. Hans Meeldijk en Chris Schneijdenberg, bedankt voor de uitleg van de Phenom SEM en alle hulp die ik nodig had tijdens het klaarmaken of bekijken van mijn materialen. Iván Garcia Torregrosa, thank you for helping me out with the FIB-SEM measurements, which took a bit longer than planned, but resulted in nice pictures. Nazila Masoud and Lisette Pompe, thank you for the preparation of the microtomed samples and for making the valuable TEM pictures. For the N_2-physisorption measurements I would like to thank Nazila Masoud, Pasi Paalanen, Suzanne Verkleij and Peter Bramwell and for the performed mercury intrusion measurements I would like to thank Peter Lipman (TU/e). Susanne Verkleij, Ramon Oord and Gang Wang, thank you for helping me perform UV-VIS measurements and for the productive discussions about the obtained data. Jan Willem de Rijk, bedankt voor het voorbereiden en uitvoeren van de DSC metingen. Kristel Boere, Mies van Steenbergen en Jeffrey Ritsema, bedankt voor alle hulp met de GPC en DLS metingen die ik op jullie groep kon doen en voor de hulp met het maken van PMMA bollen met de "oil-in-water solvent evaportion" methode (Pharmaceutics, UU). For being able to test my catalyst in the epoxidation setup, I would like to thank the people of the laboratory of Chemical Reactor Engineering at the TU/e.

Finally, I would like to thank all members of the group Inorganic Chemistry and Catalysis for providing such a pleasant environment to do research. I absolutely enjoyed being part of this group.

References

[1] T. E. Lefort, "Process for the production of ethylene oxide (US 1998878 A)," 1931. Societe Francaise de Catalyse Generalisee.

[2] S. N. Goncharova, E. A. Paukshtis, and B. S. Bal'zhinimaev, "Size effects in ethylene oxidation on silver catalysts. Influence of support and Cs promoter," *Applied Catalysis A: General*, vol. 126, pp. 67–84, 1995.

[3] P. Christopher and S. Linic, "Shape- and Size-Specific Chemistry of Ag Nanostructures in Catalytic Ethylene Epoxidation," *ChemCatChem*, vol. 2, no. 1, pp. 78–83, 2010.

[4] M. Mitsuhata, F. Watanab, and T. Kumazawa, "Silver catalyst for production of ehtylene oxide (US 4368144 A)," 1983. Nippon Shokubai Kagaku Kogyo Co.

[5] M. O. Özbek and R. A. van Santen, "The Mechanism of Ethylene Epoxidation Catalysis," *Catalysis Letters*, vol. 143, no. 2, pp. 131–141, 2013.

[6] R. A. van Santen, P. van Leeuwen, J. A. Moulijn, and B. A. Averill, *Catalysis: An Integrated Apporach*. Amsterdam: Elsevier Science B.V., 2nd ed., 1999. pp. 439–442.

[7] L. López Pérez, *Sudies on porosity control and stabilization of mesoporous silicas and aluminas*. PhD thesis, University of Groningen, 2014. pp. 7.

[8] J. Rouquerol, D. Avnir, C. W. Fairbridge, D. H. Everett, J. H. Haynes, N. Pernicone, J. D. F. Ramsay, K. S. W. Sing, and K. K. Unger, "Recommendations for the characterization of porous solids," *IUPAC*, vol. 66, no. 8, pp. 1739–1758, 1994.

[9] M. Ermakova, D. Ermakov, G. Kuvshinov, V. Fenelov, and A. Salanov, "Synthesis of High Surface Area Silica Gels Using Porous Carbon Matrices," *Journal of Porous Materials*, vol. 7, no. 4, pp. 435–441, 2000.

[10] R. J. Konwar and M. De, "Synthesis of high surface area silica gel templated carbon for hydrogen storage application," *Journal of Analytical and Applied Pyrolysis*, vol. 107, pp. 224–232, 2014.

[11] G. Prieto, J. Zečević, H. Friedrich, K. P. de Jong, and P. E. de Jongh, "Towards stable catalysts by controlling collective properties of supported metal nanoparticles.," *Nature materials*, vol. 12, no. 1, pp. 34–39, 2013.

[12] G. Prieto, M. Shakeri, K. P. de Jong, and P. E. de Jongh, "Quantitative Relationship between Support Porosity and the Stability of Pore-Confined Metal Nanoparticles on CuZnO/SiO2 Methanol Synthesis Catalysts," *ACS Nano*, vol. 8, no. 3, pp. 2522–2531, 2014.

[13] P. Munnik, M. E. Z. Velthoen, P. E. de Jongh, K. P. de Jong, and C. J. Gommes, "Nanoparticle growth in supported nickel catalysts during methanation reaction–larger is better.," *Angewandte Chemie*, vol. 53, no. 36, pp. 9493–9497, 2014.

[14] N. D. Petkovich and A. Stein, "Controlling macro- and mesostructures with hierarchical porosity through combined hard and soft templating.," *Chemical Society reviews*, vol. 42, no. 9, pp. 3721–3739, 2013.

[15] B. T. Holland, C. F. Blanford, T. Do, and A. Stein, "Synthesis of Highly Ordered, Three-Dimensional, Macroporous Structures of Amorphous or Crystalline Inorganic Oxides, Phosphates, and Hybrid Composites," *Chemistry of Materials*, vol. 11, no. 3, pp. 795–805, 1999.

[16] S. Sokolov, D. Bell, and A. Stein, "Preparation and Characterization of Macroporous α-Alumina," *Journal of the American Ceramic Society*, vol. 86, no. 9, pp. 1481–1486, 2003.

[17] S. Sokolov, *Macroporous metal oxides: Synthesis, characterization and application in catalysis and electrochemical power sources.* PhD thesis, University of Minnesota, 2003. pp. 28–31.

[18] P. A. Kilty and W. M. H. Sachtler, "The Mechanism of the Selective Oxidation of Ethylene to Ethylene Oxide," *Catal Rev Sci Eng*, vol. 10, pp. 1–16, 1974.

[19] M. Mavrikakis, D. J. Doren, and M. A. Barteau, "Density Functional Theory Calculations for Simple Oxametallacycles: Trends across the Periodic Table," *J. Phys. Chem. B*, vol. 102, no. 2, pp. 394–399, 1998.

[20] G. Rothenberg, *Catalysis.* Weinheim: Wiley-VCH Verlag GmbH & Co. KGaA, 1st ed., 2008. pp. 10–16.

[21] P. Christopher and S. Linic, "Engineering Selectivity in Heterogeneous Catalysis: Ag Nanowires as Selective Ethylene Epoxidation Catalysts," *J. Phys. Chem. Soc.*, vol. 130, no. 34, pp. 11264–11265, 2008.

[22] V. I. Bukhtiyarov, I. P. Prosvirin, R. I. Kvon, S. N. Goncharova, and B. S. Bal'zhinimaev, "XPS study of the size effect in ethene epoxidation on supported silver catalysts," *J. Chem. Soc., Faraday Trans*, vol. 93, no. 13, pp. 2323–2329, 1997.

[23] J. P. Brunelle, "Preparation of catalysts by metallic complex adsorption on mineral oxides," *Pure and Applied Chemistry*, vol. 50, pp. 1211–1229, 1978.

[24] H. Nishihara and T. Kyotani, "Templated nanocarbons for energy storage.," *Advanced materials*, vol. 24, no. 33, pp. 4473–4498, 2012.

[25] I. Sádaba, L. Granados, and E. Taarning, "Deactivation of solid catalysts in liquid media, the case of leaching of active sites in biomass conversion reactions," *Green Chemistry*, vol. 17, pp. 4133–4145, 2015.

[26] J. A. Moulijn, A. E. V. Diepen, and F. Kapteijn, "Catalyst deactivation: is it predictable? What to do?," *Applied Catalysis A: General*, vol. 212, pp. 3–16, 2001.

[27] C. H. Bartholomew, "Mechanisms of catalyst deactivation," *Applied Catalysis A: General*, vol. 212, pp. 17–60, 2001.

[28] A. Rudin, *The Elements of Polymer Science and Engineering.* Academic Press, 2nd ed., 1999. pp 189–196, 281–299.

[29] D. Zou, S. Ma, M. Park, L. Sun, J. J. Aklonis, and R. Salovey, "Model Filled Polymers . V . Synthesis of Crosslinked Monodisperse Polymethacrylate Beads," *Journal of Polymer Science: Part A Polymer Chemistry*, vol. 30, pp. 137–144, 1992.

[30] R. C. Schroden, M. Al-Daous, C. F. Blanford, and A. Stein, "Optical Properties of Inverse Opal Photonic Crystals," *Chemistry of Materials*, vol. 14, no. 8, pp. 3305–3315, 2002.

[31] R. Schroden, N. Balakrishnan, A. Stein, and M. D. Ward, *Inverse Opal Photonic Crystals - A Laboratory Guide*, 2001.

[32] G. I. N. Waterhouse and M. R. Waterland, "Opal and inverse opal photonic crystals: Fabrication and characterization," *Polyhedron*, vol. 26, no. 2, pp. 356–368, 2007.

[33] T.-P. Chiu and T.-M. Don, "Synthesis and Characterization of Poly(methyl methacrylate) Nanoparticles by Emulsifier-Free Emulsion Polymerization with a Redox-Initiated System," *Journal of Applied Polymer Science*, vol. 109, pp. 3622–3630, 2008.

[34] M. A. Zulfikar, A. W. Mohammad, A. A. Kadhum, and N. Hilal, "Synthesis and characterization of poly(methyl methacrylate)/SiO2 hybrid membrane," *Materials Science and Engineering A*, vol. 452-453, pp. 422–426, 2007.

[35] R. C. Schroden and A. Stein, *3D Ordered Macroporous Materials, in Colloids and Colloid Assemblies: Synthesis, Modification, Organization and Utilization of Colloid Particles.* Weinheim, FRG: Wiley-VCH Verlag GmbH & Co. KGaA, 2003. pp. 465–493.

[36] H. Masuda, M. Ohya, H. Asoh, M. Nakao, M. Nohtomi, and T. Tamamura, "Photonic Crystal Using Anodic Porous Alumina," *Japanese Journal of Applied Physics*, vol. 38, no. 2, No. 12A, pp. L1403–L1405, 1999.

[37] Ö. Z. Cebeci, *Mercury intrusion porosimetry theory and its application to air-entrained cement pastes and mortars.* PhD thesis, Iowa State University, 1977. pp. 18–37.

[38] J. Z. Mbese and P. A. Ajibade, "Preparation and Characterization of ZnS, CdS and HgS/Poly(methyl methacrylate) Nanocomposites," *Polymers*, vol. 6, pp. 2332–2344, 2014.

[39] P. Munnik, N. A. Krans, P. E. De Jongh, and K. P. De Jong, "Effects of Drying Conditions on the Synthesis of Co/SiO2 and Co/Al2O3 Fischer Tropsch Catalysts," *ACS Catalysis*, vol. 4, pp. 3219–3226, 2014.

[40] K. P. de Jong, *Synthesis of Solid Catalysts.* Weinheim: Wiley-VCH Verlag GmbH & Co. KGaA, 1st ed., 2009. pp. 14–15.

[41] S. M. Pourmortazavi, S. S. Hajimirsadeghi, I. Kohsari, R. Fareghi Alamdari, and M. Rahimi-Nasrabadi, "Determination of the Optimal Conditions for Synthesis of Silver Oxalate Nanorods," *Chemical Engineering & Technology*, vol. 31, no. 10, pp. 1532–1535, 2008.

[42] R. P. Nielsen and J. H. La Rochelle, "Ethylene oxide process (US 4012425 A)," 1975. Shell Oil Company.

[43] A. C. Liu and H. Soo, "Rhenium-promoted epoxidation catalysts and methods of making and using them (US 8546294 B2)," 2010. Dow Technology Investmens, LIc.

[44] D. H. K. Gladstone and A. W. Y. Whippany, "Process for Decomposition of Aluminum Nitrate Nonahydrate (US 3366446)," 1968. Allied Chemical Corparation, pp. 3–6.

[45] H. Yabu, T. Higuchi, and M. Shimomura, "Unique phase-separation structures of block-copolymer nanoparticles," *Advanced Materials*, vol. 17, pp. 2062–2065, 2005.

[46] H. Y. Son, D. J. Lee, J. B. Lee, C. H. Park, M. Seo, J. Jang, S. J. Kim, M. S. Yoon, and Y. S. Nam, "In situ functionalization of highly porous polymer microspheres with silver nanoparticles via bio-inspired chemistry," *RSC Adv.*, vol. 4, pp. 55604–55609, 2014.

Appendix A Template material

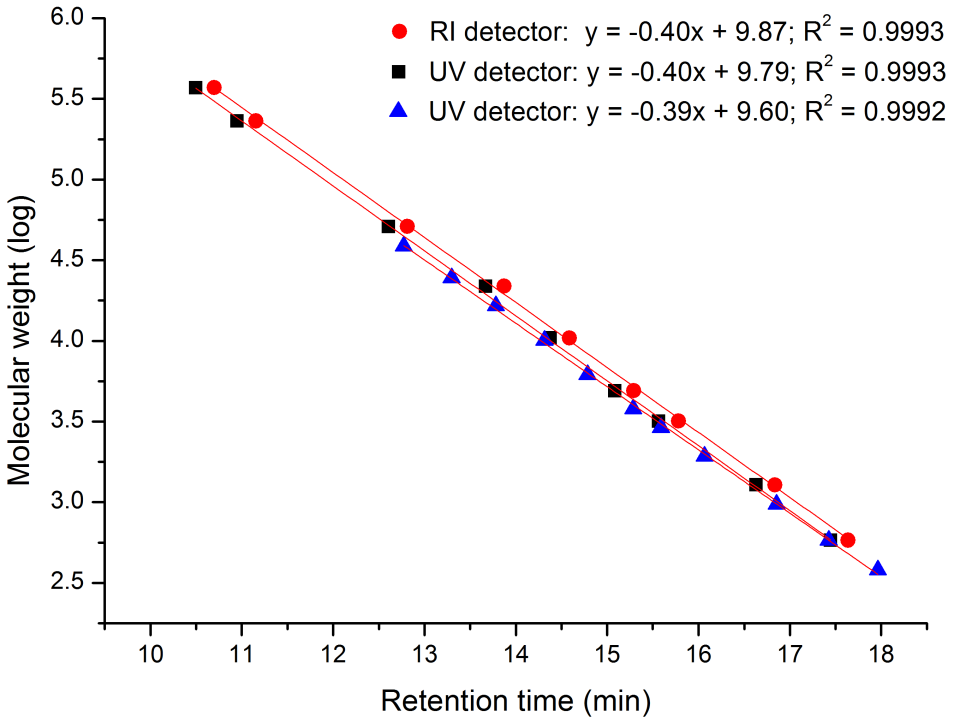

Figure A51: Calibration curves obtained during GPC measurements, using polystyrene as standard and using an UV and a RI detector. The obtained curves were used to determine the molecular weight of the PMMA molecules.

Water-in-Oil and Oil-in-Water solvent evaporation

Methods

Another way to obtain monodisperse PMMA spheres is to dissolve PMMA in a solvent (e.g. THF) and by letting them precipitate in small spheres. The precipitation is caused by the slowly addition of an anti-solvent (e.g. water) in the case of the water-in-oil solvent evaporation method, whereupon the mixture is set aside and the solvent slowly evaporates [45]. In order to only let the solvent evaporate, the chosen solvent should evaporate quicker compared to the chosen anti-solvent. Since the precipitated chains of PMMA are hydrophobic, these cluster together and form small spheres. A schematic representation of this method is shown in Figure A52.

The principle of the oil-in-water solvent evaporation method is the same, apart from the addition of the PMMA solution to the anti-solvent instead of the addition of the anti-solvent to the PMMA solution [46]. Therefore, during the addition stage, already PMMA spheres are formed, which grow during the solvent evaporation step.

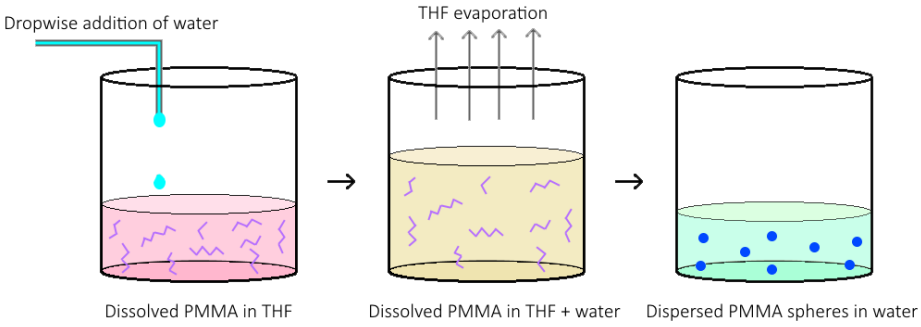

Figure A52: Schematic overview of the water-in-oil solvent evaporation method. PMMA molecules are dissolved as large chains in THF (solvent), even after water (anti-solvent) is added. During the evaporation of THF, PMMA spheres start to precipitate. [45]

Experimental

In Table A8, the used chemicals for the synthesis of PMMA spheres using oil-in-water and water-in-oil solvent evaporation are listed. The chemicals were used as received, no extra purification was applied.

Table A8: Used chemicals, their formula and supplier.

Chemical	Formula	Supplier
Tetrahydrofuran (THF)	C_4H_8O	Biosolve
Poly(vinylpyrrolidinone) (PVP)	$n(C_6H_9NO)$	
Dichloromethane (DCM)	CH_2Cl_2	Sigma-Aldrich

Water-in-oil solvent evaporation
The synthesis of PMMA spheres via water-in-oil solvent evaporation is based on the procedure described by Yabu *et al.* [45]. Using a syringe, 20 mL demiwater was added

drop wise (120 mL/min) to a solution of 10 mg PMMA in 20 mL THF at room temperature. Afterward, the mixture was set aside overnight to let the THF evaporate slowly over time. The next day, a white suspension of PMMA spheres in water was obtained, which was stored in a bottle. The same experiment was repeated, using 50 mg PMMA instead of 10 mg PMMA.

Oil-in-water solvent evaporation
The synthesis of PMMA spheres via oil-in-water solvent evaporation is based on the procedure described by Son *et al.* [46]. 50.6 mg PMMA was dissolved in 2 mL DCM. A 0.5% PVP solution in water was prepared in a beaker. The PMMA solution was added to the PVP solution within 2 minutes under sonication to mix the solutions. After mixing, a dispersion of PMMA spheres was obtained. Afterward, the beaker was stirred with a stirring bean at room temperature overnight, to let the DCM slowly evaporate over time. The next day, the obtained dispersion of PMMA spheres in water was stored in a bottle.

Results and discussion

Water-in-oil solvent evaporation
Using the water-in-oil solvent evaporation method, a low amount (10 mg) monodisperse PMMA spheres were obtained with a size of 650 nm (measured with DLS, DPI: 0.04). Synthesizing PMMA spheres on a large scale with this method is hard. Since the concentration of the start solution of PMMA is around 0.5 g/L, a lot of solvent is needed. When the PMMA concentration was increased 5 times, the particles started to aggregate during the addition of water. Considering the large amount of PMMA spheres needed as template material, this method is not suited for the production of PMMA spheres.

Oil-in-water solvent evaporation
For the oil-in-water solvent evaporation method, 50 mg PMMA was dissolved in 2 mL DCM. Besides the low amount of PMMA spheres obtained using this method compared to SFEP, the obtained spheres were very polydisperse (Figure A53). Therefore, oil-in-water solvent evaporation was not used for the production of PMMA template.

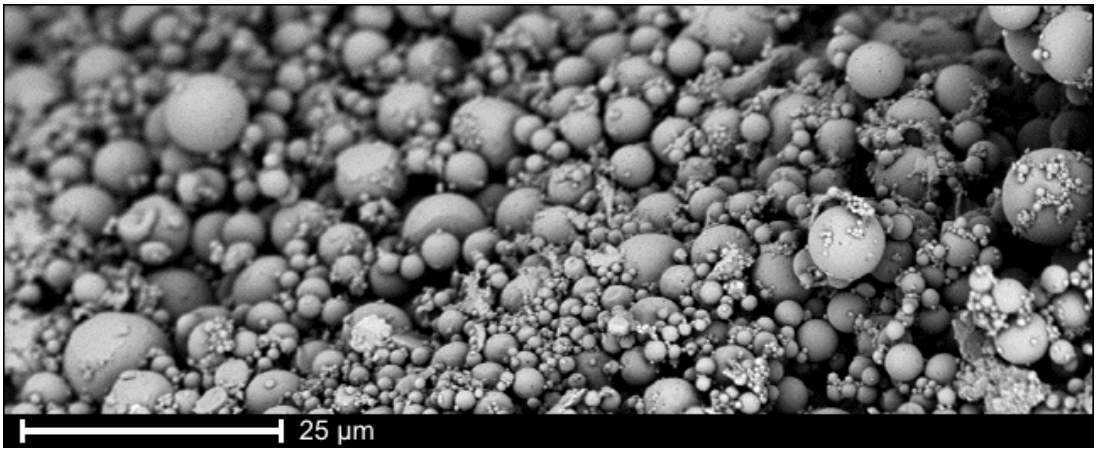

Figure A53: SEM picture of PMMA spheres synthesized using the OIW solvent evaporation method. The synthesized spheres were very polydisperse in size.

Appendix B Support material

Table B9: Performed syntheses ordered macroporous α-alumina (1).

Synthesis in lab journal	Material used	Calcination flow	Calcination temperature (°C)	Calcination time (min)	Used in report
Number of impregnation steps / amount of PMMA used					
Al2O3s22	1.5 g PMMA, three times impregnated	-	-	-	-
Al2O3s22a	Al2O3s22	air	1150	360	-
Al2O3s22b	Al2O3s22a	nitrogen	1150	360	Table 4, 1.5_3_b
Al2O3_s7	1.5 g PMMA, three times impregnated in aluminum nitrate solution	air	1150	360	Table 4, 1.5_3_a
Al2O3_s2	1.5 g PMMA, once impregnated	air	1150	360	Table 4, 1.5_1_a
Al2O3_s8	1.5 g PMMA, twice impregnated	air	1150	360	Table 4, 1.5_2_a
Al2O3_s9	1.5 g PMMA, four times impregnated	air	1150	360	Table 4, 1.5_4_a
Al2O3_s11	6 g PMMA, three times impregnated	air	1150	360	Table 4, 6_3_a
Al2O3_s14	6 g PMMA, three times impregnated	-	-	-	-
Al2O3_s14a	Al2O3_s14	nitrogen	1150	360	-
Al2O3_s14b	Al2O3_s14a	air	1150	360	-
Al2O3_s14c	Al2O3_s14b	air	1150	360	Chapter 7
Al2O3_s18	6 g PMMA, three times impregnated	-	-	-	-
Al2O3_s18a	Al2O3_s18	nitrogen	1150	360	-
Al2O3_s18b	Al2O3_s18a	nitrogen	1150	360	-
Al2O3_s18c	Al2O3_s18b	air	1150	360	Table 4, 6_3_b
Calcination temperature alumina without PMMA					
Al(OH)3_s3_60°C	Aluminium hydroxide*	-	-	-	Figure 28
Al(OH)3_s3_200°C	Al(OH)3_s3_60°C	nitrogen	200	30	Figure 28
Al(OH)3_s3_400°C	Al(OH)3_s3_60°C	nitrogen	400	30	Figure 28
Al(OH)3_s3_600°C	Al(OH)3_s3_60°C	nitrogen	600	30	Figure 28
Al(OH)3_s3_800°C	Al(OH)3_s3_60°C	nitrogen	800	30	Figure 28
Al(OH)3_s3_1000°C	Al(OH)3_s3_400°C	nitrogen	1000	30	Figure 28
Al(OH)3_s3_1150°C	Al(OH)3_s3_600°C	nitrogen	1150	30	Figure 28
Al(OH)3_s3_1150°C_3h	Al(OH)3_s3_1150°C	nitrogen	1150	180	Figure 28
Calcination temperature impregnated PMMA under air flow					
Al2O3_s20	6 g PMMA, once impregnated	-	-	-	Figures 29 - 31
Al2O3_s20_200C	Al2O3_s20	air	200	360	Figures 29 - 31
Al2O3_s20_400C	Al2O3_s20	air	400	360	Figures 29 - 31
Al2O3_s20_600C	Al2O3_s20	air	600	360	Figures 29 - 31
Al2O3_s20_800C	Al2O3_s20	air	800	360	Figures 29, 30
Al2O3_s20_1000C	Al2O3_s20_400C	air	1000	360	Figure 29
Al2O3_s20_1150C	Al2O3_s20_200C	air	1150	360	Figure 29
Calcination temperature impregnated PMMA under nitrogen flow					
Al2O3_s23	3 g PMMA, once impregnated	-	-	-	-
Al2O3_s23_200C	Al2O3_s23	nitrogen	200	360	Figure 32
Al2O3_s23_400C	Al2O3_s23	nitrogen	400	360	Figure 32
Al2O3_s12	1.5 g PMMA, once impregnated	-	-	-	-
Al2O3_s12a	Al2O3_s12	nitrogen	600	360	Figure 32
Al2O3_s17	1.5 g PMMA, once impregnated	-	-	-	-
Al2O3_s17a	Al2O3_s17	nitrogen	800	360	Figure 32
Al2O3_s16	1.5 g PMMA, once impregnated	-	-	-	-
Al2O3_s16a	Al2O3_s16	nitrogen	1000	360	Figure 32
Al2O3_s15	1.5 g PMMA, once impregnated	-	-	-	-
Al2O3_s15a	Al2O3_s15	nitrogen	1150	360	-
Al2O3_s15b	Al2O3_s15a	air	600	360	Figures 32 - 34
Al2O3_s15c	Al2O3_s15b	air	700	360	-
Al2O3_s15d	Al2O3_s15c	air	800	360	-
Al2O3_s15e	Al2O3_s15d	air	900	360	Figures 34, 35

* Prepared by adding ammonia to Al(NO3)3 in H2O, washed with H2O

Table B10: Performed syntheses ordered macroporous α-alumina (2).

Synthesis in lab journal	Material used	Calcination flow	Calcination temperature (°C)	Other parameters changed	Used in report
Pretreatment PMMA					
Al2O3_s4	1.5 g PMMA, once impregnated	air	1150	PMMA crystals dried at 60°C	Section 6.3.6
Al2O3_s19	1.5 g PMMA, once impregnated	air	1150	PMMA crystals dried at 120°C	Section 6.3.6
Calcination in boat versus reactor					
Al2O3_s24	4.5 g PMMA, once impregnated	-	-	-	-
Al2O3_s24a_boat	Al2O3_s24	nitrogen	1150	-	Section 6.3.7
Al2O3_s24a_reactor	Al2O3_s24	argon	1090	calcined in reactor	Section 6.3.7
Al2O3_s24b_boat	Al2O3_s24a_boat	air	1150	-	Section 6.3.7
Al2O3_s24b_reactor	Al2O3_s24a_reactor	5% O2 in H2	1050	calcined in reactor	Section 6.3.7
Al2O3_s24c_reactor	Al2O3_s24b_reactor	static air	1150	muffle oven used	Section 6.3.7
Strength of the pores					
Al2O3_s8_1.5ton	Al2O3_s8	-	-	crushed under 1.5 ton	Section 6.3.8
Al2O3_s11 3ton	Al2O3_s11	-	-	crushed under 3 ton	Section 6.3.8
Other samples					
Al2O3_s1	1.5 g PMMA, twice impregnated	air	1150	PMMA crystals 6 used	-
Al2O3_s3	1.5 g PMMA, twice impregnated	air	1150	PMMA soaked long in ammonia solution	-
Al2O3_s5	1.5 g PMMA, twice impregnated	air	1150	-	-
Al2O3_s6	1.5 g PMMA, twice impregnated	-	-	-	-
Al2O3_s6a	Al2O3_s6	static air	1150	no gas flow	-
Al2O3_s6b	Al2O3_s6a	air	1150	-	-
Al2O3_s10	1.5 g PMMA, once impregnated	-	-	-	-
Al2O3_s10a	Al2O3_s10	nitrogen	1150	-	-
Al2O3_s10b	Al2O3_s10a	air	1150	-	-
Al2O3_s12b	Al2O3_s12a	air	1150	-	-
Al2O3_s17b	Al2O3_s17a	air	1150	-	-
Al2O3_s16b	Al2O3_s16a	air		-	-
Al2O3_s21	3 g PMMA, once impregnated	-	-	-	-
Al2O3_s21a	Al2O3_s21	nitrogen	1150	-	-
Al2O3_s21b_1100	Al2O3_s21a	air	1100	-	-
Al2O3_s21b_1°C/min	Al2O3_s21a	air	1150	ramp: 1°C/min	-
Al2O3_s21b	Al2O3_s21a	air	1150	-	-

Theoretical maximum alumina produced

For this calculation, the following assumptions were made: The synthesis method described by *Sokolov et al.* is used (Synthesis 1.5_1_a, Table 4, Section 6.2.3) [16]. The pore structure of the PMMA colloidal crystals is FCC, which gives a pore volume of 0.26 %. The density of the PMMA colloidal crystals was determined by measuring a volume of 1.4 mL for 1 g of PMMA, using a syringe. All voids of the PMMA colloidal crystals were filled with 1 M aluminum hydroxide and all aluminum hydroxide was converted in alumina.

m_{PMMA}: 1 g
V_{PMMA}: 1.4 mL
$V_{PMMA,unoccupied}$: 0.26 %
$V_{PMMA,unoccupied}$: 0.363 mL
$m_{Al(OH)_3\ in\ voids}$: 0.363 mmol (1 mol/L)
$m_{Al_2O_3\ in\ voids}$: 0.182 mmol (2 $Al(OH)_3$ molecules needed for 1 Al_2O_3)
mAl_2O_{3max}: 0.019 g

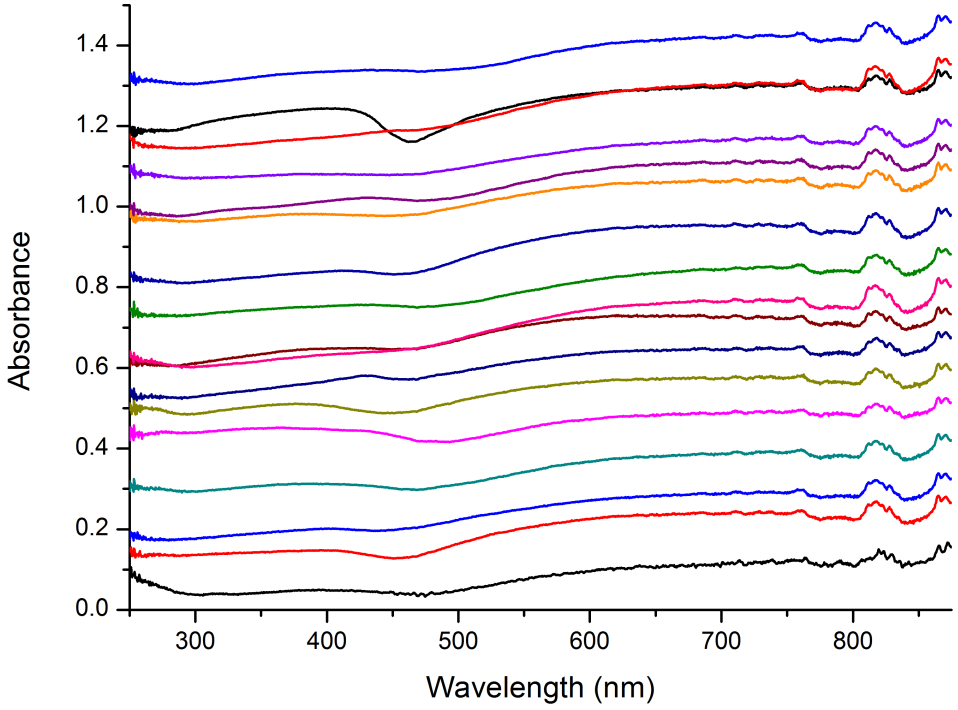

Figure B54: UV-VIS spectra measured on 50 x 50 µm of macroporous alumina material. The light around 465 nm is reflected by the ordered macroporous material. By using the UV-VIS microscope, only direct reflection was measured, resulting in unequal reflection the spectra.

Theoretical surface area ordered macroporous α-alumina

For this calculation, the following assumptions were made: The pore structure is FCC, which means that there are 5 pores per unit cell. The density of the macroporous material is 0.26 times the density of alumina plus 0.74 times the density of air. The diameter of the pores is 220 nm and the window size is 100 nm. Per sphere, 6 windows are present with a radius of 50 nm, which surface area need to be subtracted from the total surfaca area.

$d_{spheres} = 220$ nm

$V_{unit\ cell} = \sqrt{8} * d^3_{spheres} = 30117092\ nm^3 = 3.01*10^{-14}\ cm^3$
$\rho_{support} = 1.04\ g/cm^3$
$\mathbf{m_{unit\ cell} = 3.14*10^{-14}\ g}$

$SA_{1\ pore} = 152053\ nm^2$
$d_{window} = 100$ nm
$SA_{window} = 7854\ nm^2$
$SA_{6\ windows} = 47124\ nm^2$
$SA_{pore\ -\ windows} = 104929\ nm^2$
$\mathbf{SA_{unit\ cell} = 524646\ nm^2 = 5.25*10^{-13}\ m^2}$

$$\textbf{Theoretical surface area} = \frac{\mathbf{SA_{unit\ cell}}}{\mathbf{m_{unit\ cell}}} = \mathbf{16.7\ m^2/g}$$

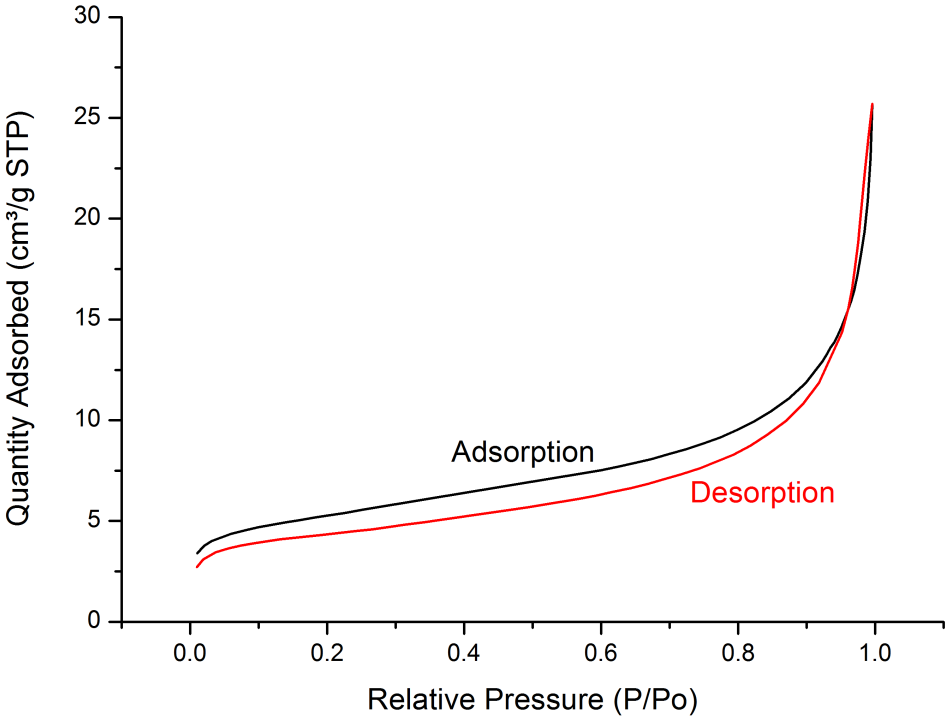

Figure B55: Isotherm obtained during N_2-physisorption measurement. The shape of the curve shows that no micropores or mesopores are present. The BET surface area of this material is approximately 20 m^2/g.

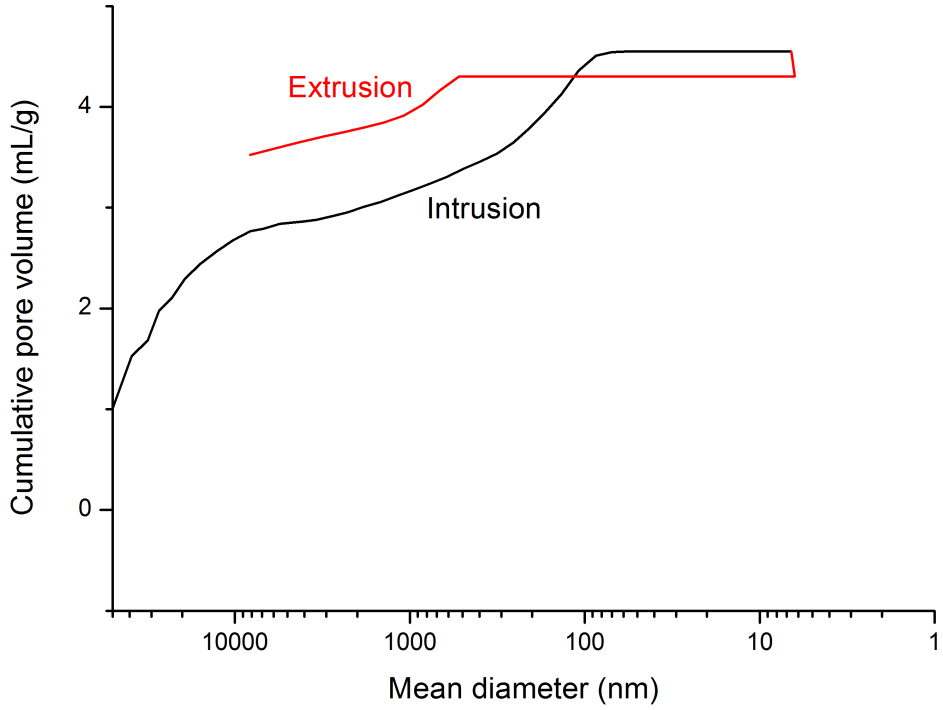

Figure B56: Isotherm obtained during mercury intrusion measurement.

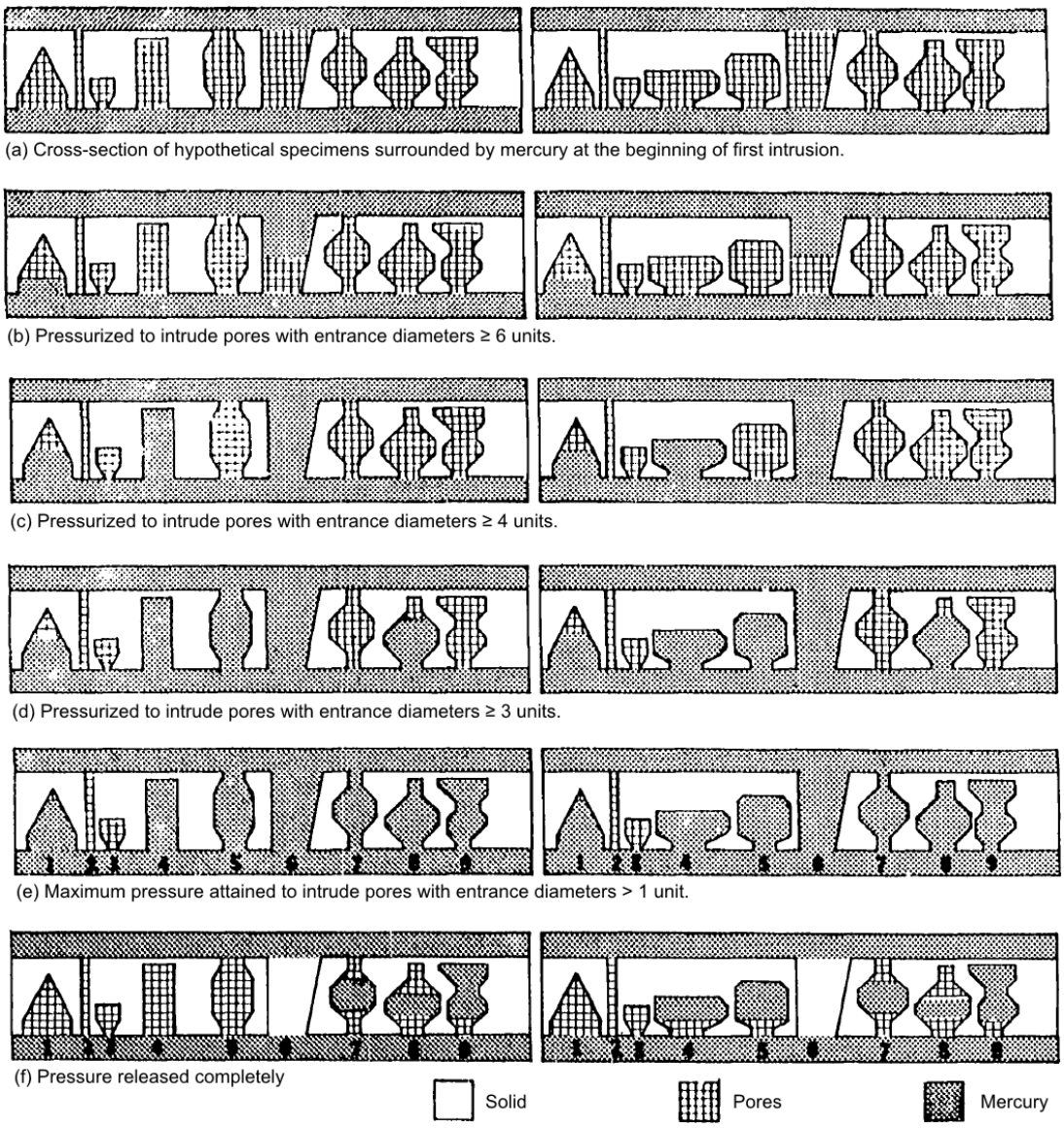

Figure B57: Schematic representation of the pore filling process during a mercury intrusion measurement (a-e). The filling of the pores is analogous to the size of the windows. After the pressure is released, part of the mercury is not removed from the pores (f). [37]

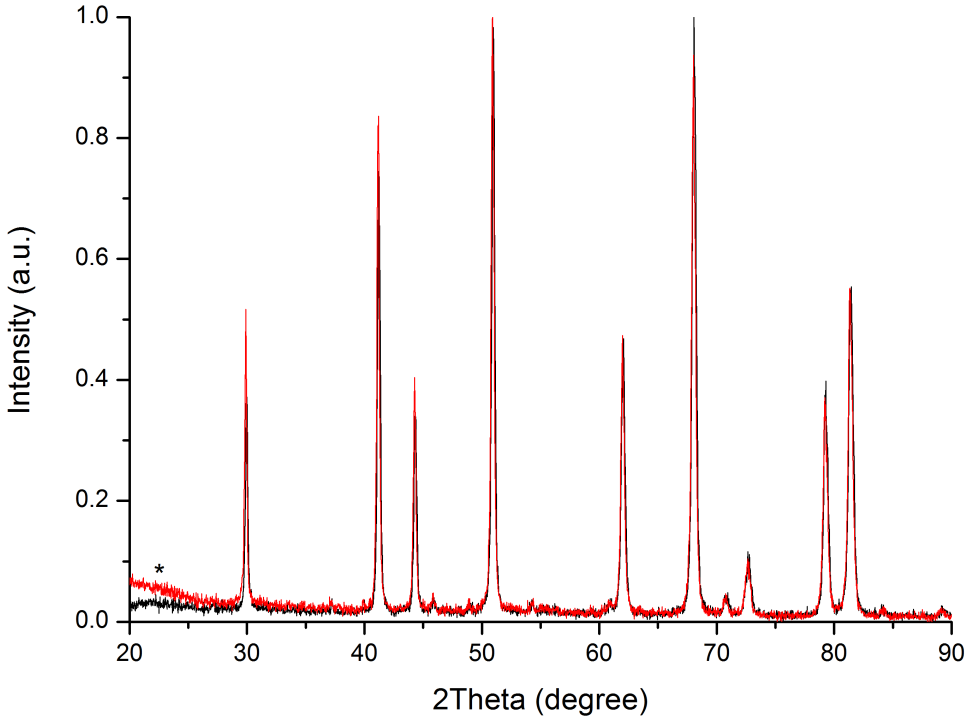

Figure B58: Two XRD measurements performed on the same device, of the same sample. The black line was measured two weeks before the red line. The spectra are the same, except for the peak denoted with $\star$. This peak is observed in other samples as well and is ascribed to an artifact of the measuring device when small amounts of sample were measured.

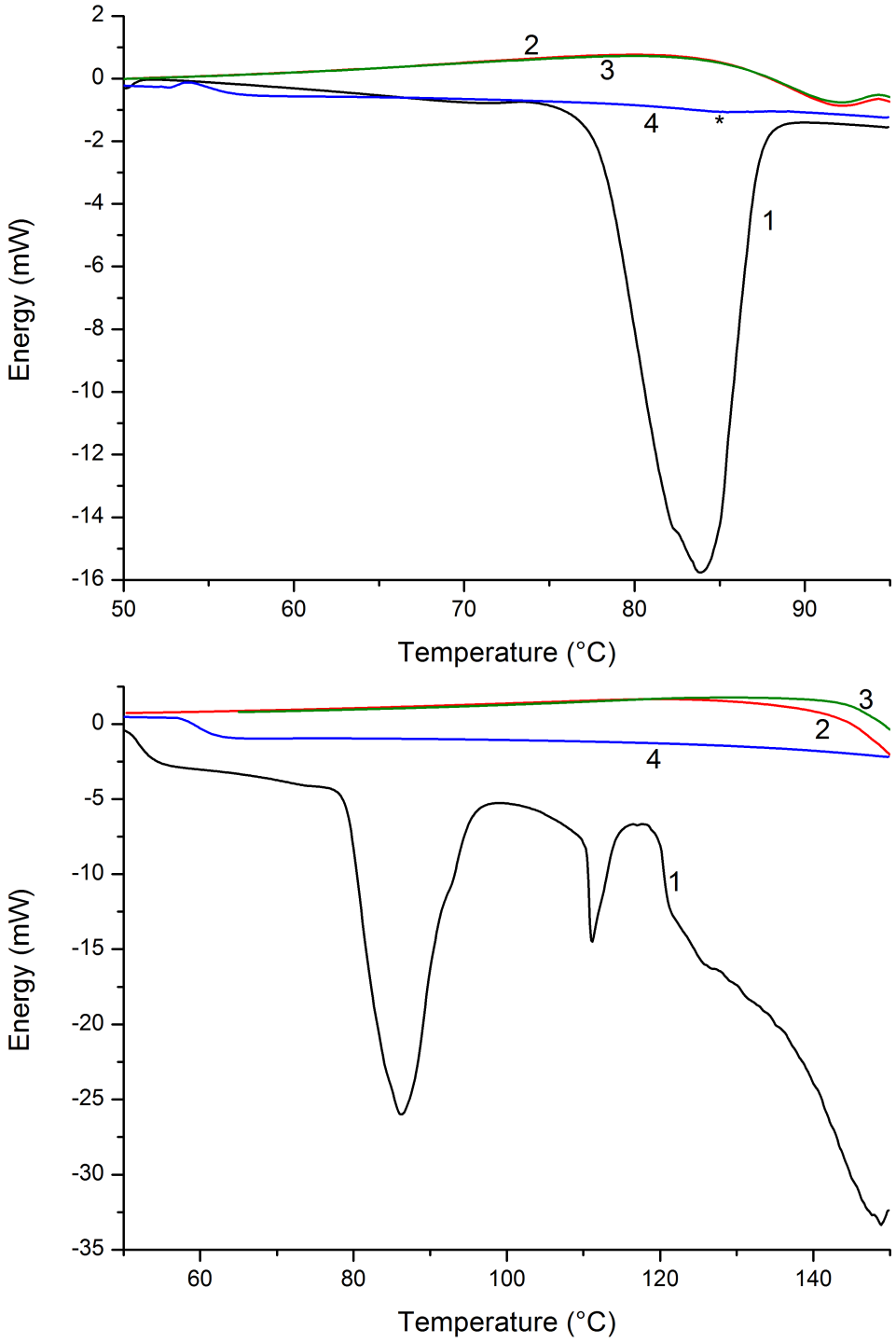

Figure B59: Two DSC measurements performed on aluminum nitrate nonahydrate, once up to 95 °C, 5 °C/min (above) and once up to 150 °C, 10 °C/min (below). The sample is heated in curve 1, cooled down in curve 2, heated up again in curve 3 and cooled down again in curve 4. In the first curve, a large negative peak is present at 84 - 86 °C, which is presumably caused by formation of anhydrous aluminum nitrate, since no solidification peak was observed in curve 2. In the material heated up to 95 °C, a melting peak might be present, assigned with ∗. In the material heated up to 150 °C, two extra negative peaks are present in curve 1, indicating decomposition.

Appendix C Catalyst and catalytic test

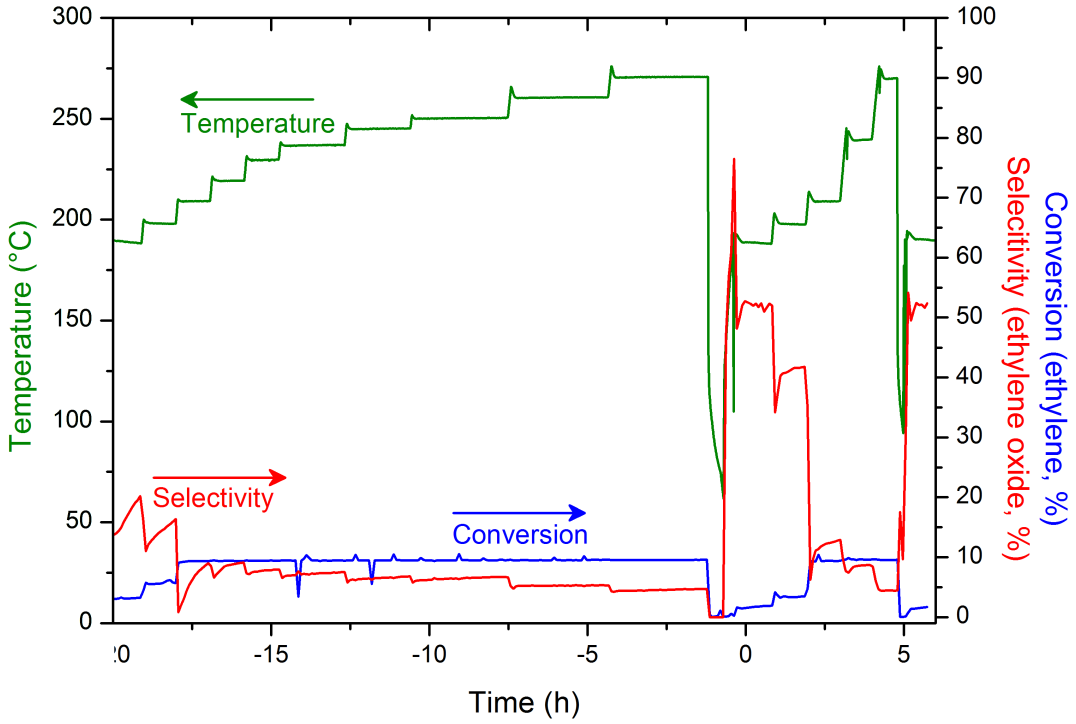

Figure C60: Conversion (blue), selectivity (red) and reaction temperature (green) of the complete epoxidation reaction of ethylene, with an activation period of 20 hours. As a result of the rising temperature, the conversion increases. The selectivity depends among others on the conversion, and decreases as the conversion increases.